RWTH AACHEN UNIVERSITY

Search for electroweak production of supersymmetric particles with photonic final states using the first LHC Run II data recorded with the CMS detector

Masterarbeit in Physik

vorgelegt der
Fakultät für
Mathematik, Informatik und Naturwissenschaften
der RWTH Aachen

von

Johannes Lange

angefertigt am
I. Physikalischen Institut B

Prüfer: Prof. Dr. Lutz Feld
Zweitprüfer: Prof. Dr. Stefan Schael

September 2016

Search for electroweak production of supersymmetric particles with photonic final states using the first LHC Run II data recorded with the CMS detector

Abstract

A search for supersymmetry in final states with photons is presented in this thesis. Data collected in Run II of the Large Hadron Collider at a center-of-mass energy of 13 TeV is used. The proton-proton collision dataset recorded with the CMS experiment in 2015 corresponds to an integrated luminosity of 2.3 fb^{-1}.

The analysis is designed to be sensitive to electroweak production of supersymmetric particles and compressed mass spectra. All considered models are motivated by gauge-mediated supersymmetry breaking. A cut-and-count experiment is performed using three exclusive search bins. No sign for physics beyond the standard model is observed.

Exclusion limits are set for a general gauge mediation scenario and a simplified model assuming electroweak gaugino production. A similar sensitivity is reached as in the search performed at $\sqrt{s} = 8$ TeV.

Additionally, two simplified models of gluino pair production are considered. The currently best limits set by CMS can be improved for these scenarios at large neutralino and chargino masses.

Contents

1 Introduction

Contents

In this thesis a search for supersymmetry using the CMS detector is presented. The results have already been published by the CMS collaboration as a preliminary result in form of a physics analysis summary (PAS) [1]. The collaboration internal documentation of the analysis can be found in the corresponding analysis note (AN) [2]. Both of these documents have mainly been written by the author of this thesis, but they have been reviewed by several other persons on behalf of the CMS collaboration. All figures and tables that have been previously published in the PAS or as additional material contain a corresponding reference in the caption to indicate that the content has been approved by the CMS collaboration. Of those, plots are additionally labeled “CMS preliminary” or “CMS simulation”. Any other plots shown in this document, labeled “CMS private work”, have not been approved by the CMS collaboration.

In the following, a short introduction to the standard model of particle physics is given. Open questions and problems are explained for which supersymmetry might provide answers. The idea of supersymmetry is outlined and the predicted new particle spectrum is explained. The analysis is put into context with related analyses, especially with those previously performed in the same collaboration.

Chapter 2 is dedicated to the Large Hadron Collider (LHC) and the CMS experiment. The event reconstruction and Monte-Carlo simulation are described in Chapter 3. Estimation methods for the expected backgrounds are explained in Chapter 4 and the final results together with statistical interpretations are presented in Chapter 5.

1.1 The standard model of particle physics

The standard model of particle physics (SM) describes the fundamental particles and their interactions using quantum field theory. It has been successful in describing all precision measurements performed to date and the last missing particle, the Higgs boson, has been discovered by the CMS and ATLAS experiments in 2012 [3–6].

In the following, the natural unit system of particle physics is used, i.e. the speed of light and the reduced Planck constant are set to unity ($c = \hbar = 1$). Hence, units are

expressed in powers of the energy unit eV. Especially masses and momenta are mostly given in GeV.

Elementary particles are described as quantum fields and categorized by different properties. Fermions carry half-integer spin (in units of $\hbar$) and integer spin particles are called bosons. Of the fermions, there are six leptons and six quarks which are ordered in three generations. For each fermion there exists a corresponding antiparticle[1] having an opposite electrical charge sign. There are three lepton generations. In each generation there is a charged lepton (electron e, muon μ, and tau τ), each carrying an electrical charge of -1e, and an electrically neutral neutrino ν_ℓ ($\ell = \mathrm{e}, \mu, \tau$). The quarks are also grouped into three generations and categorized as up-type (up u, charm c, top t) with an electrical charge of $+2/3$e and down-type (down d, strange s, bottom b) with $-1/3$e.

All fundamental interactions between particles are mediated by gauge bosons. In the SM these are gluons g, photons γ, and $\mathrm{W}^\pm$ and Z^0 bosons for the strong, electromagnetic, and weak force, respectively, each having a spin of 1. Gravity is the only known force not included in the SM. The spin-2 exchange boson introduced in quantum descriptions of gravity is the graviton G.

The strong force is described by quantum chromodynamics (QCD), which is a non-abelian gauge theory based on the SU(3) symmetry group. Only particles with color charge interact via the strong force. In the SM these are the quarks and the gluons themselves (gluon self-coupling). The eight massless gluons carry color and anticolor. Elementary particles with color charge cannot be observed as free particles, but they always form color-neutral bound states known as hadrons. Quarks and gluons produced in particle collisions will hadronize, meaning that several quark-antiquark pairs are created that form hadrons.

The electromagnetic and weak interactions are described in a unified way, based on the SU(2)×U(1) gauge group. The corresponding gauge eigenstates are the massless W^1, W^2, W^3, and B bosons. The mass eigenstates (γ, $\mathrm{W}^\pm$, Z^0) that can be observed experimentally are obtained by electroweak symmetry breaking,

$$\mathrm{W}^\pm = \frac{1}{\sqrt{2}}\left(\mathrm{W}^1 \mp \mathrm{W}^2\right),$$
$$\begin{bmatrix}\gamma \\ \mathrm{Z}^0\end{bmatrix} = \begin{bmatrix} c_W & s_W \\ -s_W & c_W \end{bmatrix}\begin{bmatrix}\mathrm{B} \\ \mathrm{W}^3\end{bmatrix},$$

with the abbreviations $s_W := \sin\theta_W$ and $c_W := \cos\theta_W$, where θ_W is the weak mixing angle with $s_W^2 \approx 0.23$ [7]. The $\mathrm{W}^\pm$ and Z^0 bosons couple to all quarks and leptons, while the photon only couples to particles carrying electrical charge. A fermion changes its type at an interaction vertex with a $\mathrm{W}^\pm$ boson, i.e. an up-type quark becomes a down-type quark, a charged lepton becomes a neutrino, and vice versa.

The direct inclusion of massive vector bosons breaks the local gauge invariance of the electroweak theory. To be able to introduce the finite masses $m_{\mathrm{W}^\pm} = 80.4\,\mathrm{GeV}$ and

[1] It is yet unclear if this is true for neutrinos. If they are Dirac fermions, like the charged leptons, the neutrino and its antiparticle are distinct particles. In the case of being a Majorana fermion, the neutrino is its own antiparticle.

$m_{Z^0} = 91.2\,\text{GeV}$ [7], the Higgs mechanism is used in the SM. A new complex scalar doublet ϕ is included, called Higgs field. The potential

$$V(\phi) = -\mu^2\phi^\dagger\phi + \lambda(\phi^\dagger\phi)^2 \qquad (\mu^2, \lambda > 0) \tag{1.1}$$

is symmetric in ϕ, but the minimum ϕ_0 is not located at the symmetry point $\phi = 0$. By means of this so-called spontaneous symmetry breaking, the non-zero vacuum expectation value of the Higgs field provides mass terms for the heavy bosons, while maintaining local gauge invariance. In this one-Higgs-doublet form of the Higgs mechanism, four degrees of freedom are introduced (two complex fields). Since the photon does not acquire mass, only three are used for the boson masses and the remaining one manifests in a new observable particle. This spin-0 Higgs boson h^0 is electrically neutral and has a mass of 125.1 GeV [7]. For consistency, the Higgs mechanism in the SM is also used to give masses to the fermions using Yukawa couplings. The search for $h^0 \to b\bar{b}$ and $h^0 \to \tau^+\tau^-$ decays has given first evidence for Higgs-fermion couplings and the analysis of $\sqrt{s} = 13\,\text{TeV}$ LHC data is expected to provide a definite answer [8–10]. Beyond this minimal formalism, extended forms of the Higgs mechanism, such as two-Higgs-doublet models, would be allowed in the SM. Analyses are ongoing to further investigate the properties of the boson found and to search for possible further Higgs bosons [11, 12].

Unsolved questions

The SM has been very successful in describing many experimental results with high precision. Nevertheless it is generally considered obvious that the theory cannot be complete and physics beyond the standard model (BSM) is assumed to exist.

First of all, the SM does not include gravity. The physics of gravitation is described by general relativity, whose predictions have been verified once more with the recent observation of gravitational waves [13, 14]. Gravitational effects are negligible at energy and distance scales that are usually described by quantum theories, such as particle collisions at colliders, but this is no longer true at the Planck scale ($\approx 10^{19}\,\text{GeV}$), where a theory of quantum gravity is needed. Examples of such attempts are string theory and loop quantum gravity, the former also trying to unify gravity and the other fundamental interactions into a "theory of everything" (TOE).

A possible intermediate step towards a TOE would be the unification of the strong and electroweak forces and their description by a single gauge symmetry. For such a grand unified theory (GUT) it is necessary that the running couplings, which depend on the energy scale, unify at some energy Λ_{GUT} called GUT scale. Figure 1.1 illustrates the running of the coupling constants corresponding to the U(1), SU(2), and SU(3) subgroups of the SM. In the SM, no unification of all three couplings is possible, while BSM models such as supersymmetry can achieve this.

The discovery of the Higgs boson with a mass of 125 GeV makes the hierarchy problem a real problem of the SM, which is essentially the huge discrepancy between the electroweak ($\approx 10^2\,\text{GeV}$) and Planck scales ($\approx 10^{19}\,\text{GeV}$) [16]. The ultraviolet cut-off scale Λ_{UV} used to regulate SM loop integrals dictates the maximum energy regime up to which the SM can be valid and in which new physics processes should be present.

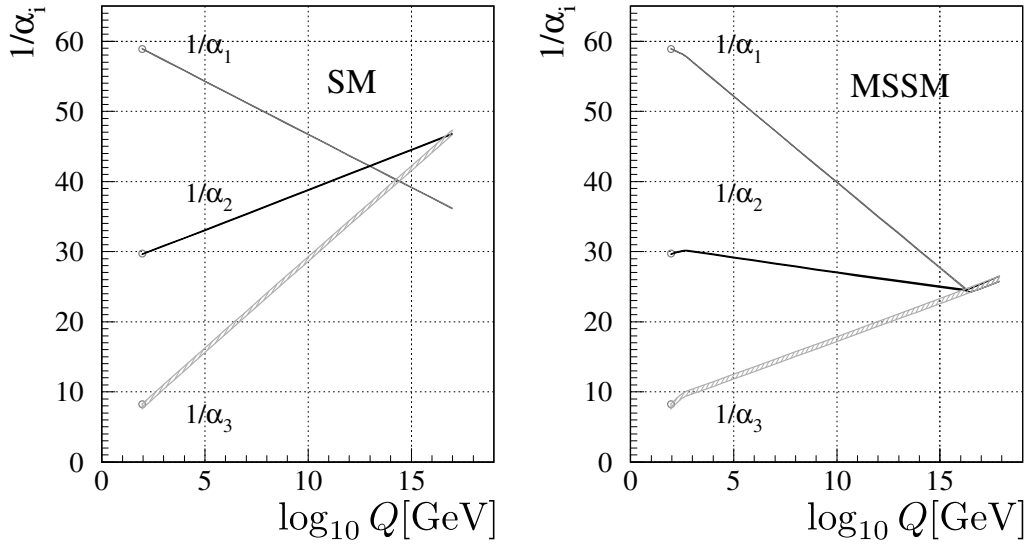

Figure 1.1: Running of the coupling constants as a function of the energy scale Q. The α_i $(i = 1, 2, 3)$ represent the coupling constants corresponding to the U(1), SU(2), and SU(3) subgroups of the SM [15]. Unification of all three couplings is not possible in the SM case (left), while BSM models such as supersymmetry (right) can achieve this. (The figure has been adapted from [15]. Only colors and labels were changed.)

It is generally assumed to be in the order of the Planck scale. All particles coupling to the Higgs boson introduce quantum corrections via virtual loops, leading to quadratic divergences in Λ_{UV} of the mass parameter μ^2 in Eq. (1.1), e.g.

$$\Delta\mu^2 \propto y_f^2 \Lambda_{\text{UV}}^2$$

for a fermion f with the Yukawa coupling parameter y_f. These corrections push the Higgs boson mass towards the Planck scale, which is many orders of magnitude larger than the measured mass. A cancellation of the huge contributions to this precision ("fine tuning") is often considered unnatural. Supersymmetry provides a nice framework in which the corrections automatically cancel. Other attempts to resolve the hierarchy problem are e.g. the introduction of new heavy particles, composite Higgs models [17], or spatial extra dimensions [18].

A further evidence for the SM not being a complete theory is the absence of a candidate for a dark matter particle. Astrophysical observations show that approximately a quarter of the energy density of the universe is composed of dark matter (DM) [7], i.e. mass that is interacting via gravitation, but not electromagnetically. The rotation velocities of galaxies as a function of the radius cannot be explained by the visible mass distribution and suggest the existence of dark matter halos [19]. Also, the gravitational lensing effects observed at galaxy clusters are stronger than anticipated and give strong evidence for the presence of additional non-luminous matter [20]. From the particle physics perspective this implies the existence of weakly interacting massive particles (WIMPs). The SM neutrinos cannot serve as DM particles due to the low masses. While heavy neutral particles can be introduced into the theory ad hoc, many supersymmetric models automatically provide a DM candidate.

1.2 Supersymmetry

Several BSM theories were designed to solve one or several problems present in the SM. Supersymmetry (SUSY) [21–27] is one of the most prominent ones, because it adds a new symmetry that is considered elegant from the theoretical perspective and at the same time it could provide answers to several open questions at once (see Section 1.1).

A new symmetry is introduced that allows for a consistent treatment of fermionic and bosonic fields. The SM symmetry group is extended with fermionic generators Q of SUSY which translate fermion states into boson states and vice versa,

$$Q\,|\text{fermion}\rangle \propto |\text{boson}\rangle\,, \quad Q\,|\text{boson}\rangle \propto |\text{fermion}\rangle\,.$$

The spin of a state is changed by $\pm\frac{1}{2}$, while all other quantum numbers are conserved by the transformation. The simplest form is "$N = 1$ SUSY", meaning that only one pair of Q, $Q^\dagger$ exists [16, 28].

In the minimal supersymmetric extension of the SM (MSSM), exactly one superpartner particle (sparticle) is introduced for each SM particle. Each sparticle has the same quantum numbers as the SM partner, except that the spin is altered by $\frac{1}{2}$. The partners of bosons and fermions are called bosinos and sfermions, respectively. Sparticles are labeled like their SM partners, but with a tilde on top, e.g. selectron $\widetilde{\mathrm{e}}$, up squark $\widetilde{\mathrm{u}}$, and gluino $\widetilde{\mathrm{g}}$. Since the left-handed quarks and leptons are SU(2) doublets and the right-handed ones are singlets, a squark and slepton is introduced for each chirality. Because the sfermions are bosons, the index (L or R) specifies the chirality of the corresponding SM fermion. Since neutrinos are usually treated as massless, the right-handed component is not considered and therefore the chirality index for sneutrinos is suppressed.

While in the SM a single complex Higgs doublet is sufficient, the MSSM requries at least a two-Higgs-doublet model,

$$H_u = \begin{bmatrix} H_u^+ \\ H_u^0 \end{bmatrix}, \quad H_d = \begin{bmatrix} H_d^0 \\ H_d^- \end{bmatrix},$$

to avoid gauge anomalies. Up-type quarks acquire masses from H_u, whereas H_d is responsible for down-type quark and charged lepton masses. With this extended SM Higgs sector, five mass eigenstates h^0, H^0, A^0, $\mathrm{H}^\pm$ exist. The particle found at a mass of 125 GeV is conventionally called h^0, a linear combination of H_u^0 and H_d^0. SUSY partners to the Higgs bosons are called higgsinos.

Like the SM gluons, the gluinos $\widetilde{\mathrm{g}}$ form a QCD color octet and cannot mix with the color-neutral bosinos. The gauge eigenstates of the electroweak gauge bosons are called wino ($\widetilde{\mathrm{W}}^1$, $\widetilde{\mathrm{W}}^2$, $\widetilde{\mathrm{W}}^3$) and bino ($\widetilde{\mathrm{B}}$). Together with the higgsinos they mix to mass eigenstates called neutralinos ($\widetilde{\chi}_1^0$, $\widetilde{\chi}_2^0$, $\widetilde{\chi}_3^0$, $\widetilde{\chi}_4^0$) and charginos ($\widetilde{\chi}_1^\pm$, $\widetilde{\chi}_2^\pm$). The upper index indicates the electrical charge and the lower index numbers the particles increasing with their mass. The non-colored bosinos are also referred to as electroweakinos.

The SUSY part of the MSSM particle spectrum is shown in Table 1.1. In this unbroken form, i.e. if the symmetry is exact, SUSY solves the hierarchy problem exactly. Fermionic and bosonic loops contribute mass corrections with an opposite sign. The

Table 1.1: Sparticle spectrum of the MSSM.

Name	Spin [$\hbar$]	Symbol	
Squarks	0	$\widetilde{u}_L, \widetilde{u}_R, \widetilde{c}_L, \widetilde{c}_R, \widetilde{t}_L, \widetilde{t}_R$ $\widetilde{d}_L, \widetilde{d}_R, \widetilde{s}_L, \widetilde{s}_R, \widetilde{b}_L, \widetilde{b}_R$	
Charged sleptons	0	$\widetilde{e}_L, \widetilde{e}_R, \widetilde{\mu}_L, \widetilde{\mu}_R, \widetilde{\tau}_L, \widetilde{\tau}_R$	
Sneutrinos	0	$\widetilde{\nu}_e, \widetilde{\nu}_\mu, \widetilde{\nu}_\tau$	
Gluinos	$1/2$	$\widetilde{g}$	
			Mass eigenstates
Winos	$1/2$	$\widetilde{W}^1, \widetilde{W}^2, \widetilde{W}^3$	neutralinos
Bino	$1/2$	$\widetilde{B}$	$\widetilde{\chi}_1^0, \widetilde{\chi}_2^0, \widetilde{\chi}_3^0, \widetilde{\chi}_4^0$
Higgsinos	$1/2$	$(\widetilde{H}_u^+, \widetilde{H}_u^0), (\widetilde{H}_d^0, \widetilde{H}_d^-)$	charginos $\widetilde{\chi}_1^\pm, \widetilde{\chi}_2^\pm$

fermion-boson partner structure of SUSY provides exact cancellation of all contributions, due to couplings of the same strength, and thus protects the Higgs boson mass. The R-parity

$$P_R = (-1)^{3(B-L)+2s}$$

is assumed to be conserved in all models considered in this thesis. This combination of baryon number B, lepton number L, and spin s ensures that all SM particles have $P_R = +1$ and all SUSY particles $P_R = -1$. A consequence of R-parity conservation is that only even numbers of sparticles can appear at interaction vertices. For SM particle collisions this implies that SUSY particles are always produced in pairs and that the lightest sparticle (LSP) is stable. A massive LSP without electrical and color charge provides a good DM candidate.

Unfortunately, no experimental evidence for the existence of SUSY particles could be observed to date and therefore the sparticle masses have to be larger than the SM partner masses. If existent, SUSY cannot be an exact symmetry and has to be broken, implying that the hierarchy problem cannot be solved exactly, i.e. the corrections do not cancel precisely. A regulation of the Higgs boson mass is still possible, though, without the need for large fine-tuning, as long as sparticles exist at the TeV scale [29]. This is of special importance for the top squark, since the Yukawa coupling is by far the strongest.

Gauge-mediated SUSY breaking

The possible source of the SUSY breaking is unknown and different mechanisms are proposed theoretically. The main motivation to search for SUSY in final states with photons is gauge-mediated SUSY breaking (GMSB) [30–36].

To achieve symmetry breaking, a new "hidden sector" is introduced. The fields contained in this sector are responsible for the SUSY breaking, while they are almost decoupled from the MSSM particles (the "visible sector"). The only interaction between both sectors is mediated by messenger fields, translating the breaking to the MSSM. In

the case of GMSB, the mediation happens via the gauge interactions. The LSP is a spin-$\frac{3}{2}$ particle, identified with the gravitino $\widetilde{\mathrm{G}}$, the superpartner of the spin-2 graviton G. Because the LSP leaves the detector undetected, causing a momentum imbalance, SUSY signal events are expected to have large missing transverse energy ($E_{\mathrm{T}}^{\mathrm{miss}}$).

1.3 Signal models

All signal models considered in this thesis are motivated by GMSB, i.e. the LSP is always the gravitino. The production of sparticles is categorized into strong and electroweak production. While strong production refers to production of sparticles carrying QCD color charge, electroweak production means direct production of charginos and/or neutralinos. The initially produced sparticles decay, possibly in several subsequent steps, to the next-to-lightest SUSY particle (NLSP), which then decays to the LSP and a SM boson. The branching fractions in the decay cascades depend on different model assumptions like the mixing ratios of the electroweakinos. The LSP is assumed to be massless, leading to prompt decays of the NLSP.

The main model used to guide the analysis is a general gauge mediation (GGM) [37–42] scenario, where the NLSP is the lightest neutralino $\widetilde{\chi}_1^0$. The neutralino decays are determined by the mixing

$$\widetilde{\chi}_i^0 = \sum_{j=1}^{4} N_{ij} \widetilde{\psi}_j^0 ,$$

with $\widetilde{\psi}^0 = (\widetilde{\mathrm{B}}, \widetilde{\mathrm{W}}^3, \widetilde{\mathrm{H}}_d^0, \widetilde{\mathrm{H}}_u^0)^\top$ and a mixing matrix N. In the case of large wino or bino components ("wino-/bino-like") of the NLSP, decays to photons or Z bosons are preferred, while a higgsino-like NLSP can also lead to final states with Higgs bosons. A GGM model of electroweak production is used, which assumes a pure bino $\widetilde{\chi}_1^0$ mixture, while the $\widetilde{\chi}_2^0$ and $\widetilde{\chi}_1^\pm$ are pure wino [43]. Therefore, the neutralino and chargino masses are given by the bino and wino masses, $m_{\widetilde{\chi}_1^0} = m_{\widetilde{\mathrm{B}}}$ and $m_{\widetilde{\chi}_2^0} = m_{\widetilde{\chi}_1^\pm} = m_{\widetilde{\mathrm{W}}}$. Squarks and gluinos are decoupled, i.e. set to very high masses, leading to electroweak production processes. The NLSP decay is determined by its mass $m_{\widetilde{\chi}_1^0}$. The branching ratio of the pure bino $\widetilde{\chi}_1^0$ to photons and Z bosons are

$$\mathrm{BR}(\widetilde{\chi}_1^0 \to \widetilde{\mathrm{G}}\gamma) = \frac{c_W^2}{c_W^2 + s_W^2 \left(1 - \frac{m_{\mathrm{Z}}^2}{m_{\widetilde{\chi}_1^0}^2}\right)^4} \xrightarrow{m_{\widetilde{\chi}_1^0} \gg m_{\mathrm{Z}}} \cos^2\theta_W \text{ , and} \tag{1.2a}$$

$$\mathrm{BR}(\widetilde{\chi}_1^0 \to \widetilde{\mathrm{G}}\mathrm{Z}) = \frac{s_W^2}{c_W^2 \left(1 - \frac{m_{\mathrm{Z}}^2}{m_{\widetilde{\chi}_1^0}^2}\right)^{-4} + s_W^2} \xrightarrow{m_{\widetilde{\chi}_1^0} \gg m_{\mathrm{Z}}} \sin^2\theta_W \text{ ,} \tag{1.2b}$$

i.e. the decay $\widetilde{\chi}_1^0 \to \widetilde{\mathrm{G}}\gamma$ is preferred [44]. Figure 1.2 shows the branching ratios as a function of the NLSP mass. For low NLSP masses, the $\widetilde{\chi}_1^0 \to \widetilde{\mathrm{G}}\mathrm{Z}$ decay is almost completely suppressed.

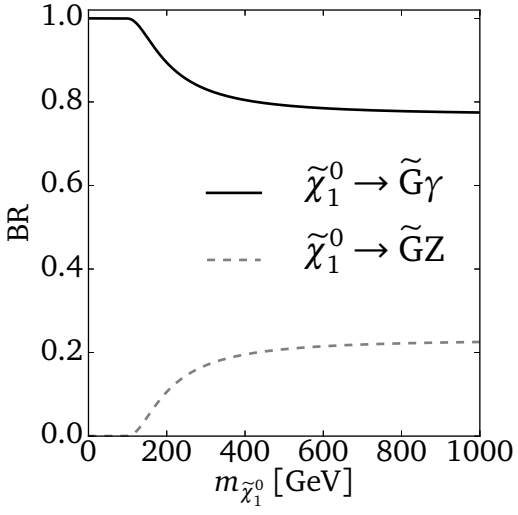

Figure 1.2: Branching ratios for the pure bino NLSP decays to $\widetilde{G}\gamma$ and $\widetilde{G}Z$ as a function of the NLSP mass in the GGM model.

The dominant production mechanism in this GGM scenario is $pp \to \widetilde{\chi}_1^{\pm}\widetilde{\chi}_2^0$, illustrated in the Feynman graph in Fig. 1.3. The $\widetilde{\chi}_1^{\pm}$ and $\widetilde{\chi}_2^0$ decay to the NLSP and a SM electroweak boson. No direct jet production is possible in the sparticle decay chains and jet activity can only be due to initial state radiation or hadronic decays of bosons. The NLSP mass directly influences the transverse momentum of the photons and gravitinos in the final state. Larger masses correspond to larger momenta and missing transverse energy.

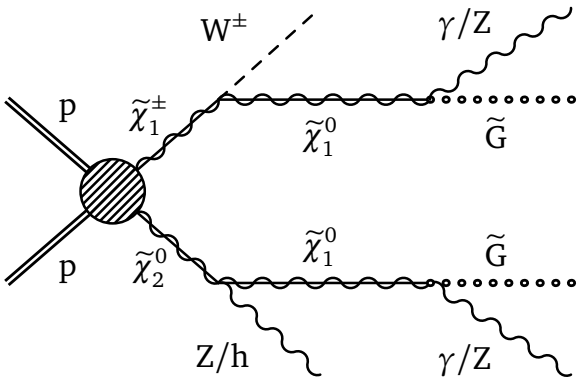

Figure 1.3: Feynman diagram of the dominant $\widetilde{\chi}_1^{\pm}$-$\widetilde{\chi}_2^0$ production mechanism and a typical decay chain in scenarios with a bino-like $\widetilde{\chi}_1^0$ and wino-like $\widetilde{\chi}_2^0$ and $\widetilde{\chi}_1^{\pm}$ [1].

Beyond this full model, simplified models are used for the final interpretation of the search results. For a simplified model, only a small subset of the sparticle spectrum is considered. The production process is fixed and very simple assumptions are made for all branching ratios.

The TChiWg model shown in Fig. 1.4 assumes chargino-neutralino production, both

having the same mass. They directly decay to the LSP and either a W boson or photon with 100% branching ratio, $\widetilde{\chi}_1^{\pm} \to \widetilde{\mathrm{G}}\mathrm{W}^{\pm}$ and $\widetilde{\chi}_1^0 \to \widetilde{\mathrm{G}}\gamma$. Consequently, the final state consists of one photon, missing transverse energy and the decay products of the W boson.

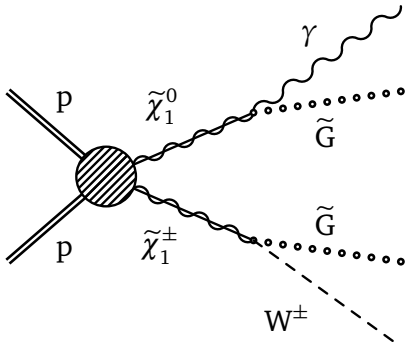

Figure 1.4: Feynman diagram corresponding to the TChiWg simplified model [1].

Two simplified models of gluino pair production are considered additionally. The gluinos $\widetilde{\mathrm{g}}$ decay to $\widetilde{\chi}_1^0$ or $\widetilde{\chi}_1^{\pm}$ and jets with subsequent decays $\widetilde{\chi}_1^0 \to \gamma\widetilde{\mathrm{G}}$ and $\widetilde{\chi}_1^{\pm} \to \mathrm{W}^{\pm}\widetilde{\mathrm{G}}$, where also branching ratios of 100% are assumed. The gluino decay is treated as a three-body decay via a virtual squark. Other analyses specifically targeted at those models typically require jets in addition to photons. In scenarios with compressed mass spectra the jets from the gluino decay are low-energetic and thus not reconstructed, which makes those analyses insensitive. Because no jet requirements are imposed in this analysis, there is no sensitivity loss for small $\Delta m(\widetilde{\mathrm{g}}, \widetilde{\chi}_1^0/\widetilde{\chi}_1^{\pm})$. The models are labeled according to the final state with two photons (T5gg) or a photon and a W boson (T5Wg). Feynman graphs for both models can be found in Fig. 1.5.

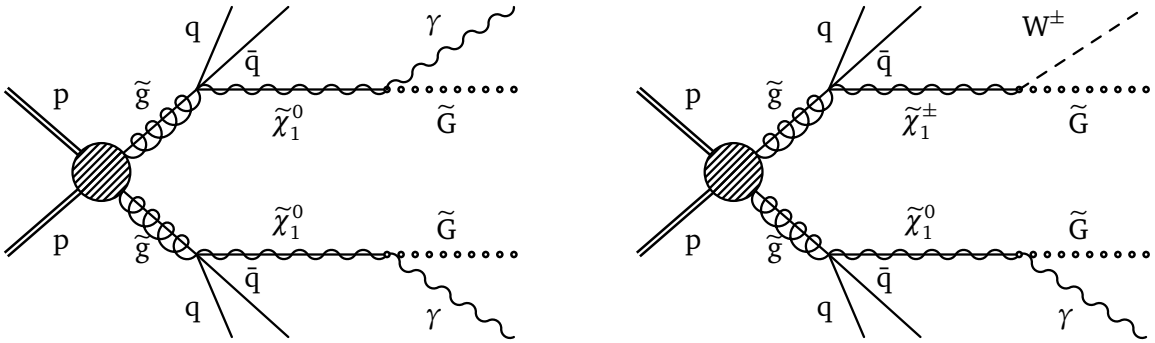

Figure 1.5: Feynman diagrams of the T5gg (left) and T5Wg (right) simplified models [1].

1.4 Previous and related SUSY searches

Searches for supersymmetry have already been performed at lower center-of-mass energies at different experiments, e.g. at the Large Electron-Positron Collider (LEP) [45]

or the Tevatron pp̄-collider [46]. Also, one of the main physics goals of the LHC is the discovery of yet unknown particles and phenomena. During its Run I at center-of-mass energies of 7 TeV and 8 TeV, many searches were performed using different final states, but no significant sign of deviations from the SM was observed. A summary of the results of the 8 TeV CMS SUSY searches published until February 2015 is shown in Fig. 1.6. For each search channel, the pull is calculated, i.e. the difference of the number of observed and expected background events divided by the total uncertainty, not considering possible correlations. Channels with an expectation of less than one event are excluded. The histogram of the pull values shows a gaussian shape with a mean close to zero, as expected for data distributed according to the background-only hypothesis. A possible explanation for the standard deviation being smaller than one is a slight overestimation of the systematic uncertainties in many analyses.

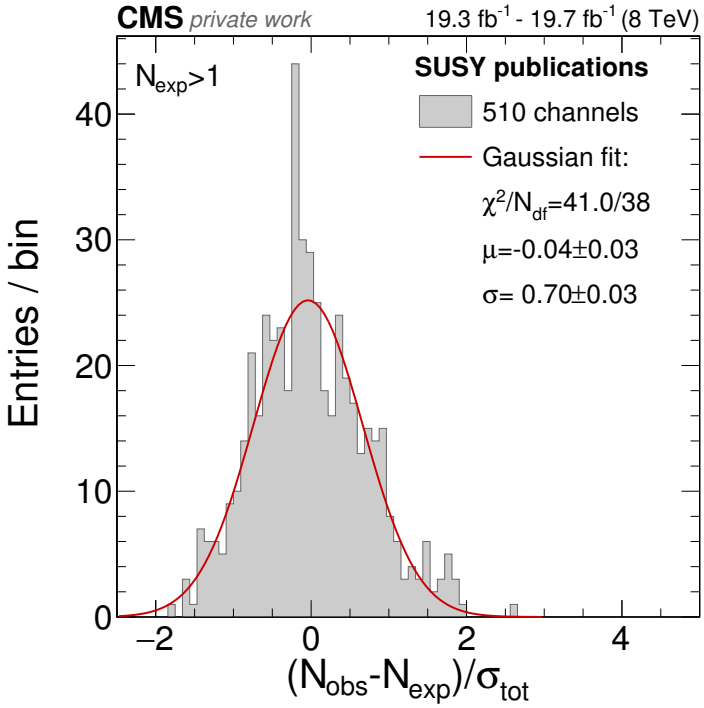

Figure 1.6: Summary of the $\sqrt{s} = 8\,\text{TeV}$ CMS SUSY results published until February 2015. A histogram of the pulls of all search channels is shown together with a gaussian fit. Channels with an expectation of less than one event are excluded. These results have been presented in this or a similar form before [47, 48].

Most of the CMS searches with photon final states in Run I were targeted at strong production, owing to the larger production cross section, and therefore often requiring the presense of jets [49, 50]. Due to the possibility of NLSP decays to W bosons in GMSB, dedicated SUSY searches for events containing a photon and a lepton were performed [51]. Since the Higgs boson can be produced in sparticle decays, the $h^0 \to \gamma\gamma$ channel was used in diphoton searches [52, 53]. Explicit searches for electroweak production, not containing photon final states, have been published for $\sqrt{s} = 8\,\text{TeV}$ [54]. Searches with photonic final states have also been carried out by the ATLAS collabora-

tion [55, 56].

The predecessor of the analysis presented here, searching for electroweak production of gauginos using final states with photons at $\sqrt{s} = 8\,\text{TeV}$, has just been published [57, 58]. The analysis strategy and background prediction methods used here are similar to those used in the $\sqrt{s} = 8\,\text{TeV}$ search. In Run I, a special "parked dataset" [59] corresponding to an integrated luminosity of $7.4\,\text{fb}^{-1}$ recorded with a photon+$E_{\text{T}}^{\text{miss}}$ trigger with low thresholds was used, whereas in this analysis a pure photon trigger is used. This change, apart from the increased center-of-mass energy, is the main change of the analysis with respect to the predecessor. The different selection with a photon-p_{T} threshold increased by more than 100 GeV implies modifications in the definition of several regions used for the background prediction, which has been further optimized in this analysis. With the dataset recorded in 2015 ($2.3\,\text{fb}^{-1}$) at $\sqrt{s} = 13\,\text{TeV}$, a sensitivity similar to the 8 TeV search is expected for electroweak production scenarios. The strong production cross section increase with the higher center-of-mass energy is large enough to have a higher sensitivity, though no strong production interpretation was provided in [57]. The full dataset that will be collected in 2016 (cf. Chapter 2) will greatly increase the discovery potential with respect to the 8 TeV analysis.

Of the ongoing 13 TeV photonic SUSY searches at CMS, the diphoton and Higgs-to-diphoton searches have been published as preliminary results [60, 61], as well as the ATLAS diphoton and photon+jets analyses [62, 63].

2
Experimental setup

Contents

To resolve ever smaller structures of matter and produce yet undiscovered particles, reactions of elementary particles have to be investigated at increasing energies. Previous electron(-positron) colliders have proven to be a precise instrument in particle physics research for the determination of many properties and parameters of the SM and to probe BSM theories. To reach even higher energies and potentially produce heavier particles, hadron colliders are used, the currently most energetic being the Large Hadron Collider.

2.1 The Large Hadron Collider

The Large Hadron Collider (LHC) [64] is located near Geneva in a ring tunnel of 26.7 km circumference 45−170 m underground, crossing the French-Swiss border. The tunnel has been built for the LEP collider, which was closed in 2000, and has been reused for the LHC, which accelerates and collides protons and lead ions. LHC's first physics operation began in 2010. To reach beam energies in the TeV range, an accelerator chain is needed. For the LHC the accelerator complex has been established by using the last main accelerator as a pre-accelerator for the newest collider. Starting from a linear accelerator (Linac2), protons are brought to higher energies in several steps in the proton synchrotron booster (PSB), proton synchrotron (PS) and super proton synchrotron (SPS), which finally injects proton bunches with 450 GeV beam energy into the LHC. The LHC is divided into eight sectors as shown in Fig. 2.1 with interaction points (IPs) in four of them, where both beams intersect and can be brought to collision. The superconducting acceleration cavities are located in sector 4 and operate at 400 MHz. Dipole magnets are used to bend the particle trajectories and enable the circular collider layout. Quadrupole magnets are needed for beam focussing and higher-order multipoles, most importantly sextupoles, are used to correct chromaticity, i.e. energy dependent tune shifts, and the influence of non-linear fields introduced by magnet errors. Since particles of the same charge are circulated in opposite direction, separate magnetic fields are needed. The superconducting magnets are realized with NbTi Rutherford cables and operated at a temperature below 2 K. The coils for both

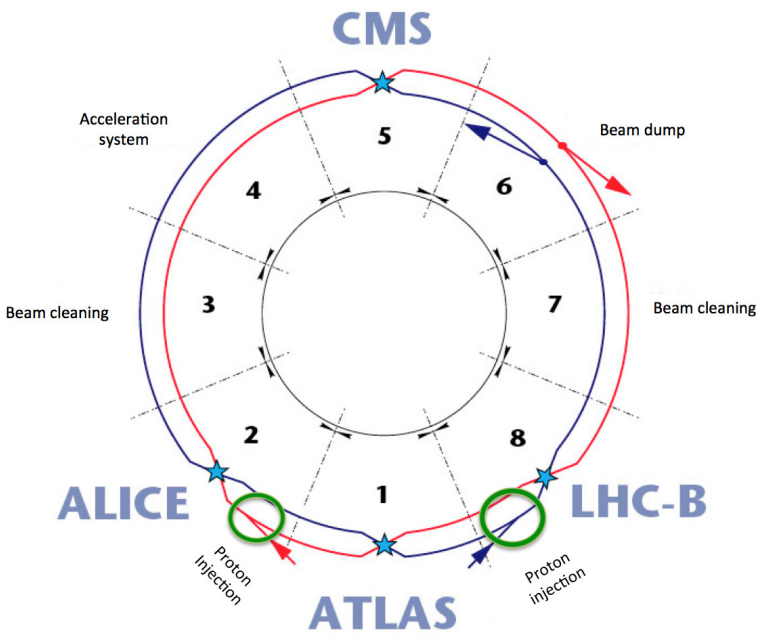

Figure 2.1: Illustration of the LHC ring with its eight sectors and both beams that are intersecting at four IPs [65].

directions are housed in one single mechanical structure [64].

The LHC is designed to reach a maximum center-of-mass energy of 14 TeV for protons, which circulate in $n_b = 2808$ bunches in each direction and are brought to collision in 25 ns intervals. Apart from the energy, the most important quantity for a collider experiment is the instantaneous luminosity L. The number of events that can be observed per time unit for a specific scattering process is proportional to L. For a symmetric collider it is given by

$$L = \frac{N_b^2 n_b f \gamma}{4\pi \varepsilon_n \beta^*} F_{\mathrm{hg}},$$

with the number n_b of bunches per beam, the number $N_b \approx 10^{11}$ of protons per bunch, the revolution frequency f, the Lorentz factor γ, the normalized emittance ε_n, and the value β^* of the beta-function at the interaction point. The hourglass factor F_{hg} accounts for the finite crossing angle of both beams. Instantaneous luminosities of up to $10^{34}\,\mathrm{cm}^{-2}\mathrm{s}^{-1} = 10\,\mathrm{Hz/nb}$ were planned initially. The integrated luminosity

$$\mathcal{L} = \int L \,\mathrm{d}t$$

is used to calculate total event counts

$$N_{\mathrm{evt}} = \mathcal{L} \cdot \sigma,$$

with the cross section σ for a specific process.

The collider can also accelerate fully stripped lead ions ($^{208}Pb^{82+}$) with beam energies of up to 2.76 TeV per nucleon, either operating in pPb or PbPb collision mode [64].

Different experiments are located around each IP. The CMS and ATLAS [66] experiments are general purpose detectors, built for conducting a broad range of physics measurements. With the LHCb experiment [67], realized as a forward spectrometer, mainly b-hadrons and their decays are studied at lower luminosities. The ALICE detector [68] is specialized for heavy ion physics. CMS and ATLAS also analyze the heavy ion collision data.

In Run I the LHC operated at $\sqrt{s} = 7\,\text{TeV}$ (2011) and $\sqrt{s} = 8\,\text{TeV}$ (2012) for pp collisions, followed by the long shutdown 1 (LS1) in which measures were taken to increase the energy closer to the design. Run II started in 2015 at $\sqrt{s} = 13\,\text{TeV}$ and continued in 2016, where the design luminosity was reached and even exceeded.

2.2 The CMS experiment

The data used in this thesis has been collected by the Compact Muon Solenoid (CMS) detector [69] located at IP5. Built around the collision point it spans approximately 20 m in length with a diameter of 15 m. The origin of the coordinate system is placed at the interaction point with the z axis parallel to the beam direction, pointing westwards, the x axis pointing towards center of the LHC, and the y axis pointing upwards. The azimuthal angle $\phi \in [-\pi, \pi]$ is measured from the x axis in the x-y plane and the polar angle $\vartheta \in [0, \pi]$ is usually substituted by the pseudorapidity $\eta = -\ln\tan\frac{\vartheta}{2}$. Distances in the η-ϕ plane are denoted $\Delta R = \sqrt{\Delta\phi^2 + \Delta\eta^2}$. The detector consists of several subcomponents each specialized to reconstruct different particle types and measure their trajectories, energies, or momenta. The subdetectors are divided into barrel and endcap parts, covering the central (small $|\eta|$) and forward (large $|\eta|$) regions, respectively. The general layout of these can be seen in Fig. 2.2.

CMS uses a superconducting solenoid magnet with a diameter of 6 m that weighs 220 t to bend charged particles' tracks in the x-y plane in order to determine their transverse momenta. Rutherford cables of NbTi are wound in four layers and carry a current of up to 19 kA. The interior of the magnet, which is occupied by the inner tracking system and the main calorimeters, is provided with a homogeneous 3.8 T magnetic field parallel to the beam direction. The magnetic flux is returned on the outside by an iron yoke, in which the muon system is embedded [69].

The innermost part of the detector is occupied by the silicon-based inner tracking system, built around the beam pipe, with a length of 5.8 m and a diameter of 2.5 m, used to reconstruct trajectories of charged particles and to identify interaction vertices and secondary vertices of e.g. b-hadron decays. Closest to the beam pipe, the pixel detector with a fine granularity ensures the ability to precisely determine track origins and vertices. Overall, it consists of 66 million pixels with a cell size of $100 \times 150\,\mu\text{m}^2$. The pixel detector is built in three layers in the barrel and two endcap disks. The innermost layer has a radius of 4.4 cm. Further outward, a silicon strip detector is used, consisting of ten barrel layers and twelve endcap disks with a total of 9.3 million

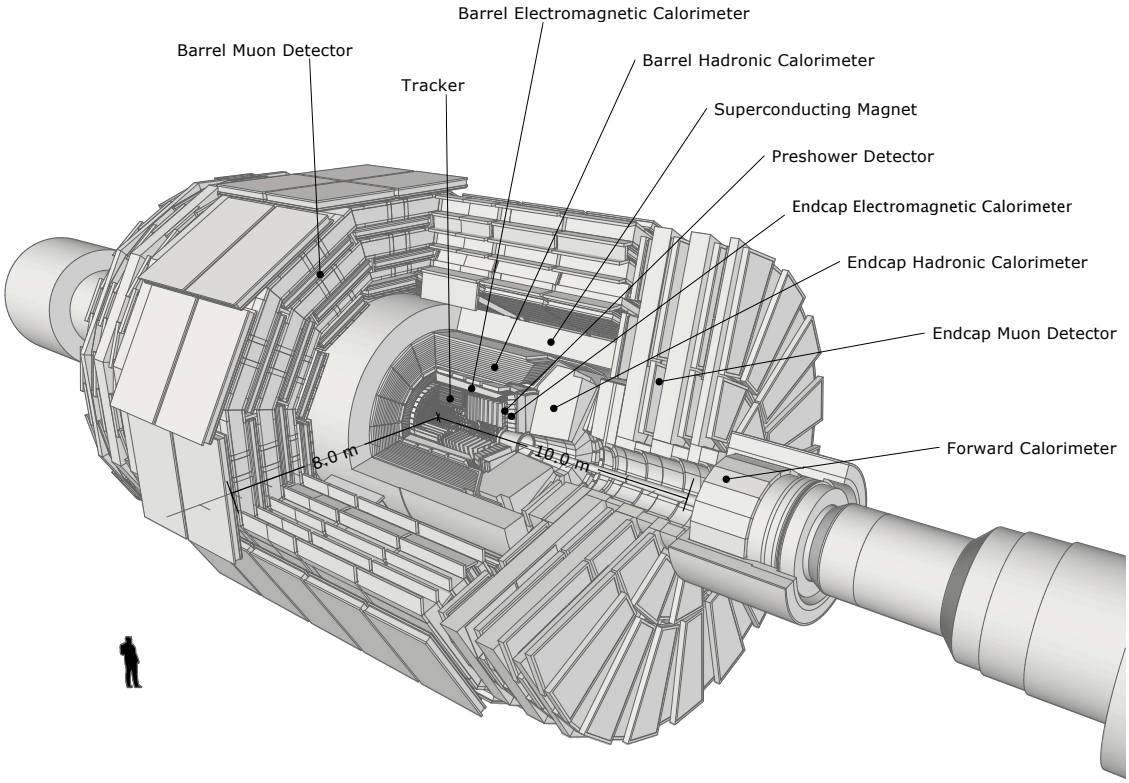

Figure 2.2: Schematic view of the CMS detector [70, 71]. The labels show the barrel and endcap subdetectors.

strips. The exact layout, subdivision, and pseudorapidity coverage of the inner tracking system is shown in Fig. 2.3. The total active silicon area of the tracker is approximately $200\,\mathrm{m}^2$ [69].

Around the tracker at an inner radius of 1.3 m, CMS is equipped with a homogeneous electromagnetic calorimeter (ECAL), mainly used to measure electron and photon energies. Lead tungstate ($PbWO_4$) crystals with a radiation length X_0 of 0.89 cm and a Molière radius of 2.2 cm serve as scintillating material. They are directed towards the collision point with a slight tilt to ensure that particles cannot pass gaps between the crystals. In the ECAL barrel (EB), covering $|\eta| < 1.479$, each of the 61200 crystals has a length of $23.0\,\mathrm{cm} \approx 25.8X_0$ and a front area of $22 \times 22\,\mathrm{mm}^2$. The ECAL endcaps (EE) each contain 7324 crystals with a length of $22.0\,\mathrm{cm} \approx 24.7X_0$ and a front cross section of $28.62 \times 28.62\,\mathrm{mm}^2$ that cover $1.479 < |\eta| < 3.0$. For the conversion of scintillation light into electrical signals avalanche photodiodes are used in the EB and vacuum phototriodes in the EE. The relative energy resolution can be parametrized with respect to the photon's or electron's energy E as

$$\left(\frac{\sigma}{E}\right)^2 = \left(\frac{2.8\%}{\sqrt{E/\,\mathrm{GeV}}}\right)^2 + \left(\frac{12\%}{E/\,\mathrm{GeV}}\right)^2 + (0.30\%)^2\,,$$

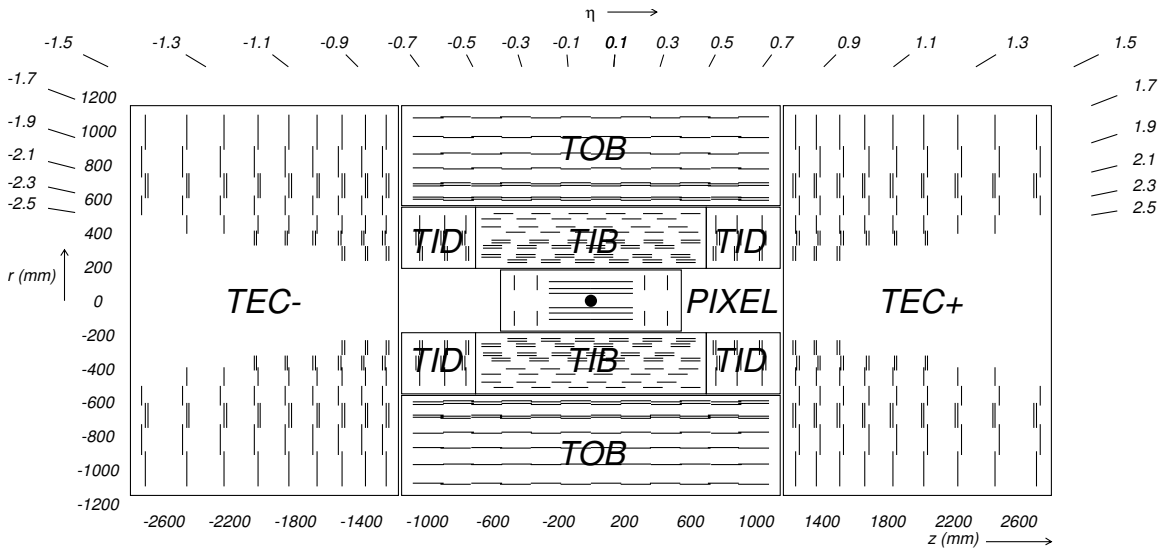

Figure 2.3: Schematic cross section of the CMS inner tracking system. The strip tracker is divided into inner and outer barrel (TIB, TOB), inner disks (TID) and endcaps (TEC). Each line represents a detector module [69].

where the numerical parameters have been determined in a beam test [72]. The first term is of stochastic origin, mainly due to the Poissonian distribution of the number of scintillation photons that are created. The second summand is attributed to noise from electronics and digitization. Other effects like the non-uniformity of the light collection, intercalibration errors, and energy leakage from the rear side of the crystals are contained in the last constant term. In order to identify the decay of neutral mesons to two photons, a preshower detector is placed in front of the ECAL for the region with $1.653 < |\eta| < 2.6$. It is realized as a sampling calorimeter with lead and silicon strip layers [69].

Between the ECAL and the magnet, i.e. at a radial distance between 1.77 m and 2.95 m in the barrel, the hadron calorimeter (HCAL) is responsible for measuring the energy of hadrons. It is built as a sampling calorimeter using layers of brass and plastic scintillators, while the front- and back-plates are made of steel. The barrel part ($|\eta| < 1.3$) consists of 36 azimuthal wedges and is segmented into parts covering 0.087×0.087 in $\Delta\eta \times \Delta\phi$. The 17 scintillator layers are read out with the help of hybrid photodiodes. In forward direction the endcaps cover a pseudorapidity of $1.3 < |\eta| < 3.0$. While for $|\eta| < 1.6$ the granularity is the same as in the barrel, it is decreased to $\Delta\eta \times \Delta\phi = 0.17 \times 0.17$ for $|\eta| > 1.6$. A further outer hadronic calorimeter is placed outside of the magnet for the barrel part. Hadrons passing the ECAL and HCAL can be detected using a scintillation detector making use of the stopping power of the magnet coil. A hadron forward calorimeter extends the pseudorapidity coverage up to $|\eta| = 5.2$. It is built of quartz fibres embedded in steel absorbers that detect Cherenkov light emitted by particles passing the detector and is therefore mainly sensitive to the electromagnetic shower component [69].

The muon system is placed outside of the magnet. In the barrel ($|\eta| < 1.2$) four stations of drift tube chambers are used to reconstruct muon trajectories. Cathode strip

chambers are employed in the endcaps ($0.9 < |\eta| < 2.4$), also arranged in four stations. Additionally, six barrel layers of resistive plate chambers and three disks per endcap are used mainly for triggering purposes [69].

To read out and store the detector signals, a trigger system is needed, because at a collision rate of 40 MHz it is impossible to store these for all collision events. The selection made by the trigger is designed to accept events in which potentially interesting physics processes occurred and is the first step of the event selection. The trigger is designed as a two-tiered system using a level-1 trigger (L1) and a high-level-trigger (HLT). For the L1 trigger simple information from the calorimeters and muon detectors is used. It is a hardware trigger implemented using custom programmable devices and it reduces the event rate from 40 MHz to $\mathcal{O}(10\,\text{kHz})$. A more sophisticated selection with a particle reconstruction closer to that used in the offline analysis is possible with the HLT, which is a software trigger running on computer farms. The HLT event output rate of $\mathcal{O}(100\,\text{Hz})$ can be handeled and stored to disk [69, 73].

In 2015, CMS recorded an integrated luminosity of $3.8\,\text{fb}^{-1}$ at a center-of-mass energy of 13 GeV with a maximum instantaneous luminosity of $0.5 \cdot 10^{34}\,\text{cm}^{-2}\text{s}^{-1}$. The history of the 2015 data taking can be seen in Fig. 2.4. Owing to issues with the operation of the experiment's magnet, only $2.3\,\text{fb}^{-1}$ of the data were recorded with full magnetic field, which are used in this analysis.

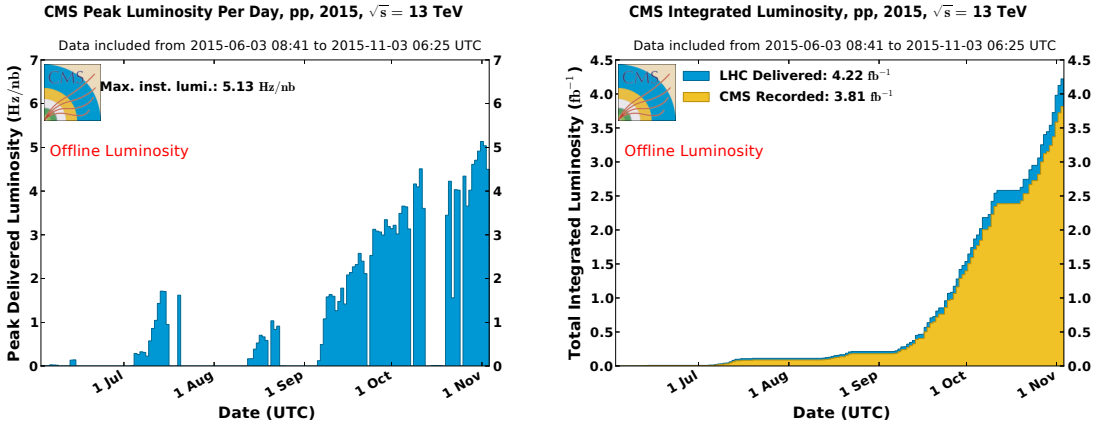

Figure 2.4: 2015 data taking performance. The instantaneous (left) and integrated (right) luminosity are shown as a function of the date. For the integrated luminosity, the delivered and recorded values are shown [74].

The problems with the magnet could be solved in the technical shutdown during winter 2015/2016 and the ongoing data taking in 2016 is progressing very well. Figure 2.5 shows the development of the integrated luminosity as a function of the date separately for each year of Run I and Run II. The data taking in 2016 is by far the most effective, reaching instantaneous luminosities of up to $1.3 \cdot 10^{34}\,\text{cm}^{-2}\text{s}^{-1}$, exceeding the design goal [74]. Up to mid-September approximately $30\,\text{fb}^{-1}$ of pp collisions have been recorded and data taking is foreseen to continue until the end of October 2016, promising a large dataset which will be the basis for many significant physics results.

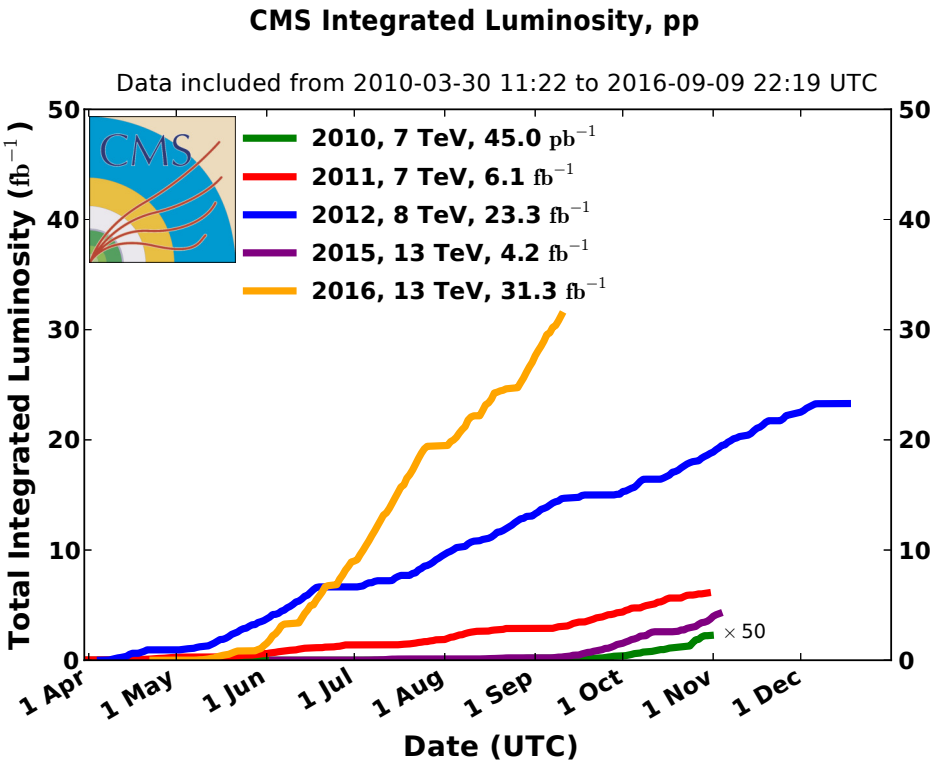

Figure 2.5: Integrated luminosity versus date delivered to CMS for pp collisions, shown separately for 2010, 2011, 2012, 2015 and 2016 data-taking [74]. The 2016 data-taking is forseen to continue until the end of October.

3

Event reconstruction and Monte-Carlo simulation

Contents

The analysis is performed starting from the MINIAOD data format which is a reduced version of Analysis Object Data (AOD), containing only a subset of the event information that is sufficient for most analyses [75]. The particle reconstruction described in Section 3.1 has been applied before and particle candidates are contained in AOD and MINIAOD. These datasets are further reduced in size by a first preselection step using the resources of the Worldwide LHC Computing Grid (WLCG) [76] with the help of the CMS software framework (CMSSW) in version 7.6.5 and CRAB3 [77]. The results are stored in the ROOT file format and the final analysis is performed on local computers with custom-written software making use of the ROOT libraries [78, 79].

In the following, the reconstruction of particles and quantities in single events is described. In general, one is interested in the products emerging from the interaction of two partons of the colliding protons, i.e. quarks or gluons, called the hard interaction. Additionally, there is the possibility that the remaining partons of the protons interact (multi-parton interactions), usually with a lower momentum transfer, resulting in additional low-energetic particles in the event. Multi-parton interactions together with the possible reconstruction of the proton-remnants are summarized as the underlying event. Additional pp interactions per bunch crossing are called pileup.

3.1 Particle reconstruction and identification

The signals that are read out from the different detector components need to be translated into physical information such as the trajectories of charged particles that traverse the detector and energies deposited in the calorimeters. In general, the particle-flow (PF) event reconstruction [80, 81] technique is used, which combines the information from all subdetectors to determine particle energies, momenta and trajectories with the best possible precision. In the following, the standard CMS reconstruction for the used

physics objects is briefly described, which is carried out centrally for all analyses. The object identification criteria applied in this analysis follow the official recommendations of the respective CMS physics object groups (POGs).

Since the initial boost in z direction of the colliding partons is unknown, only the transverse part of many quantities is considered. The transverse momentum $\vec{p}_{\mathrm{T}}$ is the vectorial projection of the momentum $\vec{p}$ onto the x-y plane, written $p_{\mathrm{T}} = |\vec{p}_{\mathrm{T}}|$ when only the absolute value is considered. In the high-energy limit that is assumed here, the masses of most particles are negligible and therefore $E \approx |\vec{p}|$. Although the energy is no vectorial quantity, transverse energies $E_{\mathrm{T}} \approx p_{\mathrm{T}}$ are used. In the high-energy limit, the pseudorapidity η is equal to the rapidity y relative to the beam axis,

$$y = \frac{1}{2} \ln \frac{E + p_z}{E - p_z} .$$

The reason for the usage of p_{T}, $\Delta\eta \approx \Delta y$, and ΔR is the Lorentz invariance with respect to boosts in z direction.

Electromagnetic objects

Electromagnetic objects, i.e. photons and electrons, mainly deposit their energy in the ECAL. Electron trajectories can additionally be reconstructed using the hits in the inner tracking system. A large fraction of photons converts to e^+e^- pairs before reaching the ECAL, which diverge in ϕ due to the magnetic field. Electrons can emit photons by bremsstrahlung, which also can convert in the inner tracking system. To associate all energy deposits to the right objects, the PF algorithm is used for a consistent global event description (GED) [82], in contrast to the Run I approach, in which ECAL clusters were built independently and then eventually matched to tracks [83, 84].

Photons and electrons are reconstructed in a consistent way. First of all, ECAL cluster seeds are determined as local maxima in the energy deposits. Starting from a seed, adjacent ECAL crystals are subsequently added to a PF cluster if their energy exceeds a certain threshold to reject noise. Different PF clusters can share the energy deposited in a single crystal with a fraction dependent on the crystal's distance to the clusters. Superclusters are merged dynamically from several clusters taking into account energy-dependent $\Delta\eta$-$\Delta\phi$ correlations expected for bremsstrahlung and conversions. Tracks are found with a Kalman filter [85] and are refitted using a Gaussian sum filter which can model the energy loss of electrons [86]. Using these, the superclusters are refined by identifying additional ECAL clusters and tracks compatible with radiated photons or conversions. Matching tracks and ECAL clusters are merged into a single PF object to avoid double-counting for the calculation of further PF-based quantities like missing transverse energy.

At this stage no explicit decision is made whether an electromagnetic object is classified as an electron or photon for the further analysis, i.e. the same object can be contained in the photon collection as well as in the electron collection. Identification criteria for the differentiation are applied on analysis level, as described below.

Photons

Only photons reconstructed in the barrel part of the ECAL are used in this analysis, since photons in the considered SUSY models are produced more centrally compared to SM background, due to high masses of the mother particles. The energy and direction of a reconstructed photon are completely determined by the corresponding supercluster. To ensure full shower containment, the two outermost crystals cannot serve as a seed crystal, restricting the EB fiducial region to $|\eta| < 1.4442$.

For the reconstructed photons, a set of identification criteria has to be applied to reject non-photon objects while keeping a high photon identification efficiency.

Often jets are also reconstructed as photons, due to an electromagnetic component. In particular neutral mesons, such as the π^0, can be produced in the hadronization and decay to two photons. Variables quantifying the shape of the shower and the amount of energy deposited by other particles in the detector around the photon candidate are used to identify prompt photons.

The ratio H/E, also called hadronic leakage, of the energy H deposited in the HCAL towers behind the supercluster and the energy E of the supercluster is generally increased for jets.

Isolation energy is calculated as the scalar sum of transverse momenta of PF objects reconstructed in a cone of $\Delta R < 0.3$ around the photon candidate and is separated into charged hadron ($\mathrm{Iso}_{\pm}$), neutral hadron (Iso_0), and photon (Iso_γ) isolation. The photon candidate itself is removed from the isolation calculation. Contributions from pileup are removed from Iso_0 and Iso_γ by subtracting $\rho \cdot A_{\mathrm{eff}}$, where ρ is the median transverse energy density in the event and A_{eff} the effective area of the photon cone multiplied by an η-dependent factor that accounts for the non-isotropic distribution of the energy density. Charged hadrons not originating from the primary vertex are identified as pileup and not considered in the charged hadron isolation calculation. The primary vertex is defined as the vertex with the largest sum of p_{T}^2 of originating tracks. For prompt photons the isolation energies are expected to be lower than for jets.

Jets also have a wider electromagnetic shower shape than photons, which is quantified as a weighted variance

$$\sigma^2_{i\eta i\eta} = \frac{\sum\limits_{i\in 5\times 5} w_i(\hat{\eta} - \eta_i)^2}{\sum\limits_{i\in 5\times 5} w_i}, \quad w_i = \max\left\{0, 4.7 + \ln\frac{E_i}{E_{5\times 5}}\right\},$$

where the sums run over the 5×5 ECAL crystal array around the seed crystal at $\hat{\eta}$, excluding the central crystal. The weights w_i account for the single crystals' energy contributions to the whole 5×5 array's energy $E_{5\times 5}$.

The CMS e/gamma POG, responsible for electron and photon reconstruction and identification, recommends different sets of selection criteria using these variables, each giving a different selection efficiency and background rejection [87]. For this analysis the "loose working point", defined in Table 3.1, is used, which provides the largest selection efficiency.

The electromagnetic showers induced by electrons in the ECAL cannot be distinguished from those of photons. To reject electrons, a pixel seed veto is used, which

Table 3.1: Loose working point identification criteria for photons reconstructed in the ECAL barrel (`SPRING15 selections 25 ns`) [87]. The thresholds for the neutral hadron and photon isolations are photon-p_{T} dependend.

H/E	$<$	0.05
$\sigma_{i\eta i\eta}$	$<$	0.0102
$\mathrm{Iso}_{\pm}$ [GeV]	$<$	3.32
Iso_{0} [GeV]	$<$	$1.92 + 0.014 \cdot p_{\mathrm{T}}$ [GeV] $+ 0.000019 \cdot (p_{\mathrm{T}}$ [GeV]$)^2$
Iso_{γ} [GeV]	$<$	$0.81 + 0.0053 \cdot p_{\mathrm{T}}$ [GeV]

makes use of the fact that electrons produce hits in the inner tracking system. Photon candidates are rejected if there exists a hit pattern in the pixel detector that can be used to fit a track to the candidate's supercluster.

In addition to the standard identification criteria, photons need to have a finite shower width to veto spontaneous discharges of the avalanche photodiodes used in the EB. Such a random discharge gives a signal in a single crystal leading to an unphysically large energy entry, called ECAL spike. This is suppressed by requiring $\sigma_{i\eta i\eta} > 0.001$ and $\sigma_{i\phi i\phi} > 0.001$, where $\sigma_{i\phi i\phi}$ is defined like $\sigma_{i\eta i\eta}$, but in ϕ-direction. The effect of these requirements is further reviewed in Section 4.5.

All used photons are required to be reconstructed with $|\eta| < 1.4442$ and $p_{\mathrm{T}} > 15\,\mathrm{GeV}$.

Leptons

Leptons are not required for the event selection, but the number of leptons is used to define regions used for the validation of the background prediction (see Section 4.4). Only electrons and muons are considered explicitly, while tau leptons can only implicitly enter by the selection of its decay products, and no distinction is made between positive and negative charge.

The electron reconstruction has been described above together with the photon reconstruction. To finally identify electrons, different quantities are used. In addition to those already described in the context of the photon identification, variables are used that exploit the imprint left by electrons in the inner tracking system [84]. The transverse (d_0) and longitudinal (d_z) distance of closest approach of the track to the primary vertex is used to ensure that electrons originate directly from the hard interaction. To verify that the track and the associated supercluster are compatible, the distance of supercluster and the extrapolated track is measured in $\Delta\eta_{\mathrm{SC,\,tr}}$ and $\Delta\phi_{\mathrm{SC,\,tr}}$, and the supercluster energy E_{SC} and track momentum p are compared as $E_{\mathrm{SC}}^{-1} - p^{-1}$. The number of missing hits along the trajectory in the tracking system due to the finite hit efficiency is restricted and photon conversions are vetoed using the χ^2 probability of a fit assuming two electrons originating from a single photon conversion vertex. The charged hadron, neutral hadron and photon isolations are calculated as for photons in a cone of $\Delta R < 0.3$, but summed up and divided by the electron p_{T}, i.e. treated as a relative isolation $\mathrm{Iso}_{\mathrm{rel}}$. Using these variables, the tight identification working point provided by the e/gamma POG, listed in Table 3.2, is used [88].

Muons are reconstructed using information from the inner tracking system in combi-

Table 3.2: Tight working point identification criteria for electrons (`SPRING15 selections 25 ns`) [88].

		Barrel	Endcap
$\sigma_{i\eta i\eta}$	$<$	0.0101	0.0279
$\lvert\Delta\eta_{\mathrm{SC,\,tr}}\rvert$	$<$	0.00926	0.00724
$\lvert\Delta\phi_{\mathrm{SC,\,tr}}\rvert$	$<$	0.0336	0.0918
H/E	$<$	0.0597	0.0615
$\mathrm{Iso}_{\mathrm{rel}}$	$<$	0.0354	0.0646
$\left\lvert E_{\mathrm{SC}}^{-1} - p^{-1}\right\rvert$ [GeV^{-1}]	$<$	0.012	0.00999
$\lvert d_0\rvert$ [cm]	$<$	0.0111	0.0351
$\lvert d_z\rvert$ [cm]	$<$	0.0466	0.417
exp. missing inner hits	$\leq$	2	1
pass conversion veto		yes	yes

nation with the dedicated outer muon system. If tracks in both systems can be matched, all hits are combined into a "global muon" fit used by the PF algorithm [89]. Further identification criteria, corresponding to the Muon POG tight selection [90], are applied, which are listed in Table 3.3. These include the χ^2 per number of degrees of freedom (χ^2/N_{df}) of the global fit, the number of used muon chamber hits, and the number of muon stations matched to the track. From the inner tracking system, the number of hits in the pixel detector and the number of tracker layers with hits are used. The impact parameter values d_0 and d_z are also considered.

Table 3.3: Tight working point identification criteria for muons, with the relative isolation requirement explicitly included [90].

χ^2/N_{df}	$<$	10
N(muon chamber hits)	$>$	0
N(matched stations)	$>$	1
$\lvert d_0\rvert$ [cm]	$<$	0.2
$\lvert d_z\rvert$ [cm]	$<$	0.5
N(pixel hits)	$>$	0
N(tracker layers)	$>$	5
$\mathrm{Iso}_{\mathrm{rel}}$	$<$	0.15

Jets

The hadrons from the hadronization of quarks and gluons are collimated into jets in the direction of the initial particle. They need to be reconstructed and clustered to separate jet candidates to determine their direction and momentum.

PF objects are clustered with the anti-k_t clustering algorithm [91] with a distance parameter D of 0.4 using the FastJet package [92,93]. Each particle is initially considered as a pseudo-jet and two pseudo-jets are merged sequentially until a stop criterion

is fulfilled. In each iteration a distance measure

$$d_{ij} := \min\left\{k_{\mathrm{T}i}^{-2}, k_{\mathrm{T}j}^{-2}\right\} \cdot \frac{\Delta_{ij}^2}{D^2}$$

is calculated for all pseudo-jet pairs (i, j), where k_T denotes the transverse momentum of a pseudo-jet and Δ_{ij} the euclidean distance in y-ϕ space. The pseudo-jet pair (i, j) with the smallest distance d_{ij} is merged to a single pseudo-jet for the next iteration. Once the distance $d_{iB} := k_{\mathrm{T}i}^{-2}$ of a pseudo-jet i to the beam axis is the smallest of the distances, it is called a jet and no longer considered in the following iterations. The distance parameter D determines roughly the size of the jet cone.

To reduce the influence of pileup on jets the charged hadron subtraction technique is used [94], rejecting charged hadrons not originating from the hard interaction vertex. For the jet energy calibration, the standard corrections provided by the Jet/MET POG are applied [95, 96], including an energy offset correction to account for pileup and the underlying event, a detector response correction to account for p_T and η dependent nonlinear responses, and residual corrections for differences between data and simulation.

Only jets with $p_\mathrm{T} > 30\,\mathrm{GeV}$ reconstructed within $|\eta| < 3.0$ that fulfill the jet identification criteria are considered [97]. A jet has to have more than one constituent and the fraction of the energy contributed by neutral hadrons and neutral electromagnetic objects each cannot exceed 99%. For jets with $|\eta| < 2.4$, additionally the charged hadron fraction and the multiplicity of charged constituents has to be greater than zero, and the charged electromagnetic fraction must be smaller than 99%. The jet energy scale (JES) and resolution (JER) [98] corresponding to version `Fall15_25nsV2` are used. Since leptons and photons are mostly also clustered as jets, jets containing a photon, electron, or muon in $\Delta R < 0.4$ are explicitly discarded.

Jets initiated by b-quarks (b-jets) can be identified with a certain efficiency, because the b-hadrons in the jet have a lifetime that is so short that they decay within the beam pipe, but long enough to be able to distinguish their decay vertex (secondary vertex) from the primary interaction vertex by extrapolating the tracks of the decay products. For the identification of b-jets, b-tagging is performed using the Combined Secondary Vertex algorithm [99, 100]. The chosen tight working point corresponds to a b-tagging efficiency of $\varepsilon_\mathrm{b} \approx 49\%$ and a misidentification rate of $\approx 0.1\%$. It is used in a control region for the background estimation (see Section 4.1), but not for the signal selection. The medium and loose working points are also used for cross checks.

3.2 Observable definitions

The reconstructed objects and their properties are combined to several other observables. These are mainly used to define selections with a good signal-background separation, but also for the validation of background prediction methods.

Missing transverse energy $E_\mathrm{T}^\mathrm{miss}$ is the absolute value of the negative vectorial sum

of the transverse momenta of all reconstructed particles,

$$E_{\mathrm{T}}^{\mathrm{miss}} \equiv \left|\vec{E}_{\mathrm{T}}^{\mathrm{miss}}\right| \text{, with}$$
$$\vec{E}_{\mathrm{T}}^{\mathrm{miss}} := -\sum_{i\in\text{particles}} \vec{p}_{\mathrm{T}}^{\,i},$$

calculated from PF objects. It is expected to be low for SM processes not containing neutrinos, but the finite detector resolution can cause substantial reconstructed missing transverse energy, even for genuinely balanced processes, especially if jets are present. The jet energy corrections are propagated to $E_{\mathrm{T}}^{\mathrm{miss}}$.

The variable S_{T}^{γ} is the scalar sum of $E_{\mathrm{T}}^{\mathrm{miss}}$ and the transverse momenta of all photons in an event,

$$S_{\mathrm{T}}^{\gamma} := E_{\mathrm{T}}^{\mathrm{miss}} + \sum_{i\in\text{photons}} |\vec{p}_{\mathrm{T}}^{\,i}|,$$

which is used for the final interpretation of the search.

The hadronic activity H_{T} is calculated as the scalar sum of all jet transverse momenta,

$$H_{\mathrm{T}} := \sum_{i\in\text{jets}} |\vec{p}_{\mathrm{T}}^{\,i}|,$$

only using jets identified as described in Section 3.1.

The transverse mass $M_{\mathrm{T}} \equiv M_{\mathrm{T}}(\gamma_1, E_{\mathrm{T}}^{\mathrm{miss}})$ of the leading photon γ_1, i.e. the photon with the largest p_{T}, and $E_{\mathrm{T}}^{\mathrm{miss}}$ is calculated like the invariant mass, but only using the transverse energy and momentum,

$$M_{\mathrm{T}}^2 := 2E_{\mathrm{T}}^{\mathrm{miss}} p_{\mathrm{T}}^{\gamma}\left[1 - \cos\Delta\phi\left(E_{\mathrm{T}}^{\mathrm{miss}}, \gamma\right)\right].$$

In an event where only a single NLSP→γ+LSP decay occured, M_{T} would correspond to the transverse mass of the NLSP. This is smeared by the second LSP emerging in the event, resulting in generally large values of M_{T}, because the NLSP is generally heavier than SM particles.

$E_{\mathrm{T}}^{\mathrm{miss}}$ significance ($\mathcal{S}$)

Even for processes for which all final state particles are detected, the reconstructed $E_{\mathrm{T}}^{\mathrm{miss}}$ can be large, due to the finite detector resolution. This is especially the case for events containing jets, because they are reconstructed with a much larger uncertainty than most other particles, owing to the resolution of the HCAL which is worse than that of the other subdetectors.

To be able to separate genuine from instrumental $E_{\mathrm{T}}^{\mathrm{miss}}$, the $E_{\mathrm{T}}^{\mathrm{miss}}$ significance ($\mathcal{S}$) is used [101–103]. The dimensionless variable is defined using a likelihood ratio

$$\mathcal{S} := 2\ln\frac{\mathcal{L}(\vec{\varepsilon}_{\mathrm{T}} = \vec{E}_{\mathrm{T}}^{\mathrm{miss}})}{\mathcal{L}(\vec{\varepsilon}_{\mathrm{T}} = 0)}$$

with the true $\vec{\varepsilon}_{\mathrm{T}}$ and measured $\vec{E}_{\mathrm{T}}^{\mathrm{miss}}$ missing transverse energy. The numerator is the likelihood that $\vec{\varepsilon}_{\mathrm{T}}$ is equal to the reconstructed missing transverse energy, which is compared to the likelihood of the true missing transverse energy being zero in the denominator.

If the transverse energy resolution $(\sigma^i_{p_{\mathrm{T}}}, \sigma^i_{\phi})$ of a particle i in an event is known, it can be expressed as a diagonal 2×2 matrix in a coordinate system with the x-axis parallel to its transverse momentum, $\vec{x}_i \parallel \vec{p}^{\,i}_{\mathrm{T}}$, which can be rotated into the CMS coordinate system using a matrix $R(\phi_i)$. The $E_{\mathrm{T}}^{\mathrm{miss}}$ covariance matrix V can be constructed from all particles in an event,

$$V = \sum_{i \in \text{particles}} R(\phi_i) \underbrace{\begin{bmatrix} {\sigma^i_{p_{\mathrm{T}}}}^2 & 0 \\ 0 & {p^i_{\mathrm{T}}}^2 {\sigma^i_{\phi}}^2 \end{bmatrix}}_{\text{in coordinates with } \vec{x}_i \parallel \vec{p}^{\,i}_{\mathrm{T}}} R^{-1}(\phi_i)\,.$$

With this, a gaussian approximation of the likelihood

$$\mathcal{L}(\vec{\varepsilon}_{\mathrm{T}}) = \frac{1}{2\pi |V|^{1/2}} \exp\left(-\frac{1}{2} (\vec{\varepsilon}_{\mathrm{T}} - \vec{E}_{\mathrm{T}}^{\mathrm{miss}})^{\mathrm{T}} V^{-1} (\vec{\varepsilon}_{\mathrm{T}} - \vec{E}_{\mathrm{T}}^{\mathrm{miss}}) \right)$$

leads to

$$\mathcal{S} = (\vec{E}_{\mathrm{T}}^{\mathrm{miss}})^{\mathrm{T}} V^{-1} \vec{E}_{\mathrm{T}}^{\mathrm{miss}}\,.$$

The resolution parameters are tuned by the Jet/MET POG. More details can be found in [101–103].

It should be noted that $\mathcal{S}$ is not to be interpreted as a number of gaussian standard deviations. It can be shown that it is approximately proportional to the square of such a measure. Since the $E_{\mathrm{T}}^{\mathrm{miss}}$ resolution $\sigma_{E_{\mathrm{T}}^{\mathrm{miss}}}$ is often approximated as $\sqrt{H_{\mathrm{T}}}$, the quantity $E_{\mathrm{T}}^{\mathrm{miss}}/\sqrt{H_{\mathrm{T}}}$ can also be used to simplify $\mathcal{S}$, though with worse discrimination power,

$$\mathcal{S} \sim \frac{{E_{\mathrm{T}}^{\mathrm{miss}}}^2}{\sigma^2_{E_{\mathrm{T}}^{\mathrm{miss}}}} \sim \left(\frac{E_{\mathrm{T}}^{\mathrm{miss}}}{\sqrt{H_{\mathrm{T}}}} \right)^2 .$$

The variable $E_{\mathrm{T}}^{\mathrm{miss}}/\sqrt{H_{\mathrm{T}}}$ is not used in this analysis, because it lacks discrimination power for events not containing jets passing the identification criteria or the energy threshold. Such events all have $E_{\mathrm{T}}^{\mathrm{miss}}/\sqrt{H_{\mathrm{T}}} = \infty$, while the $\mathcal{S}$ calculation does not depend on the jet identification and also tracks and energy deposits that are not clustered are taken into account.

The distribution of $\mathcal{S}$ for different processes after the preselection (described in Section 3.4) is shown in Fig. 3.6 (middle, right) on page 36.

3.3 Datasets and simulation

The output of several HLT paths is grouped into different primary datasets (PDs), in which an event is stored if it is accepted by one of the contained triggers. For the main

analysis, the Single Photon PD is used to which the signal trigger is associated. In addition, the MET PD is needed for the trigger efficiency measurement (described in Section 3.4) that employs a $E_{\mathrm{T}}^{\mathrm{miss}}$ trigger. The exact PD paths in the dataset bookkeeping service (DBS) [104] are listed in Table 3.4. Only 25 ns bunch spacing data taken in

Table 3.4: DBS paths of the used primary datasets.

/SinglePhoton/Run2015D-16Dec2015-v1/MINIAOD
/MET/Run2015D-16Dec2015-v1/MINIAOD

2015 with full magnetic field are considered. The `16Dec2015` reconstruction is used, corresponding to `CMSSW 76X`. Only events that passed the official certification encoded in the `Cert_13TeV_16Dec2015ReReco_Collisions15_25ns_JSON_v2.txt` JSON file are used. The total integrated luminosity of this configuration is $2.3\,\mathrm{fb}^{-1}$.

Background processes are simulated using Monte-Carlo (MC) event generators. For the generation and reconstruction, `CMSSW 76X` is used. All used background samples are listed in Table 3.5 together with the corresponding number of generated events and the cross section, which in most cases corresponds to the order in which they are generated. If a higher-order cross section is available for a process, it is listed in the table and described in the following. For some processes higher-order correction factors (k-factors) are available, as listed below. These are not yet applied to the cross sections given in the table.

The QCD multijet and γ+jets, as well as the $\mathrm{Z}(\rightarrow \nu\nu)$+jets/W+jets samples are generated in bins of H_{T} to ensure that enough events are generated in the high-energetic regime to achieve a sufficient statistical precision. For the same reason, some samples are only generated for a photon p_{T} larger than 130 GeV. The $\mathrm{t\bar{t}}(+\gamma)$ processes are generated at next-to-leading-order (NLO) precision with MadGraph mc@nlo, while all other samples are generated with MadGraph in leading order (LO) in the strong coupling α_s [105], except WW for which powheg is used [106–110]. The fragmentation and hadronization are handled with pythia 8 [111, 112] and the detector response is modeled with Geant4 [113].

The $\mathrm{Z}+\gamma$ samples are corrected with the photon-p_{T} dependent next-to-next-to-leading-order (NNLO) k-factors listed in Table 3.6 [114]. The W and $\mathrm{Z}(\rightarrow \nu\nu)$ simulation is scaled with constant NLO k-factors and a constant NNLO k-factor is applied for $\mathrm{W}+\gamma$ (see Table 3.7). Cross sections for diboson processes are available in NLO (ZZ, WZ) and NNLO (WW) [115].

All simulated processes are scaled with a factor $\mathcal{L}\cdot\sigma/N_{\mathrm{gen}}$, with the respective number N_{gen} of generated events and the corresponding cross section σ, to achieve an effective integrated luminosity of the simulation corresponding to the recorded value $\mathcal{L}$. Additionally, the generated samples are weighted on an event-by-event basis to match the number of primary interactions per bunch crossing (pileup) to the data. For the MadGraph mc@nlo simulations, event weights returned by the generator are applied, which correct for the possible double counting of generated higher order processes and radiation in the shower simulation that describe the same phase space.

For simulated events, generator matching can be applied to verify the performance of methods used on reconstruction level. An example of its usage is the validation of the

Table 3.5: Simulated background samples with the corresponding numbers N_{gen} of generated events and the cross sections. The cross sections are given to the order used by the generator, if no order is explicitly specified in the text. Any k-factors that are used are not yet applied to these values. Some samples are generated in H_{T} intervals or only above a photon p_{T} threshold.

Sample		N_{gen}	σ [pb]
$\text{Z}(\to \nu\nu) + \gamma$	$p_{\text{T}}(\gamma) > 130\,\text{GeV}$	$0.50 \cdot 10^6$	0.223
$\text{Z}(\to \ell\ell) + \gamma$	$p_{\text{T}}(\gamma) > 130\,\text{GeV}$	$0.49 \cdot 10^6$	0.143
$\text{W} + \gamma$	$p_{\text{T}}(\gamma) > 130\,\text{GeV}$	$0.50 \cdot 10^6$	0.834
γ + jets	$H_{\text{T}} = 40 - 100\,\text{GeV}$	$4.4 \cdot 10^6$	20790
	$H_{\text{T}} = 100 - 200\,\text{GeV}$	$5.1 \cdot 10^6$	9238
	$H_{\text{T}} = 200 - 400\,\text{GeV}$	$10.5 \cdot 10^6$	2305
	$H_{\text{T}} = 400 - 600\,\text{GeV}$	$2.4 \cdot 10^6$	274.4
	$H_{\text{T}} > 600\,\text{GeV}$	$2.5 \cdot 10^6$	93.46
QCD multijet	$H_{\text{T}} = 100 - 200\,\text{GeV}$	$82.1 \cdot 10^6$	27990000
	$H_{\text{T}} = 200 - 300\,\text{GeV}$	$18.8 \cdot 10^6$	1712000
	$H_{\text{T}} = 300 - 500\,\text{GeV}$	$16.9 \cdot 10^6$	347700
	$H_{\text{T}} = 500 - 700\,\text{GeV}$	$19.4 \cdot 10^6$	32100
	$H_{\text{T}} = 700 - 1000\,\text{GeV}$	$15.5 \cdot 10^6$	6831
	$H_{\text{T}} = 1000 - 1500\,\text{GeV}$	$5.0 \cdot 10^6$	1207
	$H_{\text{T}} = 1500 - 2000\,\text{GeV}$	$3.9 \cdot 10^6$	119.9
	$H_{\text{T}} > 2000\,\text{GeV}$	$2.0 \cdot 10^6$	25.24
$\text{Z}(\to \nu\nu)$	$H_{\text{T}} = 100 - 200\,\text{GeV}$	$5.2 \cdot 10^6$	280.47
	$H_{\text{T}} = 200 - 400\,\text{GeV}$	$5.1 \cdot 10^6$	78.36
	$H_{\text{T}} = 400 - 600\,\text{GeV}$	$1.0 \cdot 10^6$	10.94
	$H_{\text{T}} > 600\,\text{GeV}$	$1.0 \cdot 10^6$	4.20
$\text{W}(\to \ell\,\nu)$	$H_{\text{T}} = 100 - 200\,\text{GeV}$	$10.2 \cdot 10^6$	1345
	$H_{\text{T}} = 200 - 400\,\text{GeV}$	$4.9 \cdot 10^6$	359.7
	$H_{\text{T}} = 400 - 600\,\text{GeV}$	$1.9 \cdot 10^6$	48.91
	$H_{\text{T}} = 600 - 800\,\text{GeV}$	$3.8 \cdot 10^6$	12.05
	$H_{\text{T}} = 800 - 1200\,\text{GeV}$	$1.6 \cdot 10^6$	5.501
	$H_{\text{T}} = 1200 - 2500\,\text{GeV}$	$0.25 \cdot 10^6$	1.329
	$H_{\text{T}} > 2500\,\text{GeV}$	$0.25 \cdot 10^6$	0.03216
$\text{t}\bar{\text{t}} + \gamma$		$1.6 \cdot 10^6$	3.697
$\text{t}\bar{\text{t}}$		$12.8 \cdot 10^6$	831.76
$\text{WW}(\to 2\ell\ 2\nu)$		$2.0 \cdot 10^6$	12.178
$\text{WW}(\to \ell\,\nu\ \text{qq})$		$1.9 \cdot 10^6$	49.997
ZZ		$1.0 \cdot 10^6$	16.523
WZ		$1.0 \cdot 10^6$	47.13

Table 3.6: The p_T-dependent NNLO k-factors used for $Z + \gamma$ [114].

$p_T(\gamma)$ [GeV]		k_{NNLO}
175–	190	1.39
190–	250	1.35
250–	400	1.30
400–	700	1.23
700–	∞	1.23

Table 3.7: (N)NLO k-factors for different samples. The $W + \gamma$ factor is only valid for photon $p_T > 175$ GeV.

Process	Correction level	$k_{(N)NLO}$
$W + \gamma$	NNLO	1.34
W	NLO	1.21
$Z(\rightarrow \nu\nu)$	NLO	1.23

background prediction described in Section 4.2. To match generated and reconstructed objects, an upper limit on the distance ΔR is used, sometimes in combination with a requirement concerning the relative p_T deviation. Both quantities are not expected to be exactly equal to zero, because of the finite detector resolution and imperfect reconstruction methods. An example of the two-dimensional matching distribution using both quantities is shown in Fig. 3.1 for generated and reconstructed photons. The aggregation of entries at $|\Delta p_T|/p_T \approx 1$ is due to generated photons with low transverse momentum. Exact selection requirements are given in the text, when used the following analysis.

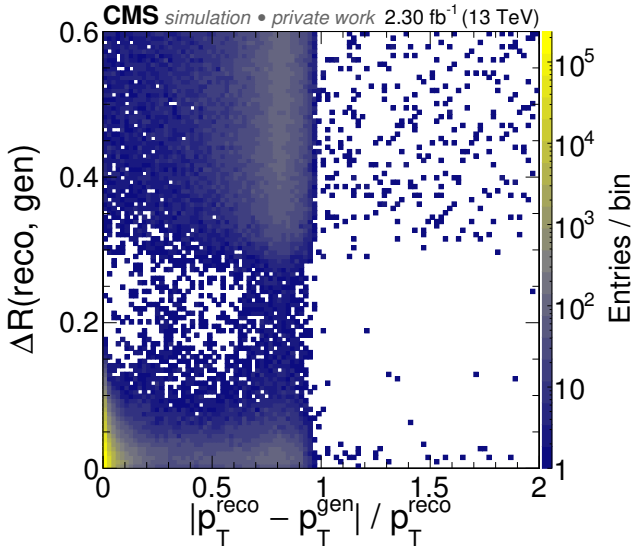

Figure 3.1: Matching of generated (gen) and reconstructed (reco) photons. The distance in ΔR is shown vs. the relative transverse momentum deviation.

Signal simulation

A simplified description of the detector response (fast simulation) is used for the signal simulation to save computing time [116]. The precision of the $\mathcal{S}$ calculation in fast simulation has been evaluated in the $\sqrt{s} = 8\,\text{TeV}$ analysis and was found to be compatible with the calculation using the full detector simulation [58]. The simplified models are generated using LO MADGRAPH simulation in CMSSW 80X and NLO cross sections for the production are used [117–119]. These samples are provided centrally for the CMS SUSY group. It has been verified that the reconstruction does not show significant differences when comparing the fast simulation implemented in the CMSSW software releases 8 and 7. The cross sections of chargino-neutralino production and gluino pair production used for the simplified models are visualized in Fig. 3.2.

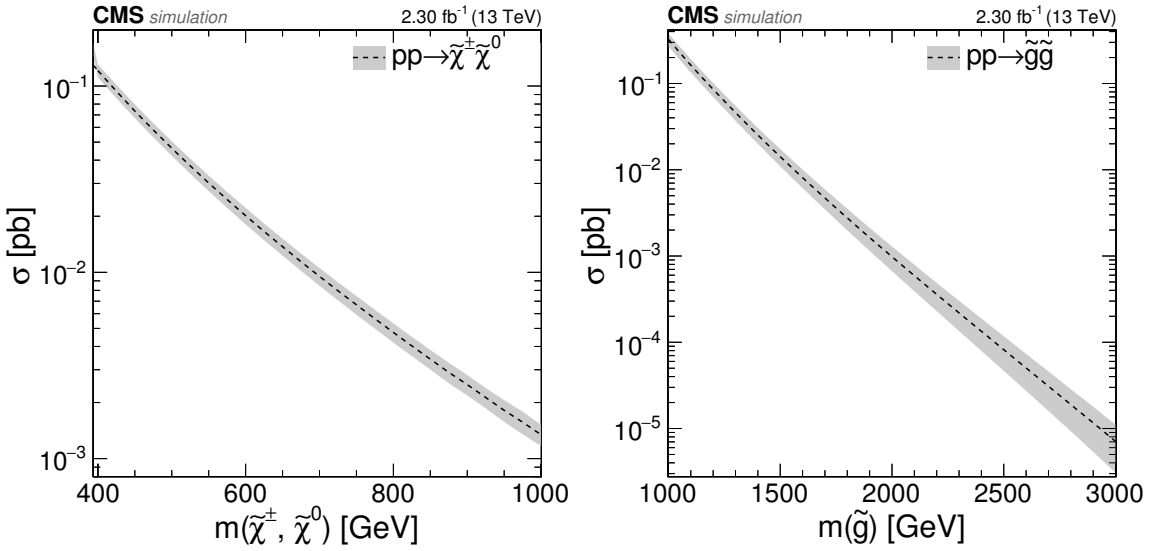

Figure 3.2: The cross sections of chargino-neutralino production (left) and gluino pair production (right) as functions of the respective masses, as used for the simplified models. The gray bands represent the theoretical uncertainty estimate [1].

GGM signal points are simulated privately with PYTHIA 8 in CMSSW 74X using the SUSY Les Houches Accord (SLHA) files for the "Wino-Bino grid" [43] and NLO cross sections are calculated using PROSPINO [120], which are shown in Fig. 3.3 as a function of the bino and wino masses. The NLSP decay is not encoded in the SLHA files and was automatically handled by PYTHIA 6, which was used in the predecessor analysis. For the usage with PYTHIA 8, which does no longer support the automatic NLSP decay, the decays $\widetilde{\chi}_1^0 \to \widetilde{\text{G}}\gamma$ and $\widetilde{\chi}_1^0 \to \widetilde{\text{G}}\text{Z}$ are added manually to the files, following Eq. (1.2), which is vizualized in Fig. 1.2. To verify the correctness of this procedure, GGM signal has also been generated at $\sqrt{s} = 8\,\text{TeV}$ and compared to the old PYTHIA 6 simulation. Figure 3.4 shows the comparison of the resulting distributions for the generated p_T of the photon and the gravitino, both agreeing well. The private production has been presented to and approved by the SUSY MC/Trigger group [121]. Technical details are documented in Appendix A.

For technical reasons, the Gravitino mass is set to 1 GeV in the simulation. The fast

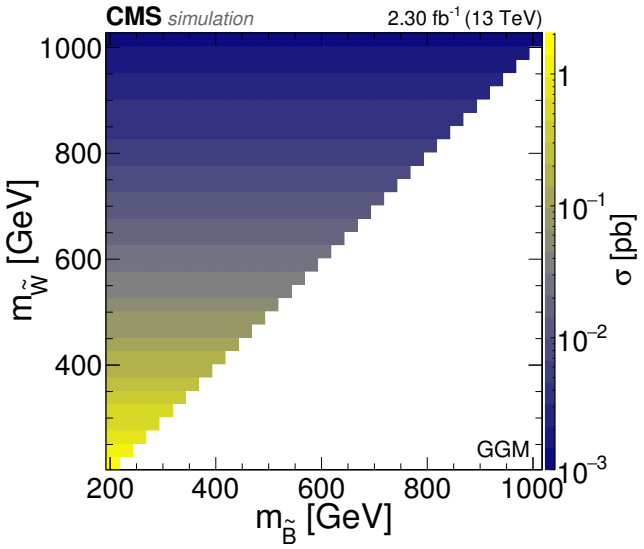

Figure 3.3: Production cross section for the considered GGM model as a function of the bino and wino masses [1].

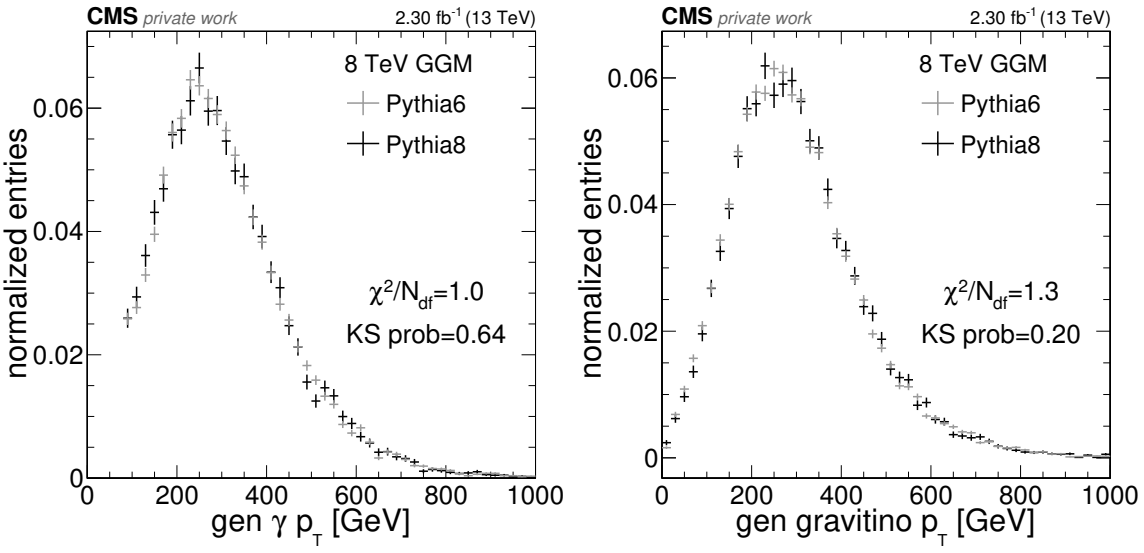

Figure 3.4: Comparison of the generated p_T of the photon (left) and the gravitino (right) for GGM simulation using PYTHIA 6 and PYTHIA 8 at $\sqrt{s} = 8\,\text{TeV}$. The χ^2 per number of degrees of freedom and the Kolmogorov–Smirnov (KS) probabilities shown in the plots indicate good agreement. The masses used in this example are $m_{\tilde{W}} = 640\,\text{GeV}$ and $m_{\tilde{B}} = 630\,\text{GeV}$.

simulation has been found to sometimes produce unphysically high energetic reconstructed jets. This generally also implies large values of E_T^{miss}, artificially increasing the signal acceptance. To counter this effect, the prescription agreed on by the CMS SUSY group is applied for the final interpretations. An event is rejected if a jet with

$|\eta| < 2.5$, $p_T > 20\,\text{GeV}$, and a charged hadron fraction of < 0.1 cannot be matched within $\Delta R < 0.3$ to any generated jet.

In the plots shown in this thesis, three different example signals are shown with the labels corresponding to the following mass points

- GGM: $m_{\tilde{W}} = 640\,\text{GeV}, m_{\tilde{B}} = 630\,\text{GeV}$,
- T5gg: $m_{\tilde{g}} = 1400\,\text{GeV}, m_{\tilde{\chi}_1^0} = 1200\,\text{GeV}$, and
- T5Wg: $m_{\tilde{g}} = 1550\,\text{GeV}, m_{\tilde{\chi}_1^0} = m_{\tilde{\chi}_1^\pm} = 1500\,\text{GeV}$.

The GGM example point corresponds to masses close to the $\sqrt{s} = 8\,\text{TeV}$ exclusion contour. Both, the T5Wg and T5gg points, were not excluded by $\sqrt{s} = 8\,\text{TeV}$ searches [48], but this analysis, as well as other $\sqrt{s} = 13\,\text{TeV}$ searches, are expected to be sensitive in this mass region.

3.4 Event selection

Event selection criteria are developed such that the selection efficiency for possible a signal is as large as possible, while trying to reduce the SM backgrounds. A preselection is made, mainly determined by the trigger requirements. Based on the this, different regions are defined to perform and validate the background prediction and to perform the actual SUSY search.

Preselection

At least one good vertex is required in an event, meaning that the vertex fit is required to have at least four degrees of freedom and that the vertex has a maximal deviation from the nominal interaction point of 24.0 cm in z direction and 2 cm in the x-y plane.

Several data quality filters (E_T^{miss} filters) are used to reject pathological events with unphysical reconstructed particles or E_T^{miss}. Most of them are caused by faulty signals in the detector electronics or beam-halo muons created in beam-gas scattering in the beam pipe. The POG-recommended E_T^{miss} filters [122] are applied, namely

- `Flag_HBHENoiseFilter`
- `Flag_HBHENoiseIsoFilter`
- `Flag_CSCTightHalo2015Filter`
- `Flag_EcalDeadCellTriggerPrimitiveFilter`
- `Flag_goodVertices`
- `Flag_eeBadScFilter` .

Events are selected if they contain at least one identified photon (see Section 3.1) with $p_T > 180\,\text{GeV}$ which is geometrically separated from jets and has been accepted by the trigger. The p_T threshold is motivated by the trigger choice, described below. The explicit separation requirement $\Delta R(\gamma, \text{nearest jet}) > 0.5$ is chosen, because for some MC samples the same restriction is used at generator level. The jets used for the ΔR calculation are not cleaned from other objects in a cone of 0.4 as described in Section 3.1, but here a jet is only removed from the candidate collection if it contains a photon within $\Delta R < 0.1$ and $|\Delta p_T|/p_T < 0.5$. The two-dimensional distribution of both variables can be seen in Fig. 3.5.

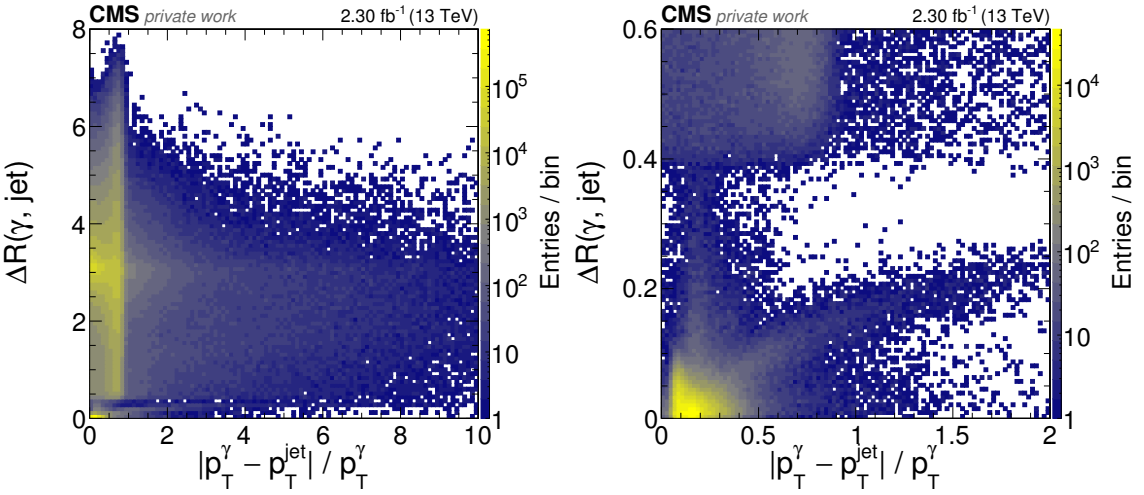

Figure 3.5: Matching of jets and photons. The distance in ΔR is shown vs. the relative transverse momentum deviation. The right plot is a zoomed version.

Figure 3.6 shows the distributions of the leading photon p_T, missing transverse energy, transverse mass, E_T^{miss} significance, H_T, and $\Delta\phi(E_T^{\text{miss}}, \gamma_1)$ after the preselection. For the signal points, some characteristic features can be observed. Both, the photon p_T and E_T^{miss}, increase on average with larger NLSP masses, which also directly influence the M_T distribution. Though it is very broad, the maximal values are roughly located at M_T of the order of the NLSP masses of 630 GeV for GGM, 1200 GeV for T5gg, and 1550 GeV for T5Wg. The signal events mostly exhibit a back-to-back topology of the photon and E_T^{miss} ($|\Delta\phi| \approx \pi$) and the E_T^{miss} significance is large compared to the background, especially multijet and γ+jets. For the GGM signal with electroweak production and a low mass splitting of $\Delta m(\widetilde{W}, \widetilde{B}) = 10\,\text{GeV}$, the hadronic activity is very low. The H_T distribution peaks at $\approx 400\,\text{GeV}$ for the T5gg example point of strong production, because jets are produced at two gluino decay vertices along with the NLSP, at each of which $\Delta m(\widetilde{g}, \widetilde{\chi}_1^0) = 200\,\text{GeV}$ is contributed to the hadronic energy. For the T5Wg point, the jets that are produced are mostly not reconstructed, because of the low mass splitting of $\Delta m(\widetilde{g}, \widetilde{\chi}_1^0/\widetilde{\chi}_1^\pm) = 50\,\text{GeV}$. The 50 GeV available at each $\widetilde{g}$ decay vertex are split between the two produced jets. Additional contributions to H_T may arise from initial state radiation jets, pileup and the underlying event.

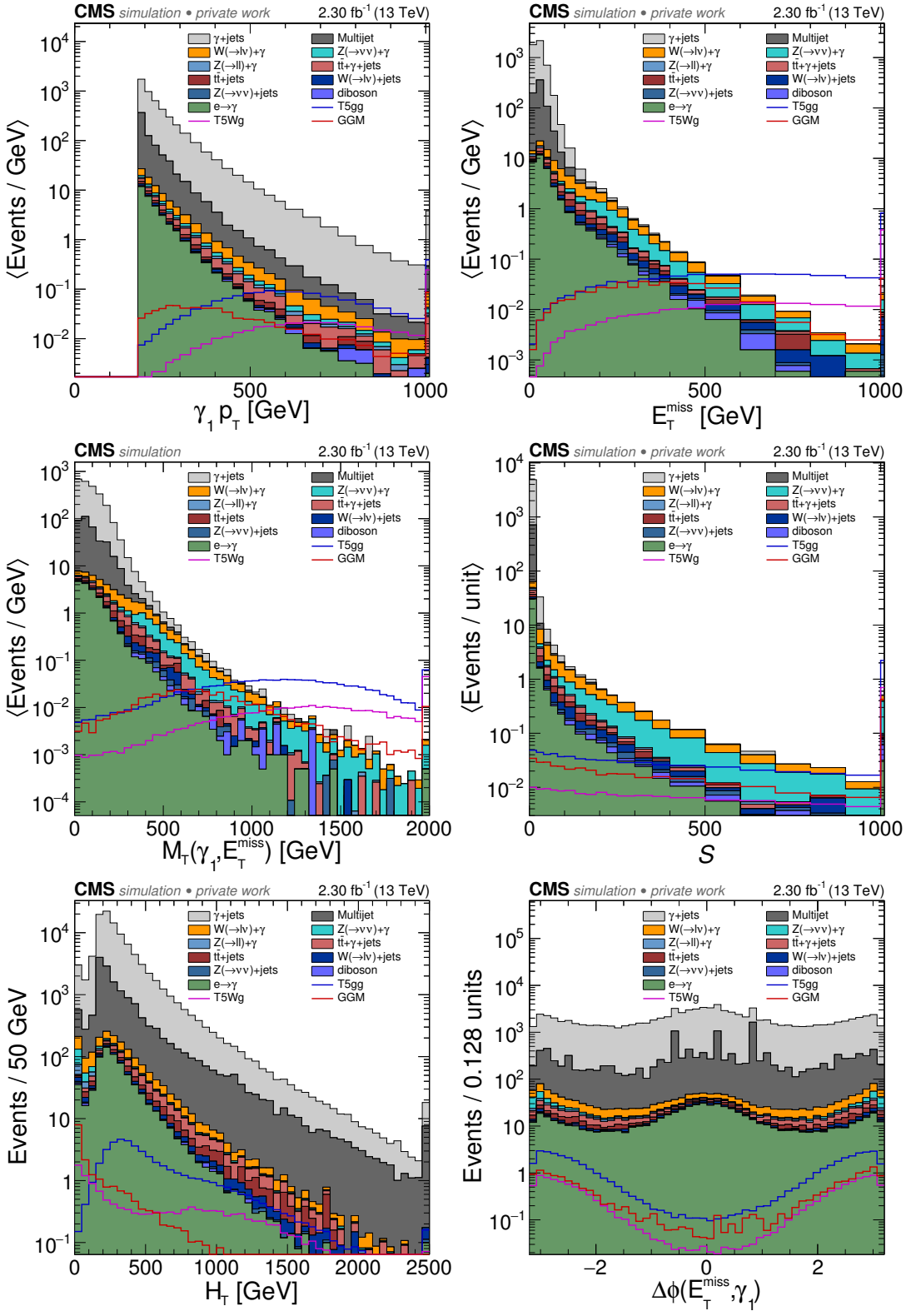

Figure 3.6: Distributions after preselection. Top: Leading photon p_{T} and $E_{\mathrm{T}}^{\mathrm{miss}}$. Middle: Transverse mass and $E_{\mathrm{T}}^{\mathrm{miss}}$ significance. Bottom: Hadronic activity and azimuthal angle between $E_{\mathrm{T}}^{\mathrm{miss}}$ and leading photon. All used samples are taken from MC simulation, except the $\mathrm{e} \rightarrow \gamma$ component, which is determined using the method described in Section 4.2. The overflow is contained in the last bin and the bin contents are divided by the bin widths. Partially published in [1].

Trigger

The events are recorded using a single-photon trigger, `HLT_Photon165_HE10`, requiring a photon reconstructed by the high-level trigger (HLT) with $p_T > 165\,\text{GeV}$ and $H/E < 10\%$. It is seeded by an `OR` combination of the level-1 triggers `L1_SingleEG25`, `L1_SingleEG40`, and `L1_SingleJet200`, i.e. requiring an electromagnetic object with a transverse energy of at least 25 GeV or 40 GeV or a jet with at least 200 GeV at L1 level.

To measure the efficiency of the *signal trigger* `HLT_Photon165_HE10`, events are selected using an independent *base trigger*. The missing transverse energy trigger `HLT_PFMET170` is chosen for this purpose, which has a E_T^{miss} threshold of 170 GeV. The efficiency is measured using the events that pass the base trigger and that contain a photon fulfilling the offline identification criteria described in Section 3.1, which is separated from jets by $\Delta R(\gamma, \text{nearest jet}) > 0.5$ as described in the event selection. Using these events, the fraction of events in which the considered photon has also been accepted by the signal trigger can be determined,

$$\varepsilon = \frac{\#\{\text{signal} \wedge \text{base}\}}{\#\{\text{base}\}}.$$

This is done in bins of the leading photon's offline p_T to see above which threshold the signal trigger reaches its maximal efficiency. Figure 3.7 shows this measurement.

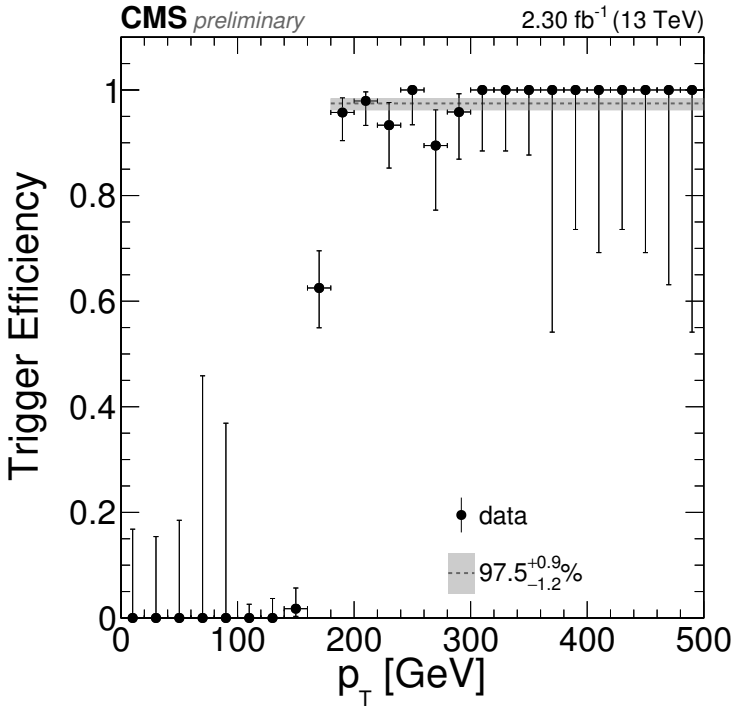

Figure 3.7: The measured trigger efficiency in bins of leading photon p_T. The dashed line indicates the efficiency for the plateau and the value is given in the plot. The uncertainty is illustrated as a gray band. All shown uncertainties correspond to 68% CL Clopper-Pearson intervals. The large statistical uncertainties at low p_T are due to a technical preselection cut [1].

A flat trigger efficiency is observed for $p_{\mathrm{T}}(\gamma) > 180\,\mathrm{GeV}$. Therefore, this p_{T} threshold is used for the event selection described above. The efficiency measured for $p_{\mathrm{T}}(\gamma) > 180\,\mathrm{GeV}$ is

$$\varepsilon = 97.5^{+0.9}_{-1.2}\%,$$

where the uncertainty is calculated from a 68% convidence level (CL) Clopper-Pearson interval [123]. All simulated samples are scaled with this efficiency. The uncertainty is considered as a systematic uncertainty for the backgrounds that are completely determined from simulation.

The photon p_{T} threshold of 180 GeV is a significant increase with respect to the $\sqrt{s} = 8\,\mathrm{TeV}$ offline trigger selection of $p_{\mathrm{T}} > 40\,\mathrm{GeV}$ together with $E_{\mathrm{T}}^{\mathrm{miss}} > 100\,\mathrm{GeV}$. A similar photon+$E_{\mathrm{T}}^{\mathrm{miss}}$ trigger has been considered for this search initially, but has been found to be inefficient for large photon p_{T} due to isolation requirements at HLT level that are not covered by the requirements on the offline isolation, which is computed differently. A different photon+$E_{\mathrm{T}}^{\mathrm{miss}}$ trigger without the isolation requirements is available, but the high thresholds do not allow a precise background estimation as described in Chapter 4, because of the limited size of the dataset used in this search. It is considered a good option for the 2016 dataset, though. The alternative trigger paths that were considered are discussed in Appendix B.

Region definitions

The preselected events are further categorized into a signal region (SR) where the signal contribution is expected to be enhanced and a control region (CR) which is dominated by SM background and possible signal contribution is negligible. The signal region is used to perform the search, while the control region is needed for the estimation of the main backgrounds. A two-dimensional definition is used for the SR, namely

- $\mathcal{S} > 80$,
- $M_{\mathrm{T}} > 300\,\mathrm{GeV}$.

Events with $S_{\mathrm{T}}^{\gamma} < 600\,\mathrm{GeV}$ are excluded from the SR and used as a validation region (VR) for the background prediction, as it is not signal sensitive (see Section 5.1). The CR is defined as a sideband to the SR by

- $\mathcal{S} > 30$,
- $M_{\mathrm{T}} > 100\,\mathrm{GeV}$,
- not in SR.

The region definitions are illustrated in Fig. 3.8.

The $\mathcal{S}$ and M_{T} distributions are shown for signal and background in Fig. 3.9. The CR definition has been chosen to contain enough W/Z(+γ) events to perform the fit described in Section 4.1, while keeping the contribution of (γ+)jets as low as possible. Figure 3.10 also shows the distributions of the total background (top) and two signal

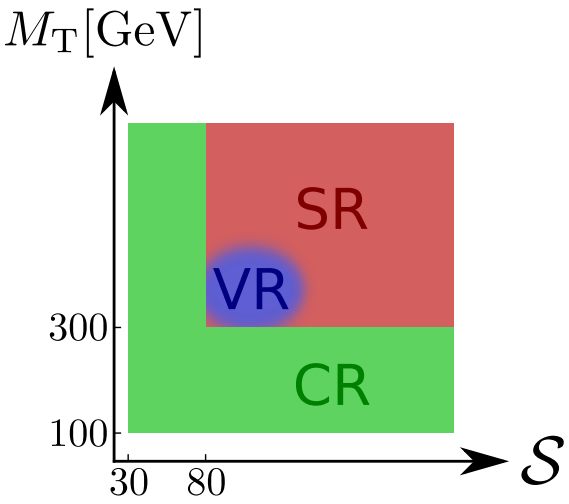

Figure 3.8: Sketch of the control (CR) and signal region (SR) definitions. The validation region (VR) is not defined in the $\mathcal{S}$-M_T plane, but embedded in the SR with the additional condition $S_T^\gamma < 600\,\text{GeV}$. This corresponds approximately to the bottom-left corner of the SR, which is therefore illustrated as a blurred region [1].

points (bottom) in the $\mathcal{S}$-M_T plane. The influence of possible signal contribution to the CR (signal contamination) has been found to be negligible for most scenarios, which is further discussed in Chapter 5, where also the consideration of the remaining influence is described.

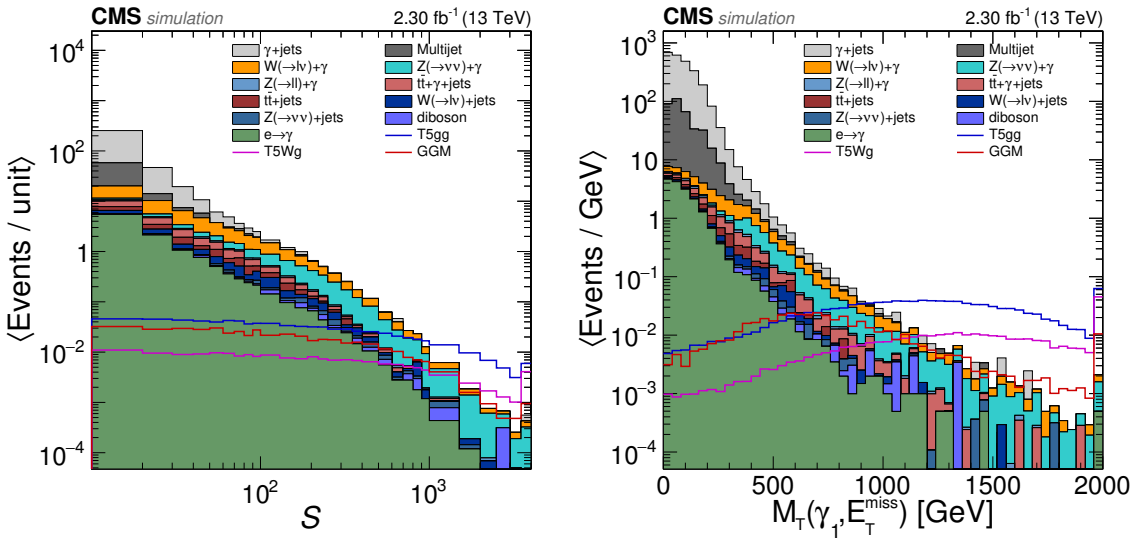

Figure 3.9: The $\mathcal{S}$ and M_T distributions after the preselection. All used samples are taken from MC simulation, except the e $\rightarrow \gamma$ component, which is determined using the method described in Section 4.2. The overflow is contained in the last bin shown and the bin contents are divided by the bin widths [1].

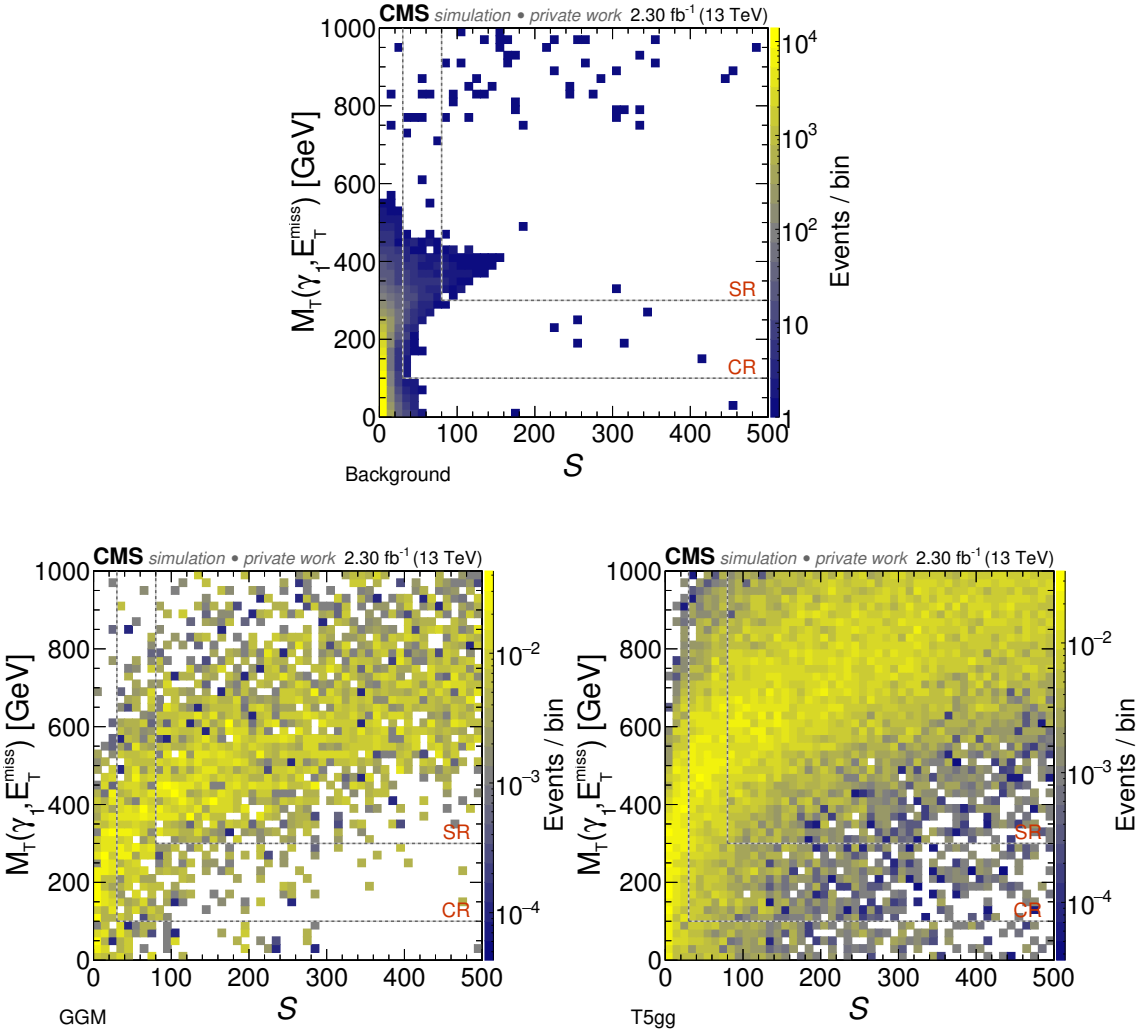

Figure 3.10: Top: Distribution of the total background in the $\mathcal{S}$-M_{T} plane. All used samples are taken from MC simulation, except the e $\rightarrow \gamma$ component, which is determined using the method described in Section 4.2. Bottom: Distribution of the example signal points for GGM (left) and T5gg (right). The dashed lines indicate the SR and CR borders.

4 Background estimation

Contents

In this analysis, a cut-and-count experiment is performed, i.e. the number of observed events in the signal region is compared to the number expected from known SM physics. To be sensitive to the presence of any BSM physics, resulting in an excess of events, the SM background needs to be predicted as accurately as possible.

Backgrounds passing the analysis selections arise from SM processes for which photons and $E_{\mathrm{T}}^{\mathrm{miss}}$ are reconstructed. The reconstructed photons can either be real photons or misidentified objects, i.e. electrons or jets. Missing transverse energy can arise from neutrino production or can be caused by the finite detector resolution (instrumental $E_{\mathrm{T}}^{\mathrm{miss}}$).

The dominant SM backgrounds for this search are the production of W($\rightarrow \ell\,\nu$) and Z($\rightarrow \nu\nu$) in association with a photon, in the following denoted V+γ, due to the neutrinos in the final state which result in missing transverse energy.

A further background with a large contribution especially in the control region selection comes from multijet events, where either a jet is misreconstructed as a photon (QCD multijet) or a real photon is radiated (γ+jets), the latter having the larger contribution. Although such events are balanced and all final state particles can be reconstructed, missing transverse energy arises from the limited detector resolution, especially of the HCAL. This background is important because of its large cross section. The V(+γ) and (γ+)jets backgrounds are estimated starting from simulated samples. These samples are then scaled by correction factors which are derived simultaneously using a template fit to the data in the control region, described in detail in Section 4.1.

Further smaller, but non-negligible backgrounds are events containing electrons that are misidentified as photons (e $\rightarrow \gamma$) and $\mathrm{t\bar{t}}$ events with photon radiation. For the estimation of the e $\rightarrow \gamma$ background a common data driven approach is used, which is explained in Section 4.2. The $\mathrm{t\bar{t}}$ events with photon radiation ($\mathrm{t\bar{t}} + \gamma$), as well as the remaining contributions of $\mathrm{t\bar{t}}$ and diboson production (WW, WZ, ZZ) due to jets misreconstructed as photons, are determined completely from simulation, as explained in Section 3.3, and not further described in the following.

4.1 Main backgrounds: W/Z(+γ) and (γ+)jets

For the dominant backgrounds, scale factors are derived in the signal depleted control region, defined in Section 3.4, using a template fit or MC normalization, i.e. template distributions for different backgrounds are taken from simulation and the normalization of the single templates is scaled to match the distribution observed in data. For this purpose, the simulated background samples are grouped into

- (γ+)jets = {multijet, γ+jets},
- V(+γ) = {W(+γ), Z(+γ)},
- fixed = {$t\bar{t}$(+γ), e $\rightarrow \gamma$, diboson} .

The normalization of each of the first two categories is determined by the fit, while the fixed backgrounds cannot vary. Of the fixed backgrounds, the e $\rightarrow \gamma$ part is determined using the data-driven method described in Section 4.2. To minimize the influence of $t\bar{t}$(+γ), which is the main part of the fixed backgrounds, the fit is performed in the CR with the additional requirement that no jet in an event is b-tagged using the tight working point.

To be able to reliably determine both normalizations, the variable used for the template distributions has to separate the two background categories. The variable used for the fit is $|\Delta\phi|(E_{\mathrm{T}}^{\mathrm{miss}}, \mathrm{jet}_1)$, because in this distribution the main backgrounds (γ+)jets and V(+γ) have different shapes as can be seen in Fig. 4.1, which already shows the post-fit distribution. For (γ+)jets, the missing transverse energy tends to be aligned with a jet, because of jet energy mismeasurements, which in most cases is the leading jet (jet_1). Compared to the resulting concentration of $|\Delta\phi|(E_{\mathrm{T}}^{\mathrm{miss}}, \mathrm{jet}_1)$ at low values, the V(+γ) events show a uniform distribution. For events not containing a jet, $|\Delta\phi|(E_{\mathrm{T}}^{\mathrm{miss}}, \mathrm{jet}_1)$ is not defined. Nevertheless, those events are used and counted in an extra bin, displayed as the overflow bin "$|\Delta\phi| > \pi$" in the plots.

An extended maximum likelihood (EML) approach is chosen for the template fit [124]. The simple maximum likelihood technique, used in the predecessor analysis in form of a χ^2-fit, assumes normalized probability density functions. In the case of fitting two template distributions to data, only a single fraction parameter f is varied to maximize the likelihood

$$\mathcal{L}(f) = \prod_{i=1}^{n} \left(f P_1(x_i) + (1-f) P_2(x_i) \right) ,$$

where the index i enumerates all n data points and $P_j(x_i)$ denotes the probability of observing the value x_i given the probability density components P_j, i.e. the templates. While this is suited for determining the relative composition of a data sample, it assumes that the normalization of the data and the model agree exactly. In the case where one is interested in the absolute contribution of each template component, the number of observed events has to be treated as a random number, though. In the EML approach the total number of events is treated as a free Poisson-distributed parameter

with mean ν, leading to the extended likelihood

$$\begin{aligned}\mathcal{L}_E(f,\nu) &= \frac{\mathrm{e}^{-\nu}\nu^n}{n!}\mathcal{L}(f) \\ &= \frac{\mathrm{e}^{-\nu}}{n!}\prod_{i=1}^{n}\left(\underbrace{\nu f}_{=:\nu_1}P_1(x_i) + \underbrace{\nu(1-f)}_{=:\nu_2}P_2(x_i)\right) \\ &\equiv \frac{\mathrm{e}^{-(\nu_1+\nu_2)}}{n!}\prod_{i=1}^{n}(\nu_1 P_1(x_i) + \nu_2 P_2(x_i)) = \mathcal{L}_E(\nu_1,\nu_2)\,.\end{aligned}$$

In the maximization of the extended likelihood, the two independent parameters (f, ν) are varied. Equivalently, this can be expressed as a fit of two normalizations (ν_1, ν_2), for which $\nu_1 + \nu_2 = \nu$ applies.

A binned extended maximum likelihood fit is performed using the RooFit package [125]. The resulting normalizations N_i^{fit} ($i \in \{(\gamma+)\text{jets}, \text{V}(+\gamma)\}$) are used to determine the MC scale factors

$$\text{SF}_i = N_i^{\text{fit}}/N_i^{\text{init}}$$

with the initial number N_i^{init} of events contained in template i and the number N_i^{fit} determined by the fit. The results of the fit are

$$\text{SF}_{(\gamma+)\text{jets}} = 1.46 \pm 0.13, \tag{4.1a}$$

$$\text{SF}_{\text{V}(+\gamma)} = 0.69 \pm 0.17, \tag{4.1b}$$

which are shown in the post-fit distribution in Fig. 4.1. The uncertainties of the fit are of statistical origin and the corresponding correlation is $\rho = -0.64$. In contrast to that, the usage of a simple maximum likelihood fit would imply a correlation of exactly -100%. For the LO (γ+)jets template a scale factor larger than unity is expected owing to missing higher order corrections in α_s that would increase the cross section. The V($+\gamma$) template is already corrected with QCD NNLO k-factors. Additional electroweak corrections are expected to decrease the cross section, which explains a scale factor lower than unity. The total post-fit distribution shows a good agreement with the data, also reflected in the pulls shown in the lower part of the same plot.

The obtained scale factors are applied to the corresponding simulated samples to predict the (γ+)jets and V($+\gamma$) backgrounds in the signal region.

All main uncertainties of the simulation that would express in a normalization uncertainty are eliminated by this MC normalization method. The remaining uncertainties are the statistical uncertainties of the fit result, which enter as systematic uncertainties in the following. For the final interpretation, the anti-correlation of these is taken into account.

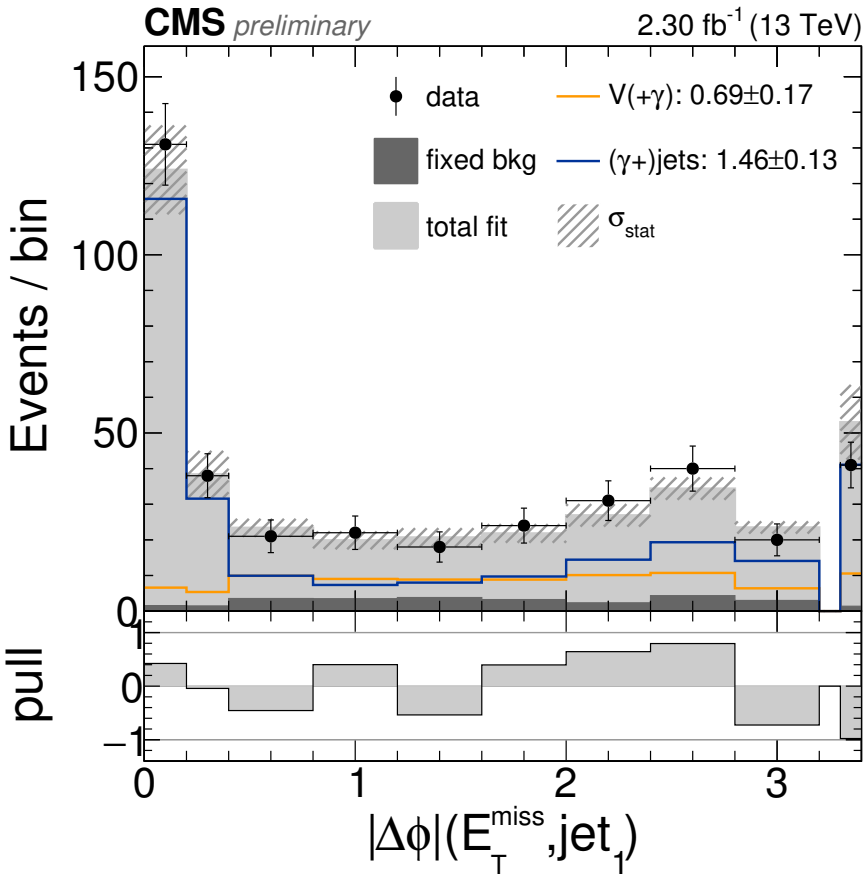

Figure 4.1: Template fit result: The post-fit distributions for (γ+)jets and V($+\gamma$) together with the total fit distribution stacked onto the fixed backgrounds. Events containing zero jets are counted in the last shown bin. The values in the legend are the resulting scale factors [1].

Stability of the fit method

To check that possible shape uncertainties do not have an influence beyond the quoted uncertainties and to verify the stability of the fit, different systematic variations are performed:

- The binning is varied, using approximately half and twice the number of bins.
- Different template variables are used, e.g. the angle between $E_{\mathrm{T}}^{\mathrm{miss}}$ and the nearest jet and between $E_{\mathrm{T}}^{\mathrm{miss}}$ and the leading photon.
- The control region definition is altered, shifting the lower or upper bounds. Also one-dimensional definitions are used, the b-tag veto is removed, and different b-tagging working points are checked.
- The JES is varied within its uncertainties, which can change which jet is selected.
- The JES is varied within its uncertainties and the differences are propagated to $E_{\mathrm{T}}^{\mathrm{miss}}$.

The fit results obtained using a subset of these variations are illustrated in Fig. 4.2. Selection strings used in this figure and following ones are to be read like this:

`Xx`	means	$X > x$,
`Xlx`	means	$X < x$,
`v`	means	"or".

The additions `0bT`, `0bM`, and `0bL` indicate a 0-b-tag requirement for tight, medium, and loose working points. The deviations from the nominal result are largely within the uncertainty margin and the observed fluctuations are expected when considering 1σ errors. Since both scale factors are correlated, the results of the fit variations are also shown in two dimenions in Fig. 4.3. It should be noted that the results are strongly correlated among each other. For example, fits using the same selection but different distributions are expected to be shifted roughly in the same way. Based on these studies, the uncertainties given in Eq. (4.1) are assumed to cover the systematic effects listed above and are taken as the total uncertainties for V(+γ) and (γ+)jets.

The influence of the renormalization and factorization scale, and variations of the parton density functions (PDFs) are also found to be negligible for the V(+γ) SF. For the (γ+)jets SF, the variation reached maximum deviations of -0.18 and $+0.19$ for changes of the scales by factors of 0.5 and 2. Therefore, an additional systematic uncertainty of 13% is assigned to $\mathrm{SF}_{(\gamma+\mathrm{jets})}$.

A possible contribution of signal in the fit region is not expected to influence the fit, as long as it is not too large. Figure 4.4 shows the pre-fit distributions of the templates together with data and the example GGM signal point. The bin with the highest possible signal contribution would still have a sub-percent share of the total data. A possible contamination of signal in the CR can become important for low NLSP masses, because the M_{T} criterion for the SR definition might not be met. The treatment of the signal contamination in mass regions in which it is no longer negligible is described in the context of the final interpretation in Section 5.3.

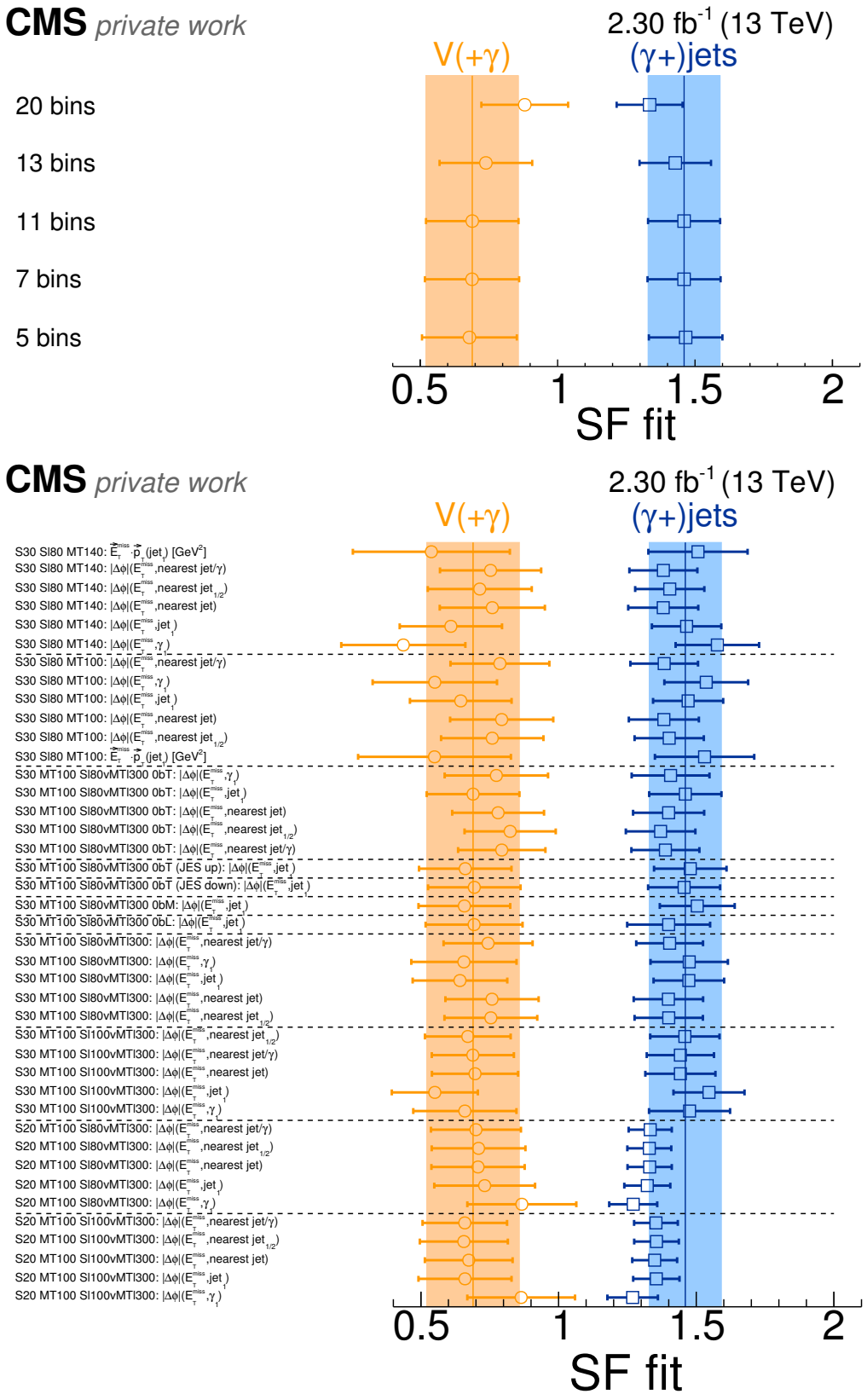

Figure 4.2: Top: Fit results using different numbers of bins. Bottom: Fit results for different selections and variables, grouped by selection. The shown lines and error bands correspond to the nominal fit result given in Eq. (4.1).

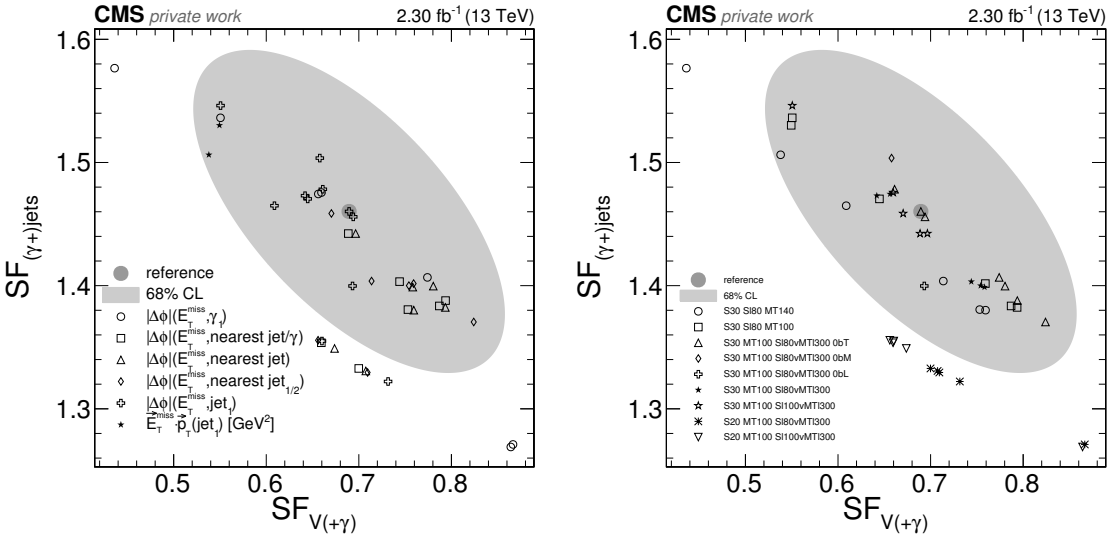

Figure 4.3: The same fit results as shown in Fig. 4.2 (bottom) in two dimensions. The nominal value is shown with its 1σ uncertainty ellipse. The same points are shown on both sides. Left: The same marker indicates one template variable. Right: The same marker indicates one selection used for the fits.

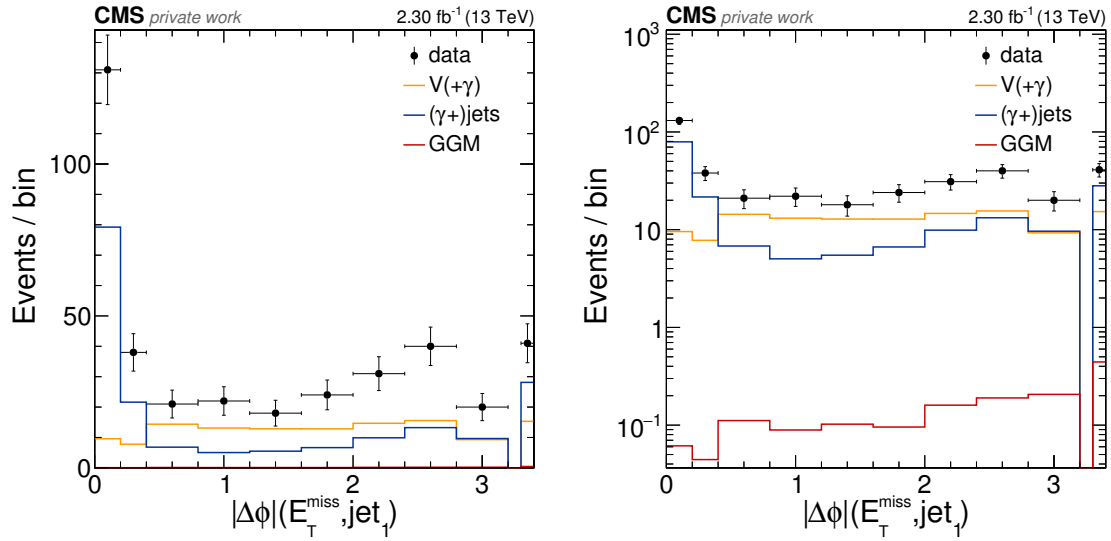

Figure 4.4: The pre-fit distributions of both templates shown with data and the GGM signal point using linear (left) and logarithmic (right) scales. A possible presence of signal is not expected to influence the fit result.

Robustness with respect to higher order corrections

To estimate possible effects of higher order corrections on the method, the whole prediction is repeated without applying the NNLO k-factors for V($+\gamma$) described in Section 3.3. This affects the templates in the CR and thus the fit results, as well as the V($+\gamma$) shape in the SR due to the p_{T}-dependent corrections. Of the higher order effects, only the part influencing shapes can alter the results, because normalization variations are compensated by the fit.

Of the nominal fit result (4.1), only the V($+\gamma$) is influenced within the uncertainty while the ($\gamma+$)jets scale factor is completely stable. This implies that the ($\gamma+$)jets prediction in the SR is not altered. The changed V($+\gamma$) yields in the SR are compared to the original ones for all SR bins, defined in Section 5.1, showing a relative change of $1-4\%$ which is not significant compared to the statistical uncertainty.

Since the higher order corrections may affect the photon p_{T} and therefore the selection efficiencies of the CR and SR, the ratio $\varepsilon_{\mathrm{CR}}/\varepsilon_{\mathrm{SR}}$ of those efficiencies is compared with and without the corrections. Without applying the NNLO corrections the variation is in the sub-percent range.

The same has been tested with the renormalization and factorization scales increased and decreased by a factor of two, yielding variations of at most 4% for the V($+\gamma$) scale factor. The scale variations change the nominal value for ($\gamma+$)jets in the order of $1-2\%$. PDF variations are found to have the strongest influence on $\varepsilon_{\mathrm{CR}}/\varepsilon_{\mathrm{SR}}$ for ($\gamma+$)jets. The deviations are below 5%.

These effects are small with respect to the fit uncertainties and therefore considered to be covered already.

The tests have also been performed separately for each SR bin, i.e. $\varepsilon_{\mathrm{CR}}/\varepsilon_{\mathrm{SR}_i}$ has been calculated. The observed fluctuations partially reached multiples of 10%, but were found to not be significant with respect to the statistical errors of the values.

Test of the method on simulation

The MC normalization method can be tested on simulation. For this purpose, toy data is generated using MC simulation, where single components of the background can be scaled by desired factors. The fit can be performed using the generated data and it is checked that the fitted scale factors (SF_i) reflect the true scale factors (f_i). The fitted scale factors can be applied in the signal region to check if the obtained prediction describes the toy data.

The toy data in the CR is generated with the following procedure.

1. Add up all simulated backgrounds to a histogram H_{true}, possibly scaling the components with factors $f_{\mathrm{V}(+\gamma)}$ and $f_{(\gamma+)\mathrm{jets}}$.

2. For each bin i of H_{true} with the bin content t_i, draw a random number r_i from a Poisson distribution with a mean equal to t_i.

3. Set the content of bin i of the toy data histogram H_{toy} to r_i with an error of $\sqrt{r_i}$.

Now, the fit is performed using this toy data. An example fit with the backgrounds scaled with $f_{\mathrm{V}(+\gamma)} = 0.5$, $f_{(\gamma+\mathrm{jets})} = 1.5$ yields $\mathrm{SF}_{\mathrm{V}(+\gamma)} = 0.61 \pm 0.18$ and $\mathrm{SF}_{(\gamma+\mathrm{jets})} = 1.66 \pm 0.14$, reasonably reproducing the input within the expected statistical fluctuation.

The determined scale factors are applied in the SR to obtain the prediction. Here, also the part with $S_{\mathrm{T}}^{\gamma} < 600\,\mathrm{GeV}$, normally used as the VR, is included as a fourth bin, because the background prediction has to be valid in this region, too. Again, toy data is generated as described for the CR and compared to the prediction, as illustrated for the chosen example in Fig. 4.5. The systematic uncertainty shown stems from the errors of the fit result. Reasonable agreement can be observed. To further quantify this, the χ^2/N_{df} is calculated, which is 1.2 in the shown case.

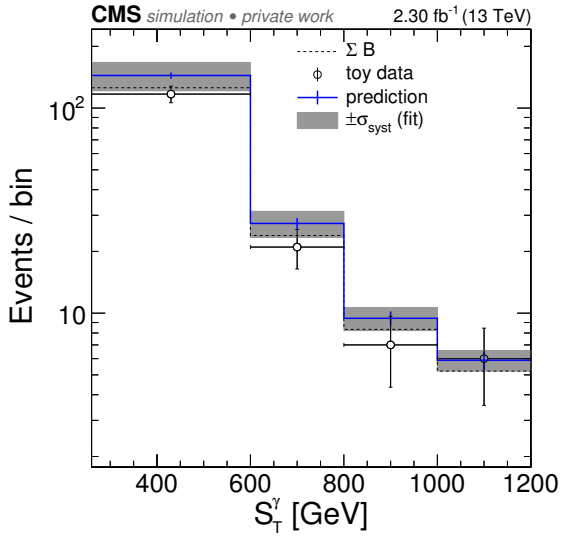

Figure 4.5: Closure test of the extrapolation of the fitted scale factors to the signal region for $f_{\mathrm{V}(+\gamma)} = 0.5$, $f_{(\gamma+\mathrm{jets})} = 1.5$. The dashed line is the sum of all background processes scaled with the f_i, the open circles are the toy data generated from this true distribution. The prediction obtained from the fitted SF_i is shown in blue and the systematic error is originating from the fit errors.

One can repeat this procedure using different random seeds. In this case, it is repeated for different choices of f_i to also ensure that the method does not show a bias for specific scalings. One factor is fixed to unity ($f_i = 1$), while the other one is scanned ($f_j \in [0.5, 2.0]$). Figure 4.6 shows the scans for both $f_{\mathrm{V}(+\gamma)}$ and $f_{(\gamma+\mathrm{jets})}$. The lines show the input scale values f_i and the markers represent the fitted values SF_i with their uncertainties, which show the expected statistical fluctuation around the true value. The χ^2/N_{df} values calculated in the SR are of the order of 1, indicating a good description of the signal region distribution. Furthermore, the total prediction in the SR is compared to the true value in Fig. 4.7, also showing good agreement.

The whole procedure can be repeated taking into account possible presence of signal to check the performance of the method in the case of signal contamination. For this purpose, toy data is generated as described above, but also adding up the signal in addition to the background samples. In this case, the example GGM point is used. The fit is repeated, yielding $\mathrm{SF}_{\mathrm{V}(+\gamma)} = 0.62 \pm 0.18$ and $\mathrm{SF}_{(\gamma+\mathrm{jets})} = 1.66 \pm 0.14$ for $f_{\mathrm{V}(+\gamma)} = 0.5$

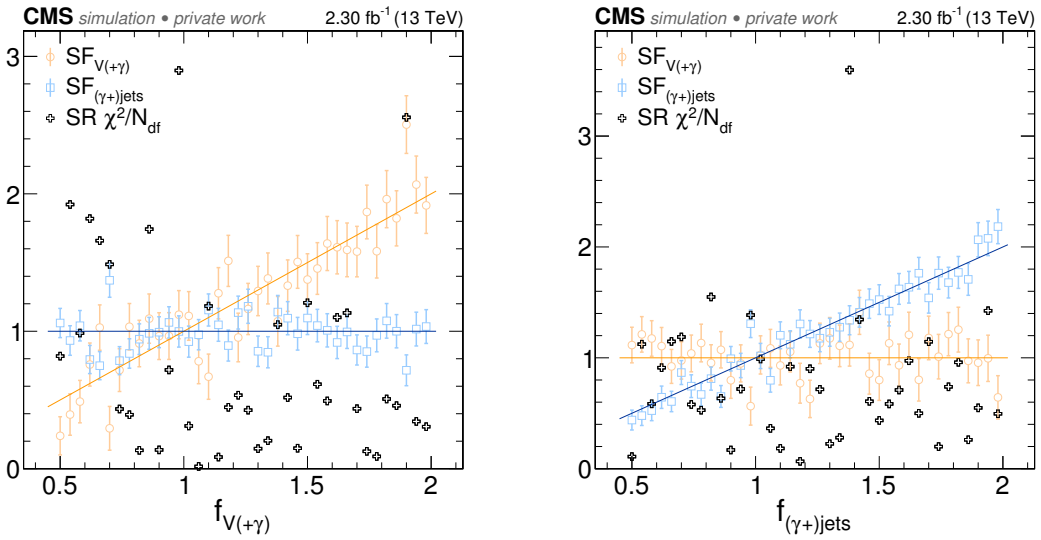

Figure 4.6: Closure test of the fit procedure vs. f_i. The lines show the input values f_i and the markers represent the fitted SF_i with their errors. The χ^2/N_{df} values are calculated for the SR distributions.

and $f_{(\gamma+)\mathrm{jets}} = 1.5$. The extrapolation to the signal region is shown in Fig. 4.8, showing a good agreement with the true sum of backgrounds, while maintaining signal sensitivity. Since the toy data is sampled from the distribution containing signal, a disagreement of the prediction in the SR is desired and can be observed. This disagreement is also reflected in the χ^2/N_{df} of 2.6.

Figure 4.9 shows these tests for different f_i. The fitted scale factors SF_i still reproduce the input values in the case of signal presence. The χ^2/N_{df} are significantly increased with respect to the background-only closure test, indicating the preservation of signal sensitivity. In Fig. 4.10 one can see that the total background yield in the SR is still described well.

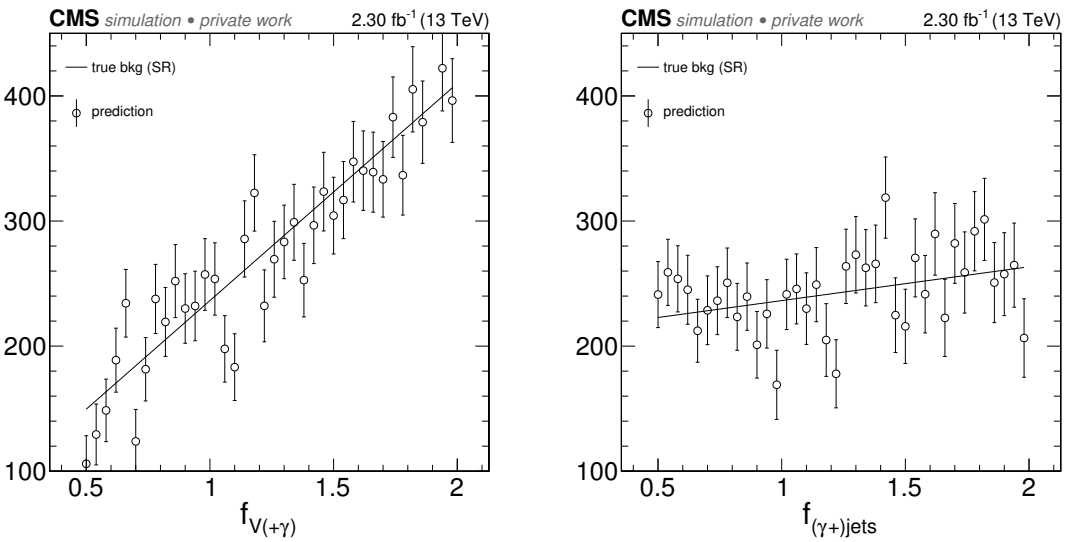

Figure 4.7: Closure test of the total SR prediction vs. f_i. The lines show the expectation, the prediction with its systematic uncertainties is shown as markers.

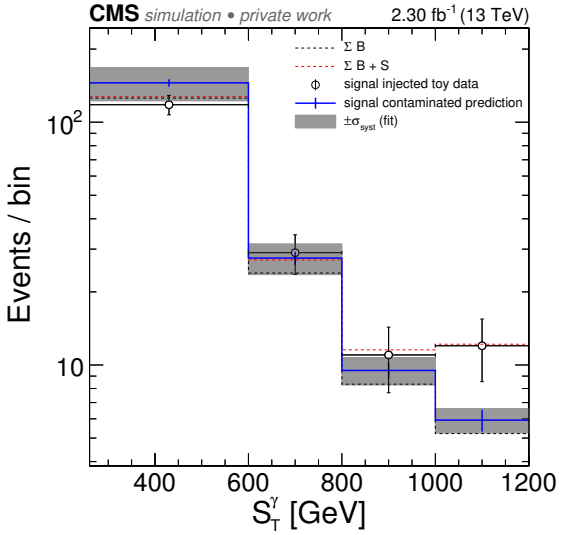

Figure 4.8: Closure test of the extrapolation of the fitted scale factors to the signal region for $f_{\mathrm{V}(+\gamma)} = 0.5$, $f_{(\gamma+)\mathrm{jets}} = 1.5$ in the presence of signal in both the SR and CR. The black dashed line is the sum of all background processes scaled with the f_i and the red dashed line also includes the signal. The open circles are the toy data generated from the true distribution containing the signal. The prediction obtained from the SF_i is shown in blue and the systematic error is originating from the fit errors.

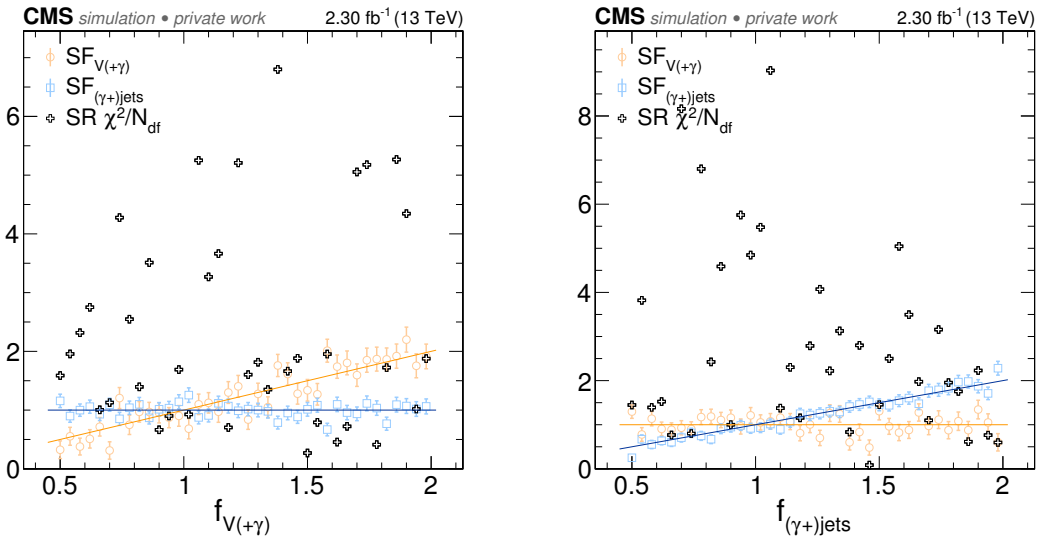

Figure 4.9: Closure test of the fit procedure in the presence of signal in both, the CR and SR, vs. f_i. The lines show the input values f_i and the markers represent the fitted SF_i with their errors. The χ^2/N_{df} values are calculated for the SR distributions including the signal component.

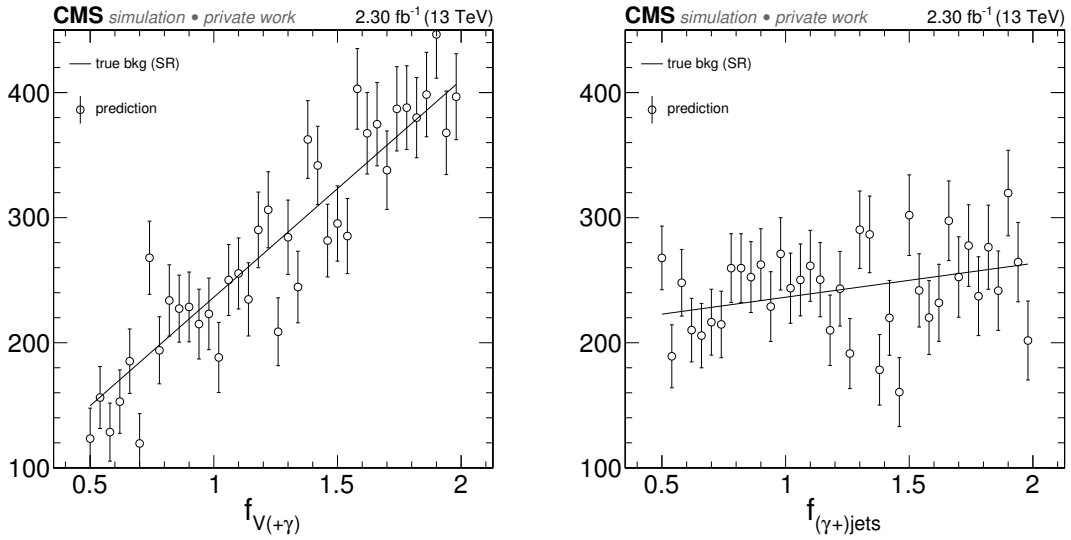

Figure 4.10: Closure test of the total SR prediction in the presence of signal vs. f_i. The lines show the background expectation, the prediction with its systematic uncertainties is shown as markers.

4.2 Background from electrons misidentified as photons

To estimate the background contribution from electrons misidentified as photons, a data-driven tag-and-probe approach is used. The fraction of real electrons that are reconstructed as photons, i.e. that do not have a pixel seed, is determined in data, which is used together with the number of reconstructed electrons to infer the $e \to \gamma$ background. The values have been determined in the context of a separate Master thesis [126], where the details of this procedure are described. The results are also documented in a corresponding CMS analysis note [127].

The tag object is a well reconstructed electron, defined like a photon (cf. Section 3.1) but requiring a pixel seed (γ_{pix}). The probe is an object fulfilling the photon identification criteria, but which is not checked for a pixel seed. To get a large fraction of real electrons in the probe sample, $Z \to ee$ events are selected by requiring an invariant mass of the tag and probe objects between 60 GeV and 120 GeV. After the subtraction of non-Z backgrounds, the number of events in which the probe object does pass the pixel seed veto is used to determine the misidentification rate f. It is determined separately for data and simulation as

$$f_{\text{data}} = 1.94\%,$$
$$f_{\text{MC}} = 1.08\%.$$

An uncertainty of 30% is assigned to these values, which is estimated based on the variations observed as a function of the photon p_{T} and η [126, 127].

To determine the $e \to \gamma$ background, the whole event selection is repeated, but instead of selecting photons, γ_{pix} are used. The resulting distribution is finally scaled by the transfer factor

$$R = \frac{f}{1-f},$$

which takes into account the fact that not all real electrons are counted but only the reconstructed ones, i.e. γ_{pix}. This procedure is tested using simulated $t\bar{t}$, WW, WZ, and ZZ events in the preselection. Figure 4.11 shows the closure test for the photon p_{T}, $E_{\text{T}}^{\text{miss}}$ and $\mathcal{S}$ distributions. The prediction using the described method is compared to the events, in which the reconstructed photon can be matched to a generated electron within $\Delta R < 0.1$ and a relative p_{T} deviation of less than 0.5. Good agreement is observed between the predicted and generator-matched distributions within the statistical precision.

To avoid double counting of $e \to \gamma$ events, all events in simulated samples in which the reconstructed leading photon can be matched to a generated electron ($\Delta R < 0.1$ and a relative p_{T} deviation of < 0.5) are rejected. The remaining diboson and $t\bar{t}$ events may still pass the selection criteria due to jets misidentified as photons. Since the contribution is very small, they are completely determined from simulation, as mentioned above.

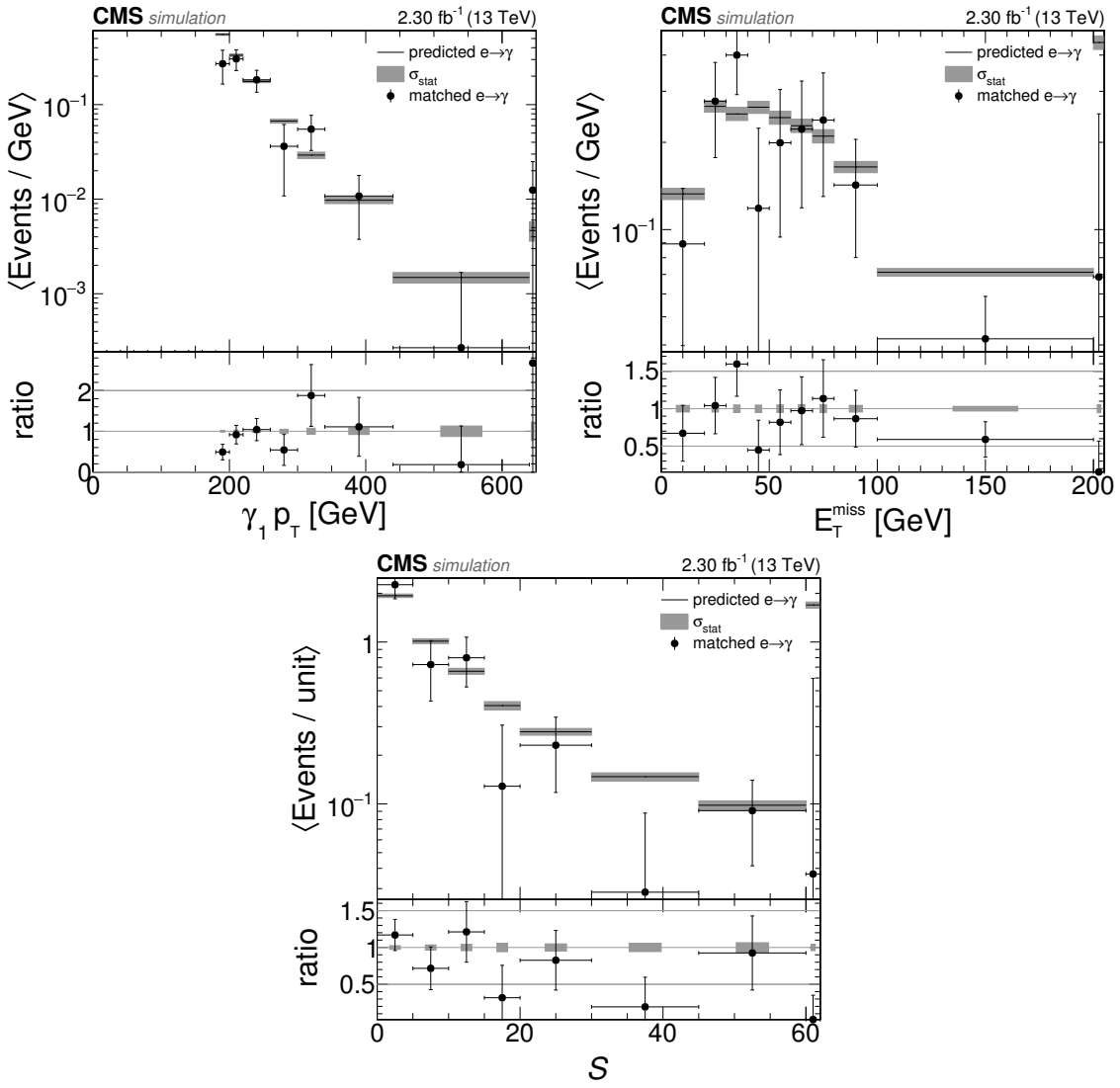

Figure 4.11: Closure tests for the electron misidentification background estimation using simulated $t\bar{t}$, WW, WZ and ZZ events. Only statistical uncertainties are shown. The overflow is contained in the last bin and the bin contents are divided by the bin widths [1].

4.3 Systematic uncertainties

The relative systematic uncertainties are listed in Table 4.1. For the main backgrounds, V(+γ) and (γ+)jets, the fit uncertainties are considered with the corresponding correlation. The influence of the renormalization and factorization scales on the (γ+)jets background is considered separately. The e $\rightarrow \gamma$ uncertainty has been discussed in Section 4.2. For the other less important backgrounds that are taken from simulation, sources of systematic uncertainty are cross section, PDF and scale uncertainties. For $t\bar{t}$(+γ), 30% are assumed, covering the uncertainty of the latest CMS measurement [128]. Diboson cross section measurements for 13 TeV [129–131] yield uncertainties between 9% and 13%. Here, an uncertainty of 20% is assigned to account for the fact that only a special phase space is considered. For the backgrounds and signals that are taken from simulation, the uncertainties of the trigger efficiency (1%) and the luminosity (2.3%) are considered. The ratio of the photon identification efficiency in data and simulation has been studied by the e/gamma POG and found to be consistent with unity. An uncertainty of 1% is derived from these studies. The uncertainty arising from limited sizes of generated MC samples varies for the different bins. Approximate ranges are given in the table for the signal region bins.

Table 4.1: Systematic uncertainties of the individual backgrounds. The uncertainties are relative to the respective backgrounds [1].

	V(+γ)	(γ+)jets	e $\rightarrow \gamma$	$t\bar{t}$(+γ)	Diboson	Signal
Fit uncert. of statistical origin	25%	9%	-	-	-	-
Scale uncert. influence on fit	-	13%	-	-	-	-
Tag-and-Probe fit	-	-	30%	-	-	-
MC statistical precision	$1-3\%$	$21-27\%$	-	$14-25\%$	$47-66\%$	$2-10\%$
Cross section, PDF, scale	-	-	-	30%	20%	-
Luminosity	-	-	-	2.3%	2.3%	2.3%
Trigger efficiency	-	-	-	1%	1%	1%
Photon identification	-	-	-	1%	1%	1%

Since the V(+γ) background is the largest one in the signal region, its uncertainty has the largest contribution to the total systematic uncertainty. This can also be explicitly seen in the results presented in Chapter 5.

For the statistical interpretation the anti-correlation of the uncertainties of V(+γ) and (γ+)jets (cf. Section 4.1) have to be considered, as described in Section 5.3. The luminosity, trigger efficiency, and photon identification uncertainties are treated as fully correlated among all bins and backgrounds.

Theoretical uncertainties affecting the signal cross sections, such as variations of renormalization and factorization scales, and PDF uncertainties are considered separately from the experimental uncertainties listed above and the shifted results are explicitly shown in the interpretations presented in Section 5.3. A possible influence of the theory uncertainties on the signal acceptance, which would be considered an experimental uncertainty, has been found to be negligible compared to the statistical uncertainty of the signal samples.

4.4 Validation of the background prediction

To verify that the total background prediction describes the data in different distributions, the total estimate is compared to the data in the CR. This is done for the CR region with the requirement of 0 b-tags, i.e. the region where the fit is performed. These comparisons are shown in Fig. 4.12 for the leading photon p_{T}, $E_{\mathrm{T}}^{\mathrm{miss}}$, $\mathcal{S}$, M_{T}, S_{T}^{γ}, and H_{T}. Additionally, Figures 4.13 and 4.14 show comparisons for the inclusive CR, i.e. without a requirement concerning b-tags, also showing $|\Delta\phi|$ between the photon and $E_{\mathrm{T}}^{\mathrm{miss}}$, the numbers N_{jets} and N_{γ} of jets and photons, and the shower width $\sigma_{i\eta i\eta}$ of the leading photon. An overall good agreement is observed, especially for the observables used for the event selection in this search. Since the main backgrounds are determined with the fit in the CR, the overall normalization in these distributions agrees almost perfectly. The N_{γ} distribution shows that the majority of the SM events does not contain more than one photon. Consequently, the normalization can be compared easily in the one-photon bin. The description of the shower width is the least precise one and it shows small deviations, but the exact modeling of the shower in the ECAL is very complicated and the resulting agreement can be considered reasonable.

Additionally, the V($+\gamma$) scale factor determined in the fit can be further validated by checking a W enriched region. This is the most important scale factor, since the V($+\gamma$) background dominates in the SR. For this purpose, exactly one lepton is required in the CR, considering only electrons and muons, as described in Section 3.1. Figure 4.15 shows that good agreement is achieved for the $E_{\mathrm{T}}^{\mathrm{miss}}$ and $\mathcal{S}$ distributions.

The VR, which is embedded in the signal region with the requirement $S_{\mathrm{T}}^{\gamma} < 600\,\mathrm{GeV}$, can be used to verify the background prediction outside of the CR. The validation is shown in Fig. 4.16, again for the p_{T}, $E_{\mathrm{T}}^{\mathrm{miss}}$, $\mathcal{S}$, M_{T}, S_{T}^{γ}, and H_{T} distributions, and reasonable agreement is observed, showing that the extrapolation of the scale factors derived in the CR still provides a good description of the data.

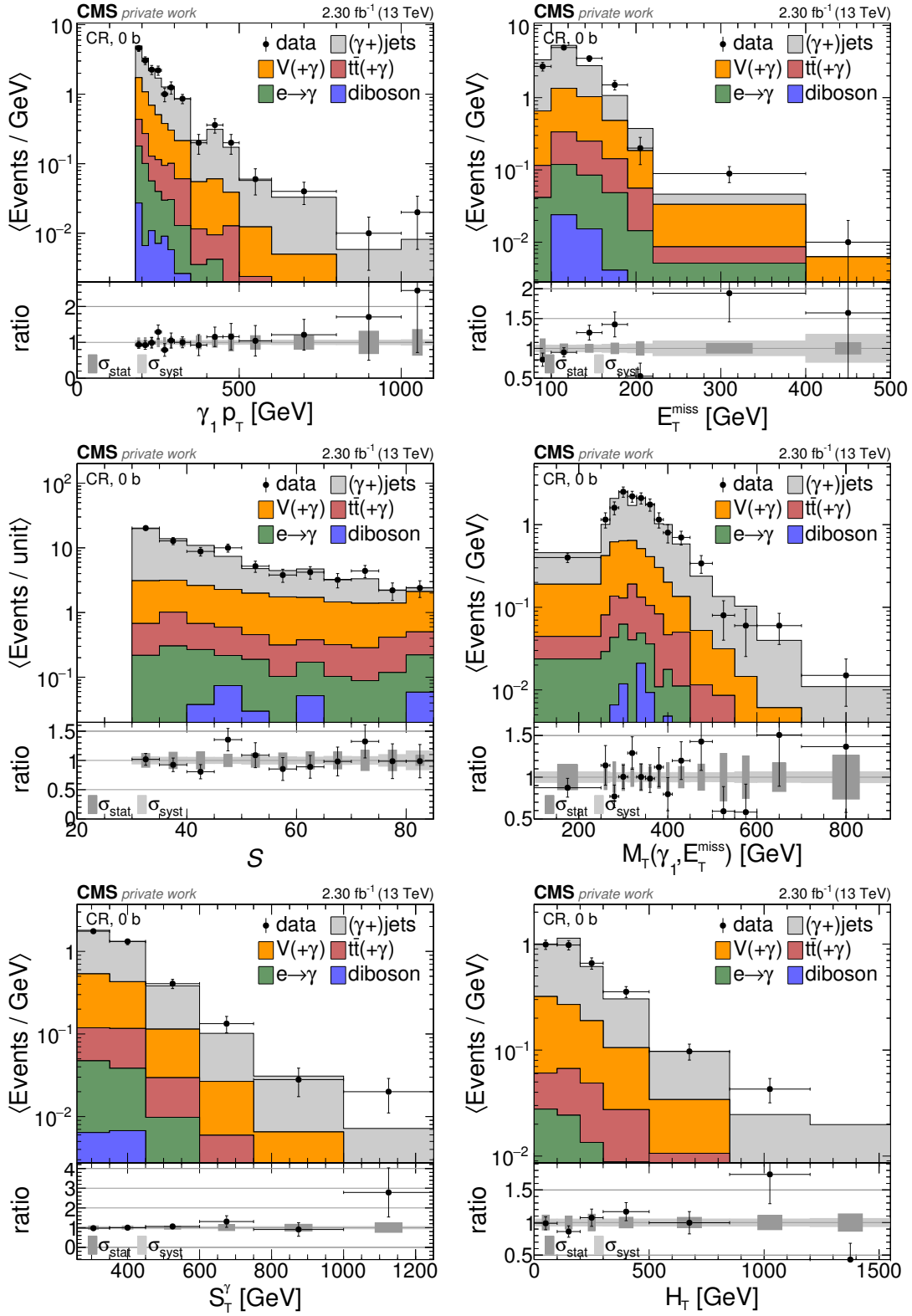

Figure 4.12: Comparison of the total background prediction to data in the control region with a b-tag veto. The overflow is contained in the last bin. The bin contents are divided by the bin widths.

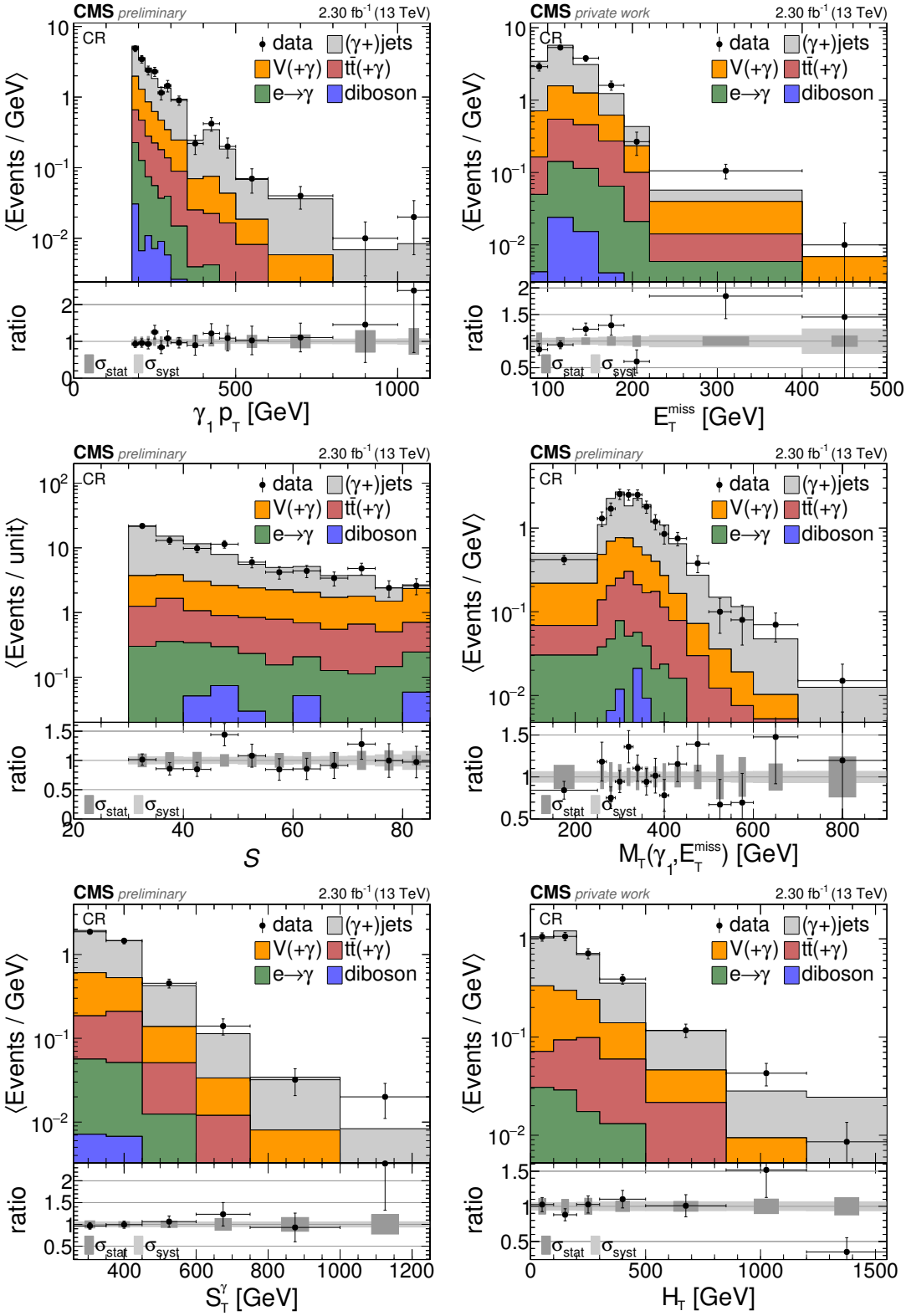

Figure 4.13: Comparison of the total background prediction to data in the control region without a b-tag veto. The overflow is contained in the last bin. The bin contents are divided by the bin widths. Partially published in [1].

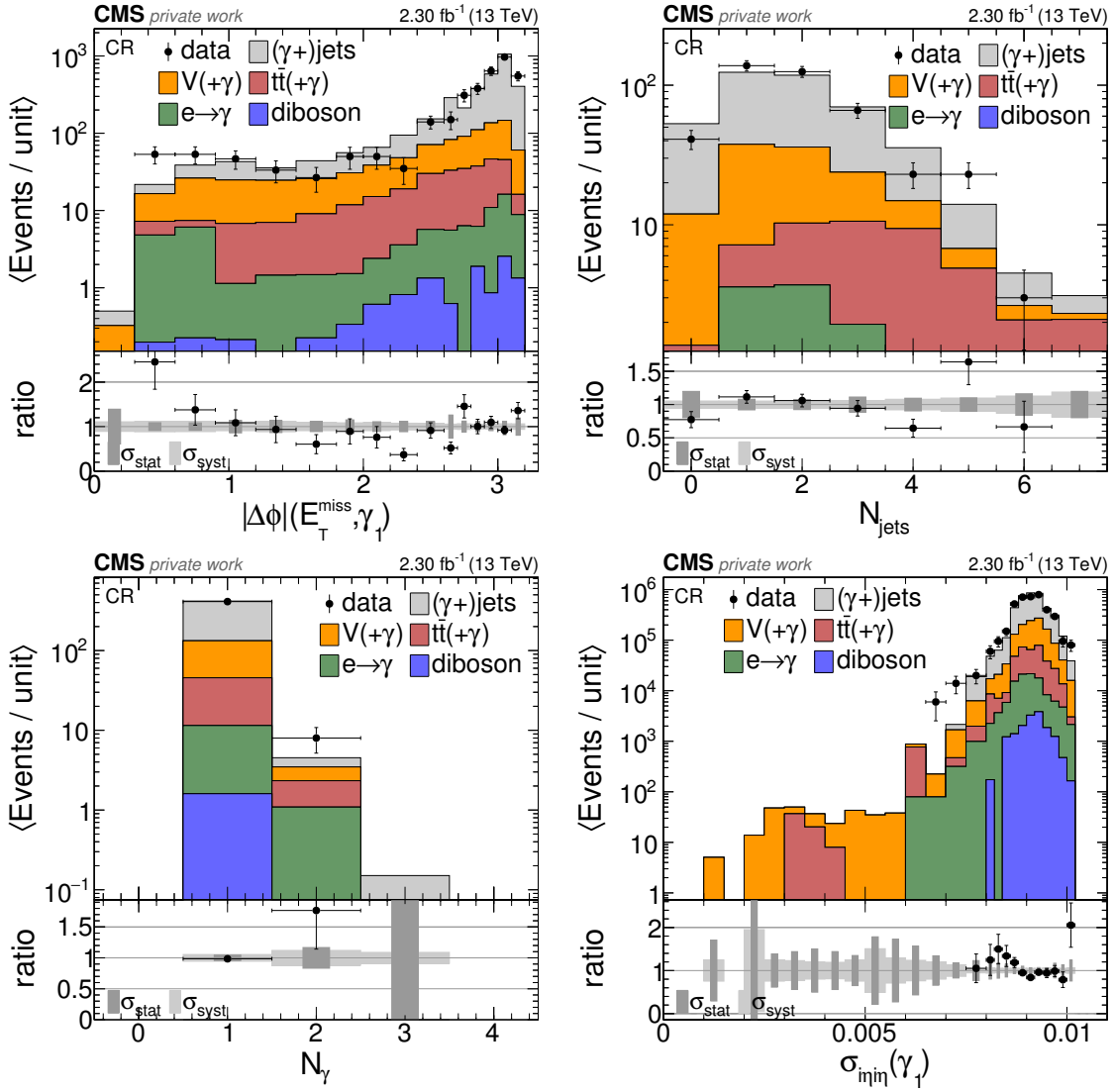

Figure 4.14: Comparison of the total background prediction to data in the control region without a b-tag veto. The overflow is contained in the last bin. The bin contents are divided by the bin widths.

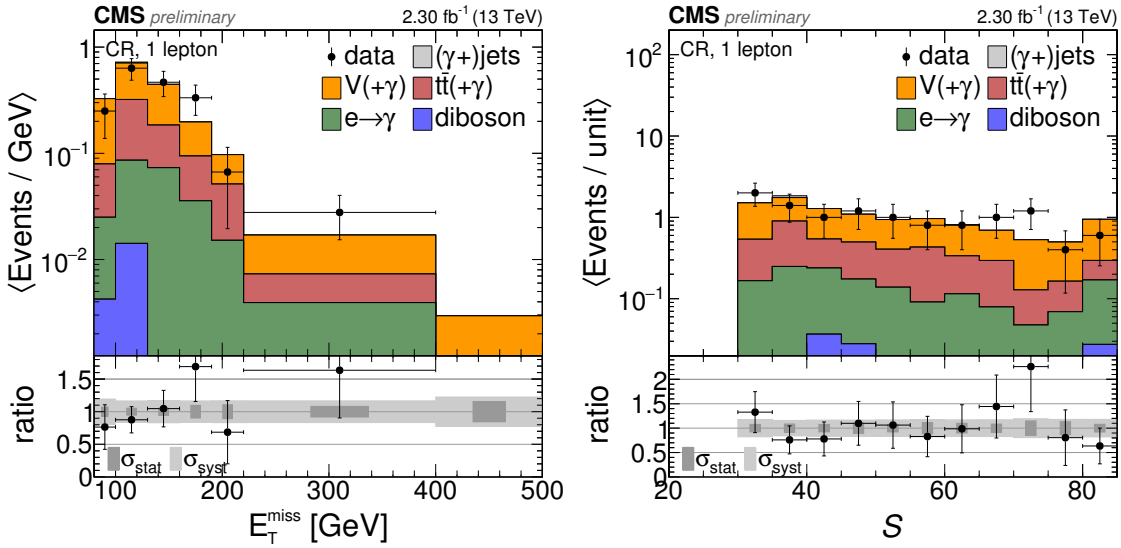

Figure 4.15: Comparison of the total background prediction to data in the CR requiring one lepton. The overflow is contained in the last bin. The bin contents are divided by the bin widths [1].

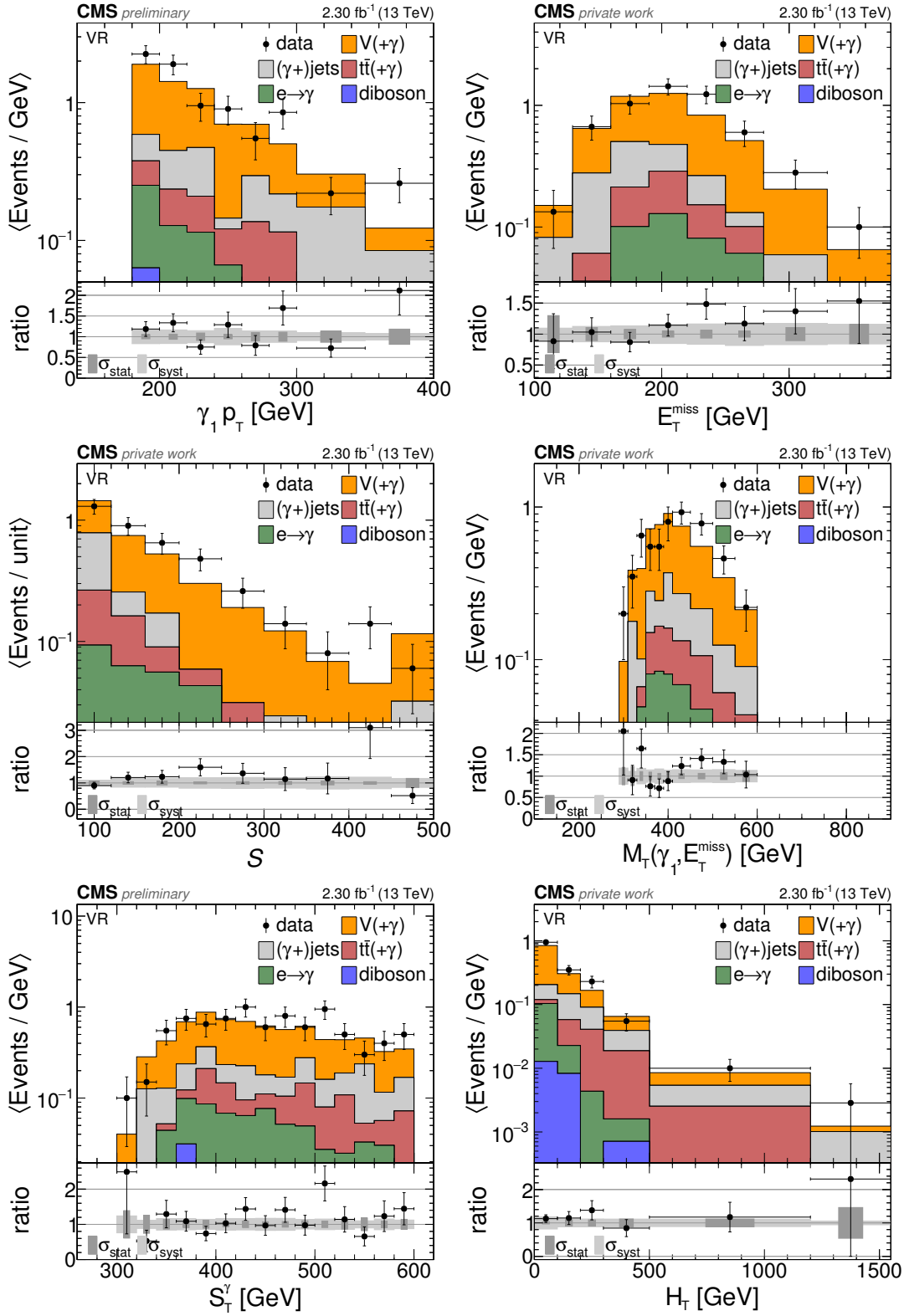

Figure 4.16: Validation of the background prediction in the validation region (VR). The overflow is contained in the last bin. The bin contents are divided by the bin widths. Partially published in [1].

4.5 Study of non-collision backgrounds

A possible contribution of non-collision backgrounds that could enter the selection is checked, namely:

Beam halo: A beam halo muon may radiate a photon, which is reconstructed in the ECAL. Since its momentum is mainly parallel to the beam axis and only photons reconstructed in the barrel are used, the ECAL shower is expected to be spread mainly in η, resutling in a large value of $\sigma_{i\eta i\eta}$. The photons still passing the upper $\sigma_{i\eta i\eta}$ threshold included in the photon identification would be reconstructed at large $|\eta|$. Due to the momentum imbalance caused by such an object, the missing transverse energy would be back-to-back with the photon ($|\Delta\phi| \approx \pi$).

ECAL spikes: Spontaneous discharges in the avalanche photodiodes of the ECAL barrel cause unphyiscal energy entries. Events passing the standard filtering vetoing such occurances typically contain a reconstructed photon with a shower width close to zero ($\sigma_{i\eta i\eta} \approx 0$). These events also cause a back-to-back topology of $E_{\mathrm{T}}^{\mathrm{miss}}$ and the photon.

To check for both effects, the $|\Delta\phi|(E_{\mathrm{T}}^{\mathrm{miss}}, \gamma)$ and $\sigma_{i\eta i\eta}$ distributions are investigated. For this purpose, the lower thresholds for $\sigma_{i\eta i\eta}$ and $\sigma_{i\phi i\phi}$ described in Section 3.1 are omitted. Figure 4.17 shows the distributions for $|\eta|(\gamma) > 1.0$ in the CR (left) as well as in the SR (right). No indication of non-collision background contribution is observed.

To further check for ECAL spike events, the $\sigma_{i\eta i\eta}$ distribution is shown without the $|\eta|(\gamma) > 1.0$ requriement in Fig. 4.18, again separately for the CR (left) and SR (right). While the control region does not show any suspicious behaviour, the signal region contains three events with $\sigma_{i\eta i\eta} \approx 0$, assumed to be ECAL spikes. All three events exhibit the typical back-to-back topology:

1) $p_{\mathrm{T}}(\gamma_1) = 290\,\mathrm{GeV}$ $\sigma_{i\eta i\eta} = 0.000031$ $E_{\mathrm{T}}^{\mathrm{miss}} = 288\,\mathrm{GeV}$ $\Delta\phi(E_{\mathrm{T}}^{\mathrm{miss}}, \gamma_1) = 3.12$
2) $p_{\mathrm{T}}(\gamma_1) = 308\,\mathrm{GeV}$ $\sigma_{i\eta i\eta} = 0.000011$ $E_{\mathrm{T}}^{\mathrm{miss}} = 310\,\mathrm{GeV}$ $\Delta\phi(E_{\mathrm{T}}^{\mathrm{miss}}, \gamma_1) = 3.11$
3) $p_{\mathrm{T}}(\gamma_1) = 397\,\mathrm{GeV}$ $\sigma_{i\eta i\eta} = 0.000009$ $E_{\mathrm{T}}^{\mathrm{miss}} = 421\,\mathrm{GeV}$ $\Delta\phi(E_{\mathrm{T}}^{\mathrm{miss}}, \gamma_1) = -3.14$

To reject this type of events, the requirements $\sigma_{i\eta i\eta} > 0.001$ and $\sigma_{i\phi i\phi} > 0.001$ already listed in Section 3.1 are applied, because the expected signature of a real photon includes a finite shower width.

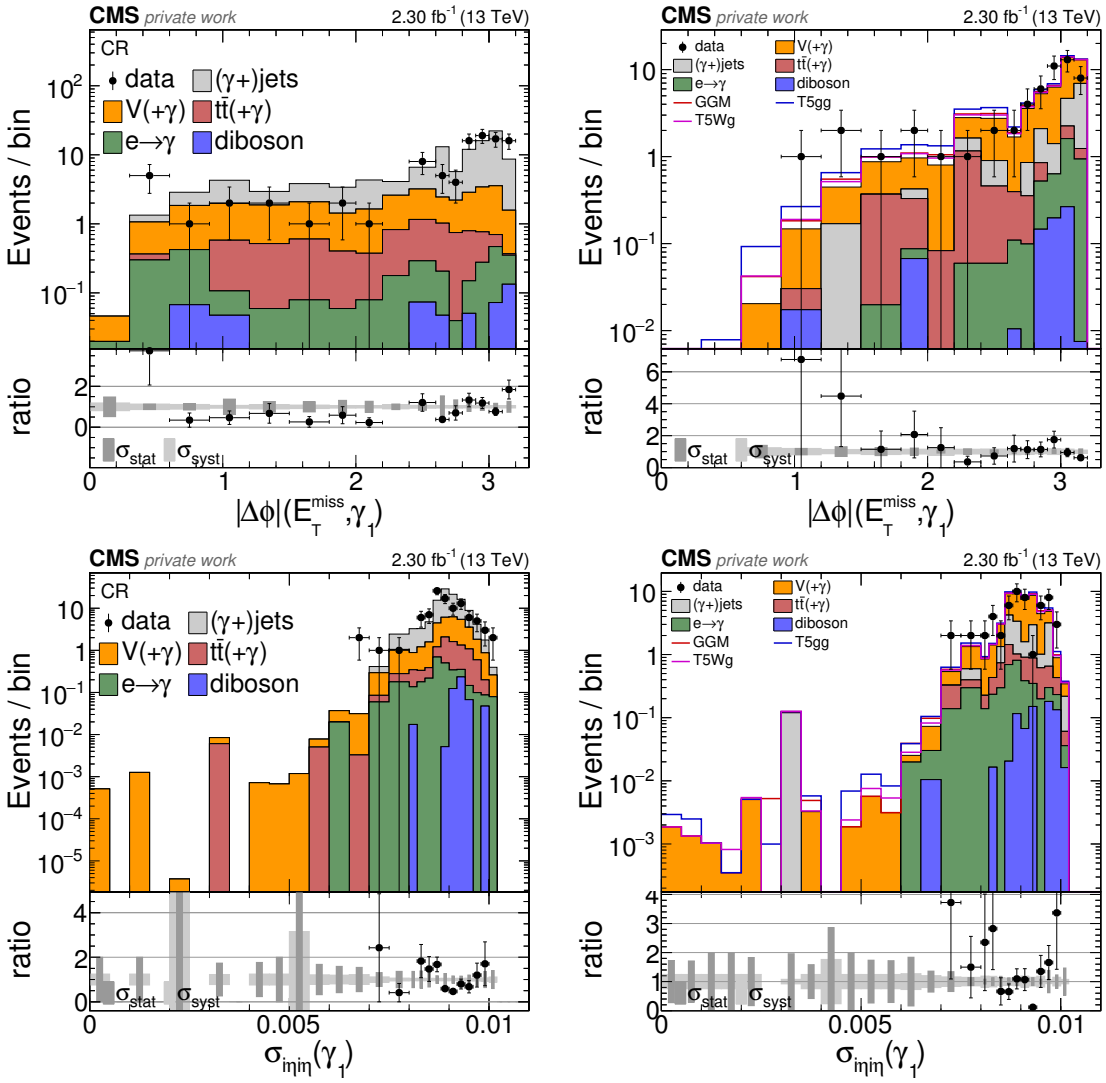

Figure 4.17: Non-collision background check using the $|\Delta\phi|(E_{\mathrm{T}}^{\mathrm{miss}},\gamma)$ and $\sigma_{i\eta i\eta}$ distributions for $|\eta|(\gamma) > 1.0$ in the CR (left) and SR (right).

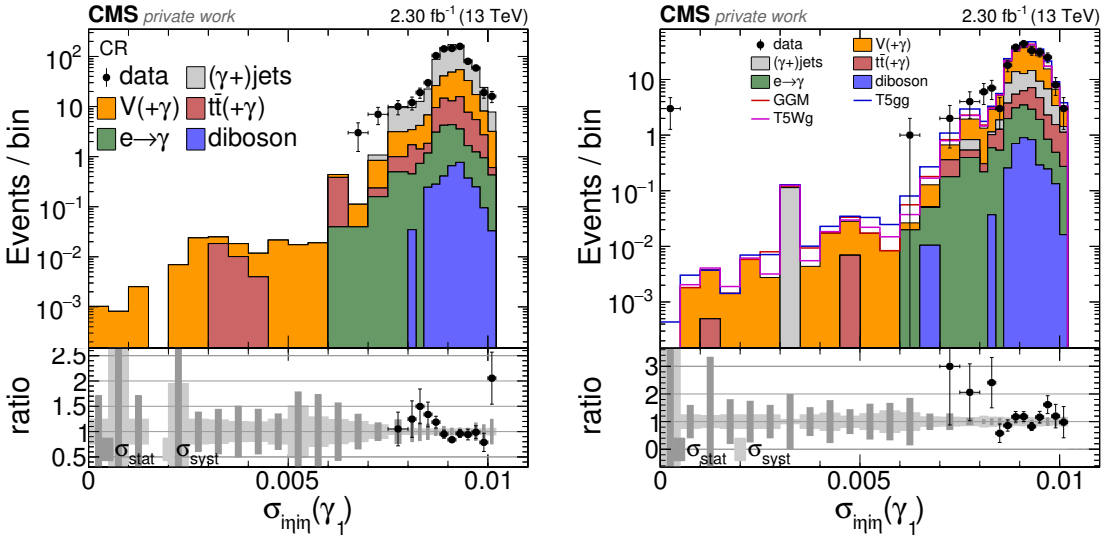

Figure 4.18: Check for ECAL-spike events using the $\sigma_{i\eta i\eta}$ distribution without the $|\eta|(\gamma) > 1.0$ requirement in the CR (left) and SR (right).

5 Results

Contents

The background estimation has been validated and found to be stable. It can be applied in the signal region, $\mathcal{S} > 80$, $M_{\mathrm{T}} > 300\,\mathrm{GeV}$, and $S_{\mathrm{T}}^{\gamma} > 600\,\mathrm{GeV}$, to check if it agrees with the data or if an excess of events is observed, indicating the presence of BSM physics.

5.1 Signal region binning

In order to be sensitive to the possible production of SUSY particles, a distribution has to be chosen that has discriminative power, meaning that it separates the SM background from the SUSY signal searched for. The simplest approach then is to find a selection threshold (cut) for the chosen variable such that the impact of possible signal above (or below) the threshold would be as significant as possible. The background and data event yields passing the cut can be compared to evaluate their compatibility. To further increase the sensitivity, one can increase the number of regions where yields are counted. Instead of a single cut, several bins are constructed, in each of which the data yield is compared to the background prediction.

Candidate distributions for this binning are photon p_{T}, $E_{\mathrm{T}}^{\mathrm{miss}}$, $\mathcal{S}$, and S_{T}^{γ}, which are shown in Fig. 5.1 for the background and the three example signal points. Signal and background are stacked to see the impact of the signal. No data is shown yet, since the data distribution is not supposed to influence the choice of the binning. In all these cases the signal would be best visible at large values, while the regions at lower values are dominated by background, making a possible signal contribution undetectable. The variables investigated further in the following are $\mathcal{S}$ and S_{T}^{γ}.

To quantify the potential sensitivity, different simulation-based measures can be utilized. A common observable used to estimate the expected significance is

$$\frac{s}{\sqrt{s+b}},$$

where s is the number of signal events and b the number of background events. The denominator $\sqrt{s+b}$ approximates the expected uncertainty of data composed of back-

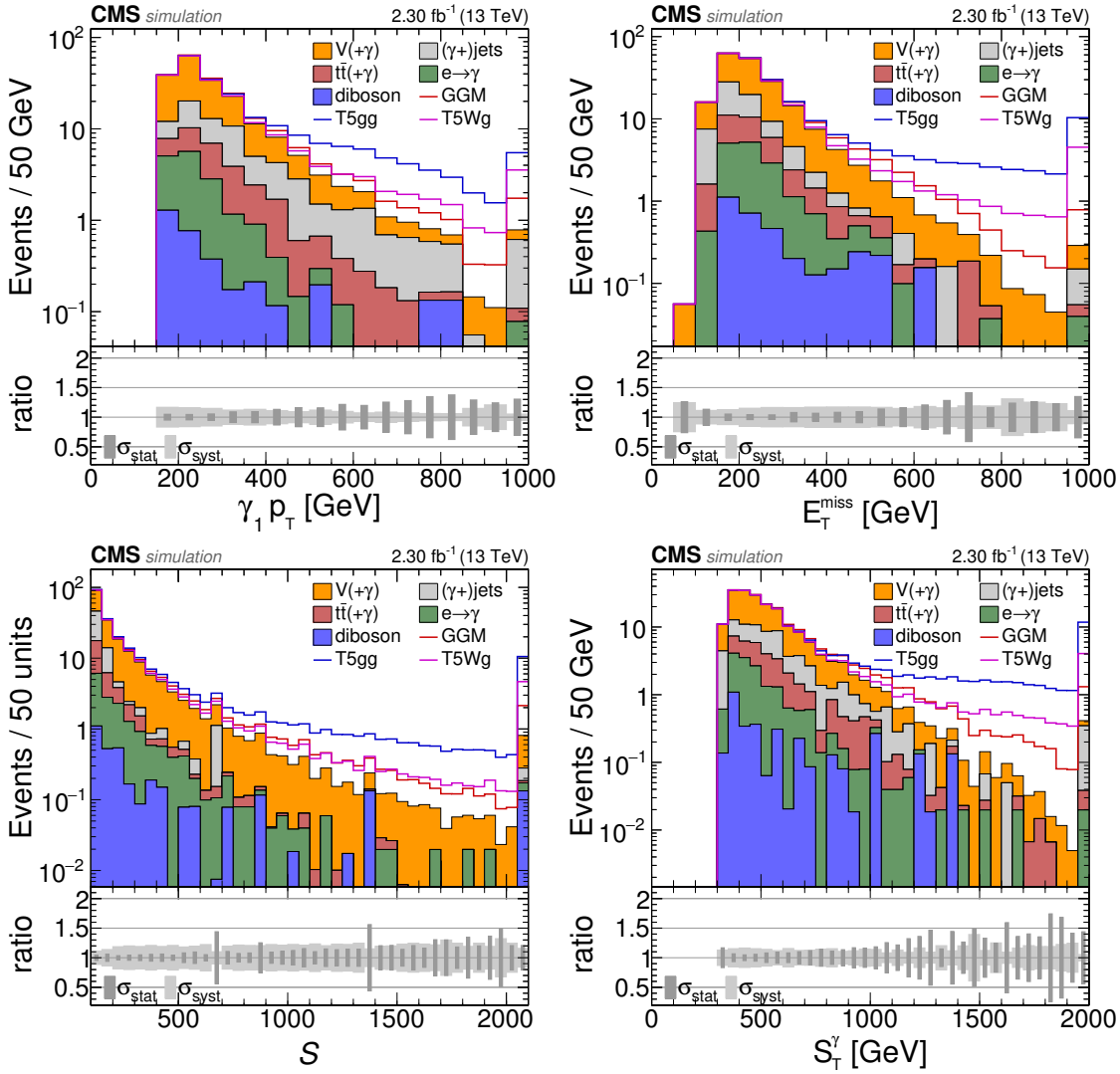

Figure 5.1: Distributions of photon p_T, E_T^{miss}, $\mathcal{S}$, and S_T^{γ} in the signal region (including the part with $S_T^{\gamma} < 600\,\text{GeV}$). No data is shown, but the relative background uncertainty can be seen in the ratio plots. The signals are stacked onto the background and the overflow is contained in the last bin [1].

ground and signal. In the case of a non-negligible statistical background uncertainty $\sigma_{b,stat}$, one can consider its impact using

$$\frac{s}{\sqrt{s+b+\sigma_{b,stat}^2}}.$$

The systematic uncertainty is not considered, since the relative systematic background uncertainty is mostly independent of the cut value and the absolute value of the significance estimate is not of interest here. For the case of data consisting of SM background only, $\sqrt{b}$ approximates the expected data uncertainty. Thus,

$$\frac{s}{\sqrt{b}}$$

can be used to optimize the "exclusion sensitivity", while the former two measures are more suited to compare the "discovery sensitivity" of different distributions and cuts.

All three measures are calculated as a function of a cut c, i.e. for events fulfilling $X > c$, with $X \in \{\mathcal{S}, S_{\mathrm{T}}^{\gamma}\}$. They are shown in Fig. 5.2 for the three example signals. It should be noted that all sensitivity measures also depend on the masses used in any of the models. No real optimization with respect to a specific model or mass range is performed, in order to avoid being too targeted at a specific scenario, but these studies are performed to get an idea of a sensible range to define bin boundaries. Additionally, the maximal values reached with the different distributions can be compared. The main focus is on the GGM signal point, especially on $s/(s+b)^{1/2}$.

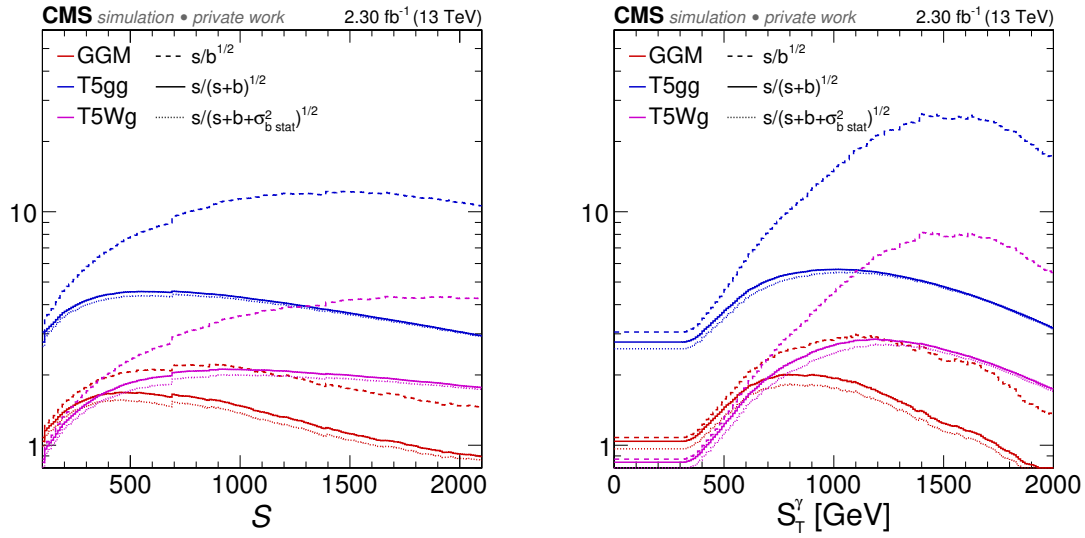

Figure 5.2: The different sensitivity measures for the three example signals. The x-axes label the cut of the variable used.

In all cases, S_{T}^{γ} reaches a slightly better maximal sensitivity than $\mathcal{S}$, which is why it is chosen for the cut. The value is not set exactly such that one sensitivity measure is maximal, because this is only valid for the studied mass point. A cut of $S_{\mathrm{T}}^{\gamma} = 1000\,\mathrm{GeV}$ is chosen. To further make use of the region with $S_{\mathrm{T}}^{\gamma} < 1000\,\mathrm{GeV}$, the procedure is repeated iteratively to define three exclusive bins in S_{T}^{γ} [GeV], with the boundaries

$$[600, 800, 1000, \infty]\,.$$

The part with $S_{\mathrm{T}}^{\gamma} < 600\,\mathrm{GeV}$ is not signal sensitive and therefore excluded from the SR (cf. Section 3.4), and used as a validation region to test the background prediction, as described in Section 4.4.

A two-dimensional binning of the SR, as used in the $\sqrt{s} = 8\,\mathrm{TeV}$ analysis, has also been studied. No significance gain could be observed with respect to the one-dimensional binning and therefore the latter is used for the search.

5.2 Event yields

The background distribution in the signal region using the final binning in S_T^γ is shown in Fig. 5.3. To see the expected impact of signal presence, the three example signal points are stacked onto the total background prediction. The shown data yields are in good agreement with the SM background prediction and no evidence for SUSY is observed.

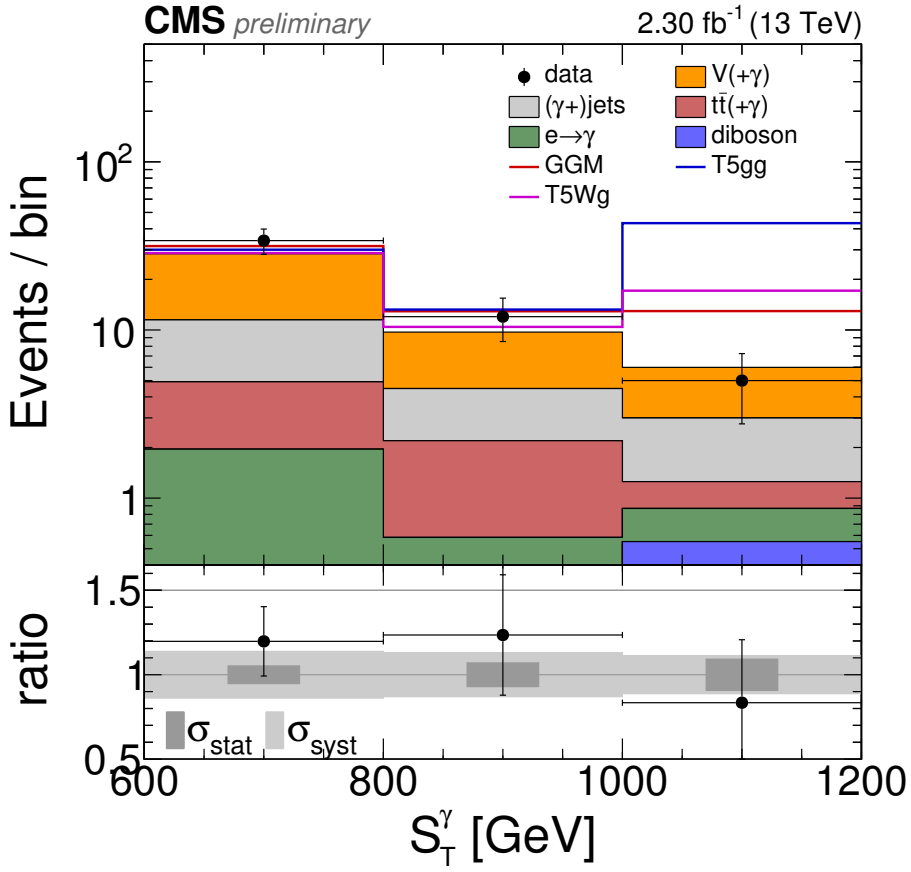

Figure 5.3: Background and data distributions in the signal region using the final binning in S_T^γ. The last bin contains the overflow. The background and signal histograms are stacked [1].

Additionally, the yields for the individual bins can be found in Table 5.1. The systematic uncertainties of the single background components are combined, taking the correlation term for V(+γ) and (γ+)jets into account. The contributions of the individual background components are listed in Table 5.2 together with the corresponding uncertainties.

Table 5.1: Yields for the individual SR bins. For the total systematic uncertainties the correlation term for the systematic uncertainties of V(+γ) and (γ+)jets has been considered [1].

S_T^γ [GeV]	prediction	σ_{stat}	σ_{syst}	data
600– 800	28.4	±1.5	±4.1	34
800–1000	9.7	±0.7	±1.3	12
1000– ∞	6.0	±0.6	±0.7	5

Table 5.2: Individual background yields for the separate signal region bins. The statistical uncertainty of the e → γ background is due to the limited size of the collected data sample. All other statistical uncertainties are due to the limited number of simulated events [1].

S_T^γ bin	600 − 800 GeV			800 − 1000 GeV			1000 − ∞ GeV		
	yield	σ_{stat}	σ_{syst}	yield	σ_{stat}	σ_{syst}	yield	σ_{stat}	σ_{syst}
V(+γ)	16.90	0.27	4.16	5.23	0.12	1.29	3.00	0.09	0.74
(γ+)jets	6.57	1.40	1.03	2.29	0.56	0.36	1.74	0.47	0.27
$t\bar{t}$(+γ)	2.96	0.41	0.89	1.61	0.34	0.48	0.39	0.09	0.12
e → γ	1.62	0.18	0.49	0.36	0.08	0.11	0.32	0.08	0.09
diboson	0.33	0.16	0.07	0.23	0.15	0.05	0.55	0.26	0.11

5.3 Statistical interpretations

No evidence for physics beyond the standard model is found, but limits can be calculated to constrain the still allowed parameter space of different GMSB SUSY models. The focus is on models of electroweak production. Additionally, two strong production models with gluino pair production are considered.

Signal acceptance and signal contamination

The signal acceptances for all four models are shown in Fig. 5.4 as functions of the mass parameters of the individual models, i.e. the bino and wino masses ($m_{\tilde{B}}$, $m_{\tilde{W}}$) for GGM, the single NLSP mass parameter for TChiWg, and the gluino and neutralino/chargino masses for T5gg/T5Wg. In all cases, the signal acceptances are larger for high NLSP masses, due to the resulting large values of photon p_T and E_T^{miss}, and consequently large $\mathcal{S}$ and M_T. Accordingly, the acceptance drops significantly towards low NLSP masses, especially when the photon from the NLSP decay can no longer pass the trigger threshold.

Signal events not passing the SR selection criteria may contribute to the data in the CR. An increased data yield would result in an overprediction of the scale factors for the main backgrounds, which are determined in the CR as described in Section 4.1. Consequently, the backgrounds in the SR would be overestimated, reducing the sensitivity for a possible signal. It has been verified that this form of signal contamination does not influence the fit results significantly for low signal contributions in the CR (cf. Section 4.1).

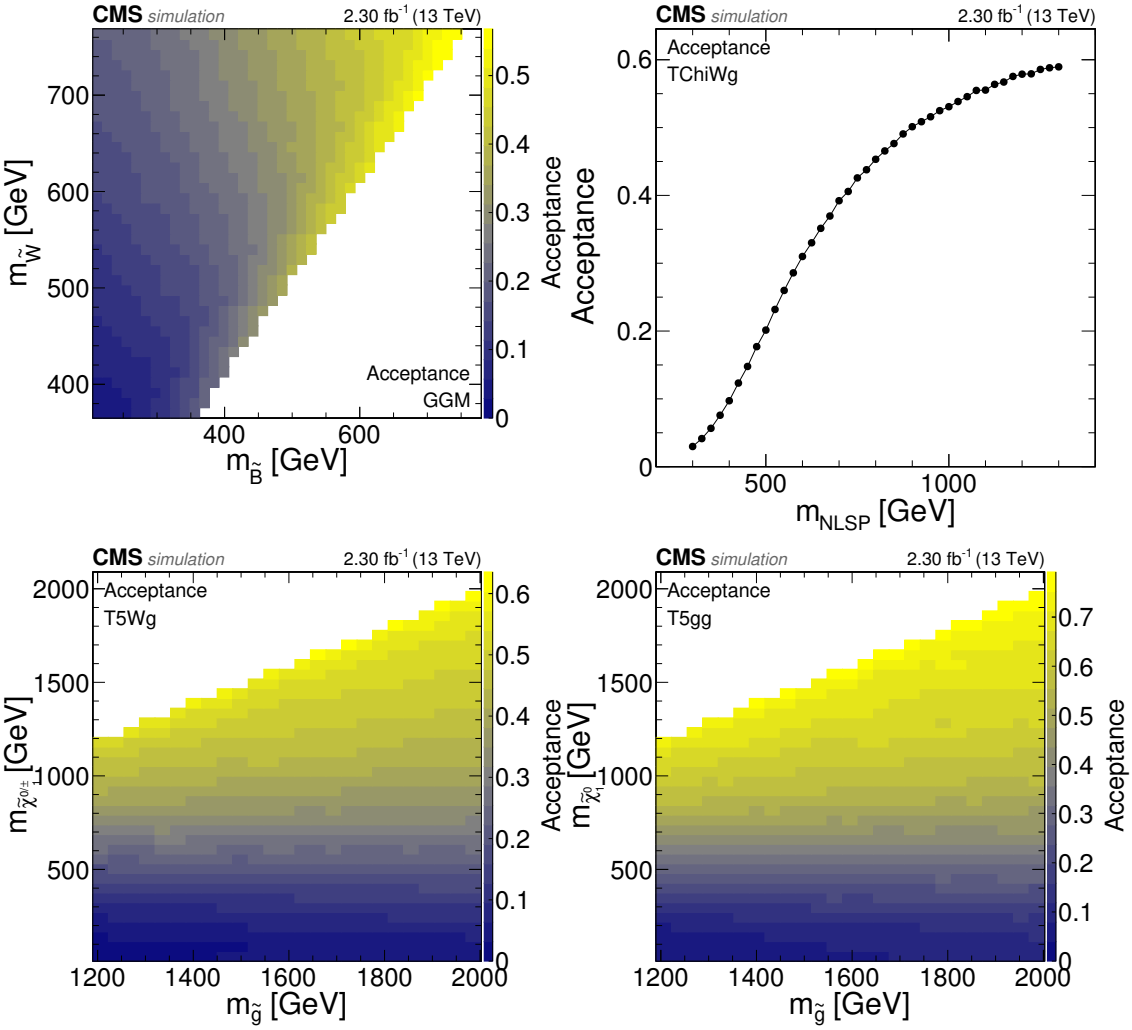

Figure 5.4: The signal acceptances of the SR selection depending on the mass(es) of the models [1].

For low masses of the initially produced sparticles, the signal cross section can be large enough that the possible signal contribution to the data in the CR can reach multiples of 10%. This is the case if the NLSP mass is low and thus many events do not pass the criterion $M_{\mathrm{T}} > 300\,\mathrm{GeV}$ of the SR.

To be able to correct for signal contamination in a simple way, only signal points with a low contamination are considered for the statistical interpretation. Since the background uncertainty exceeds 10% in all SR bins, a maximum hypothetical signal contribution κ of 5% to the CR event yield is accepted. As long as the contribution is this small, the relative normalization distortion in the CR is assumed to directly translate into the SR, resulting in a relative background overprediction of κ. Only mass points meeting this requirement are shown in the acceptance and limit plots.

The remaining effect for the considered mass points is corrected by subtracting the overprediction from the background yield b. The technical implementation allows only

to specify a single background yield b and a single signal yield s, from which both, the signal-only and the signal+background hypothesis (described below), are constructed. By definition signal contamination can only have an effect for the signal+background and not for background-only hypothesis. Therefore, the overprediction is subtracted from the signal yield instead of the background yield, because it has the same effect on $s + b$, while b remains unaffected.

Upper cross section limit calculation

Upper limits on the production cross section are calculated for the different models at 95% confidence level (CL) using a frequentist $\mathrm{CL_s}$ approach [132–134] with a profile likelihood test statistic and asymptotic formulae [135]. The background-only hypothesis b is compared to the signal+background hypothesis $s + b$. A multiplicative signal strength modifier μ for the signal contribution is introduced, such that both hypotheses can be expressed in a unified form, $\mu s + b$. All systematic uncertainties are treated as nuisance parameters, collectively denoted θ. The test statistic $\tilde{q}_\mu$ for a tested signal strength μ is constructed using a likelihood ratio,

$$\tilde{q}_\mu = -2 \ln \frac{\mathcal{L}(\text{data} \mid \mu, \hat{\hat{\theta}}_\mu)}{\mathcal{L}(\text{data} \mid \hat{\mu}, \hat{\theta})},$$

with the likelihood $\mathcal{L}$ being the product of all search channels' Poisson probabilities for the observed yields, additionally incorporating probability density functions for the systematic uncertainties. The likelihood in the denominator is evaluated given $\hat{\mu}$ and $\hat{\theta}$, that globally maximize $\mathcal{L}$, with the constraint $\hat{\mu} \in [0, \mu]$, while $\hat{\hat{\theta}}_\mu$ is the maximum likelihood estimator for θ given μ. The observation of $\tilde{q}_\mu$ made in the experiment is denoted $\tilde{q}_\mu^{\text{obs}}$. Using the probability $\mathrm{CL_{s+b}}$ to observe $\tilde{q}_\mu \geq \tilde{q}_\mu^{\text{obs}}$ given the signal+background hypothesis and the probability $\mathrm{CL_b}$ to observe $\tilde{q}_\mu \geq \tilde{q}_\mu^{\text{obs}}$ given the background-only hypothesis, the measure

$$\mathrm{CL_s} = \frac{\mathrm{CL_{s+b}}}{\mathrm{CL_b}}$$

is calculated. The $(1 - \alpha)$ CL upper limit on μ is found by varying μ until $\mathrm{CL_s} = \alpha$ is reached [134]. Conventionally, $1 - \alpha = 95\%$ is used. In the following, the limits on μ for different models are directly translated to upper cross section limits.

The calculation is done in the framework developed by the LHC Higgs Combination Group [134], in which the systematic uncertainties are treated as nuisance parameters that are either uncorrelated or 100% (anti-)correlated. Most of the uncertainties can be directly assigned to one of those two categories, as described in Section 4.3. The correlation of the fit uncertainty for the main backgrounds of −64%, determined in Section 4.1, is considered by decomposing the uncertainties into a fully correlated and an uncorrelated part, as described in detail in Appendix C.

Cross section limits and exclusion contours

Based on the upper cross section limit for a specific mass point, it is decided if it can be excluded. If the theoretical cross section exceeds the limit, the point can be excluded

at the quoted CL. In the two-dimensional mass planes, contours around the excluded regions are determined. Expected limits and contours can be determined, reflecting the expectation for hypothetical data distributed according to the SM prediction.

The observed upper cross section limits are shown in Fig. 5.5 for the GGM model together with the observed and expected exclusion contours in the bino-wino ($m_{\tilde{B}}$–$m_{\tilde{W}}$) mass plane. The observed limit contour is weaker than the expected at lower bino masses, because these correspond to lower photon p_T and E_T^{miss}. Therefore, the first two signal region bins, which show slight overfluctuations, have a larger influence. For larger NLSP masses, the last SR bin is more important. Here, a small underfluctuation is observed, resulting in a stronger observed limit. Near the mass diagonal, bino masses of up to ≈ 675 GeV can be excluded. Bino masses below 300 GeV cannot be excluded, since the low E_T^{miss} and photon p_T lead to a signal acceptance loss, as described above.

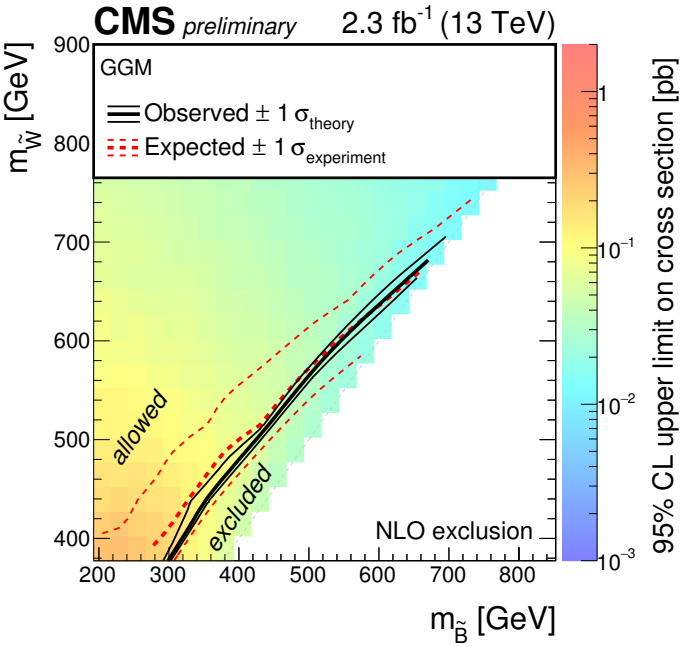

Figure 5.5: The 95% CL limits for the GGM model in the bino-wino mass plane. The color scale encodes the observed upper cross section limit for each point. The lines represent the observed (black) and expected (red) exclusion contours and their uncertainties [1].

Figure 5.6 shows observed and expected upper cross section limits as a function of the single NLSP mass parameter for the TChiWg simplified model. Masses below the intersection with the theoretical cross section at approximately 450 GeV can be excluded at 95% CL.

For the GGM and TChiWg models of electroweak production, the exclusion limits cannot be improved with respect to the predecessor analysis, due to the strongly increased trigger threshold and the low integrated luminosity of less than a third compared to the search at $\sqrt{s} = 8$ TeV [57], which are not compensated by the increased production cross section at $\sqrt{s} = 13$ TeV. With the large dataset recorded in 2016, a large sensitivity gain is expected, though.

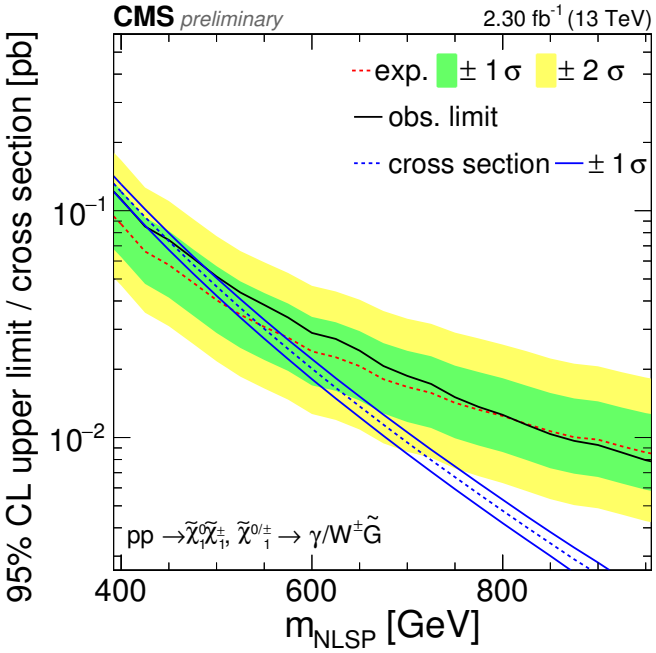

Figure 5.6: Observed and expected upper cross section limits as a function of the NLSP mass for the TChiWg model together with the theoretical cross section [1].

The cross section increase with respect to $\sqrt{s} = 8\,\text{TeV}$ for the gluino pair production models is much larger and therefore a large sensitivity is expected. No interpretations for strong production scenarios have been published by the $\sqrt{s} = 8\,\text{TeV}$ analysis, making a direct comparison impossible. The cross section limits and exclusion contours in the gluino-neutralino/chargino mass plane for the T5gg and T5Wg models are shown in Figs. 5.7 and 5.8. For both, the acceptance loss at low NLSP masses causes the same sensitivity drop as for the electroweak models. The currently strongest limit set by CMS for the T5gg model is provided by the search requiring two photons in the final state (using the same dataset as this search), excluding gluino masses below approximately 1550 GeV for $m_{\tilde{\chi}^0_1} > 200\,\text{GeV}$ [60]. Here, $m_{\tilde{g}} \lesssim 1740\,\text{GeV}$ can be excluded near the mass diagonal, improving the limit in this region. The sensitivity for the T5Wg model is slightly worse than for the T5gg model, because only one photon contributes to S_{T}^{γ}. Near the mass diagonal, $m_{\tilde{g}} \lesssim 1690\,\text{GeV}$ can be excluded, improving the limits set in $\sqrt{s} = 8\,\text{TeV}$ searches [48].

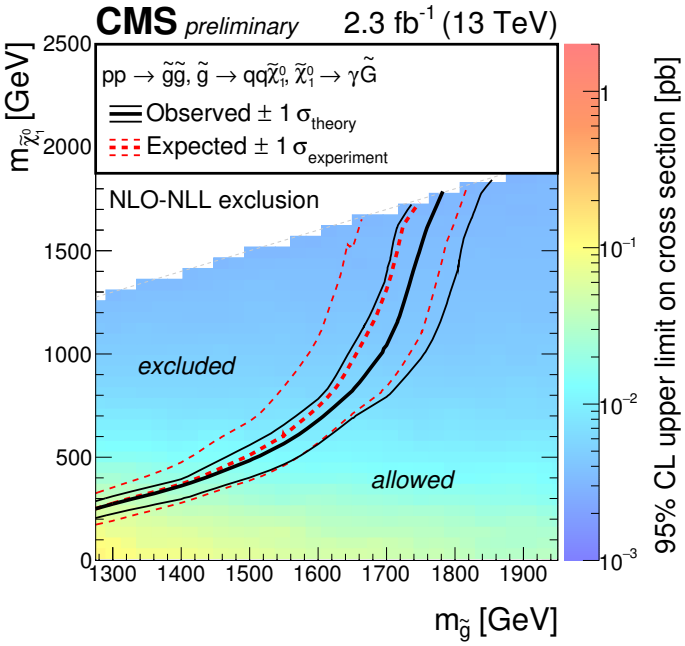

Figure 5.7: The 95% CL limits for the T5gg model in the gluino-neutralino mass plane. The color scale encodes the observed upper cross section limit for each point. The lines represent the observed (black) and expected (red) exclusion contours and their uncertainties [1].

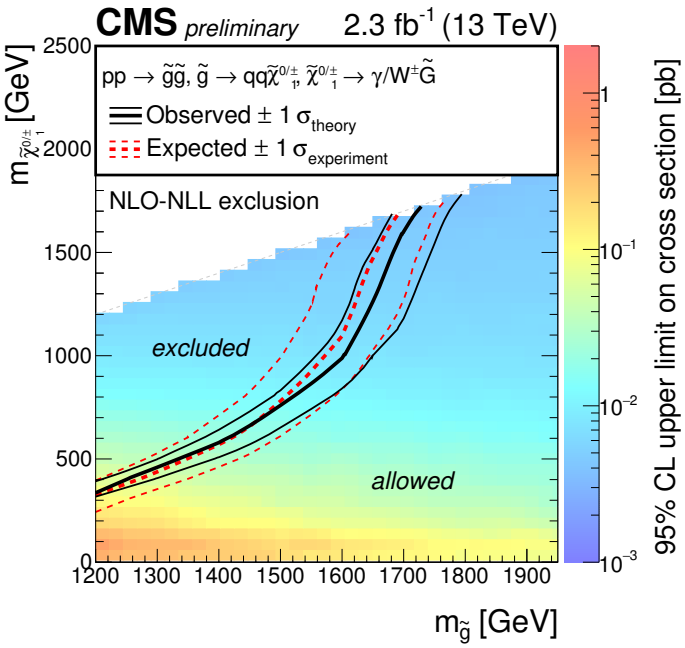

Figure 5.8: The 95% CL limits for the T5Wg model in the gluino-neutralino mass plane. The color scale encodes the observed upper cross section limit for each point. The lines represent the observed (black) and expected (red) exclusion contours and their uncertainties [1].

5.4 Summary

In this thesis a search for the production of supersymmetric particles decaying to photons is presented, with a focus on electroweak gaugino production. Proton-proton collisions recorded with the CMS detector at the Large Hadron Collider in its Run II are investigated. The recorded data sample corresponds an integrated luminosity of $2.3\,\text{fb}^{-1}$, recorded in 2015 at $\sqrt{s} = 13\,\text{TeV}$.

A cut-and-count experiment is performed in three exclusive search bins. The main backgrounds are W and Z boson production in association with a photon and QCD multijet events with photon radiation. They are estimated simultaneously using a template fit of simulated samples to data in a signal-depleted control region. The resulting scale factors are applied to the simulated samples in the search region. Background from electrons misidentified as photons are determined using a data-driven tag-and-probe method. Further backgrounds are estimated completely from simulation. The observed event counts are in agreement with the standard model prediction and no evidence for physics beyond the standard model is observed.

Exclusion limits at the 95% confidence level are set for a general gauge mediation model of electroweak production and the simplified model TChiWg. The limits for the electroweak production models cannot be improved with respect to the predecessor search carried out using $7.4\,\text{fb}^{-1}$ recorded at $\sqrt{s} = 8\,\text{TeV}$. A much larger sensitivity is expected with more integrated luminosity collected at $\sqrt{s} = 13\,\text{TeV}$ in the 2016 data taking.

Additionally, limits are set for two simplified models of gluino pair production with final states with two photons (T5gg) or one photon and a W boson (T5Wg). The currently best limits set by CMS are improved in regions with large NLSP masses.

Appendix A

Technical details of the GGM signal generation

The GGM signal is produced privately, using the SLHA files of the `Spectra_WB` grid provided by [43]. These have also been used for the predecessor search at $\sqrt{s} = 8\,\text{TeV}$. For a given mass point of the grid, all masses of the sparticles, their decay widths, and their branching ratios are encoded in a single SLHA file, except the decay of the NLSP, i.e. $\widetilde{\chi}_1^0 \to \widetilde{\text{G}}\gamma$ and $\widetilde{\chi}_1^0 \to \widetilde{\text{G}}\text{Z}$. The $\sqrt{s} = 8\,\text{TeV}$ GGM signal was generated with PYTHIA 6, which has an option

```
'IMSS(11) = 1 !  Set gravitino as LSP',
```

that automatically handles the NLSP decay.

The GGM signal for this search is simulated with PYTHIA 8, in which this option is not present. Accordingly, it has been added manually to the SLHA files, with the branching ratios calculated according to Eq. (1.2) on page 7. For $m_{\widetilde{\chi}_1^0} < m_{\text{Z}}$ the branching ratios are set to 0% and 100%, respectively, as shown in Fig. 1.2. The gravitino mass and decay width are both set to 1 GeV. Example additions for the point $m_{\widetilde{\text{W}}} = 640\,\text{GeV}, m_{\widetilde{\text{B}}} = 630\,\text{GeV}$ can be found in Listing A.1.

Listing A.1: Example additions (`diff`) to the SLHA file for the point $m_{\widetilde{\text{W}}} = 640\,\text{GeV}$, $m_{\widetilde{\text{B}}} = 630\,\text{GeV}$.

```
--- M2_640_M1_630.slha  2015-11-20 09:56:08.158502456 +0100
+++ M2_640_M1_630_chi01decays.slha      2015-11-25 09:20:20.355879898 +0100
@@ -113,6 +113,7 @@
    1000035     2.00417784E+03   # ~chi_40
    1000024     6.37545019E+02   # ~chi_1+
    1000037     2.00391687E+03   # ~chi_2+
+   1000039     1.00000000E+00   # ~G
 #
 BLOCK NMIX  # Neutralino Mixing Matrix
   1  1     9.86867903E-01   # N_11
@@ -521,3 +522,9 @@
      2.99309464E-01    2    -1000024        24   # BR(~chi_40 -> ~chi_1-   W+)
      1.37775091E-01    2     1000022        25   # BR(~chi_40 -> ~chi_10   h )
      2.20478260E-01    2     1000023        25   # BR(~chi_40 -> ~chi_20   h )
+#
+#         PDG            Width
+DECAY   1000022     1.00000000E+00   # neutralino1 decays
+#          BR         NDA      ID1       ID2
+     7.83493292E-01    2     1000039        22   # BR(~chi_10 -> ~G gamma)
+     2.16506708E-01    2     1000039        23   # BR(~chi_10 -> ~G Z    )
```

A template `CMSSW` configuration for the signal generation is generated using the `cmsDriver` command shown in Listing A.2. It is modified to run PYTHIA 8 with the corresponding GGM SLHA file as input. The important fragments that have been added can be seen in Listing A.3. The final configuration is run with the `cmsRun` command to generate the events for a single mass point. To generate the whole signal scan, the procedure described above is repeated for each mass point.

Listing A.2: `cmsDriver` command to create a template `CMSSW` configuration for the signal generation.

```
cmsDriver.py Configuration/GenProduction/python/SUS-RunIISpring15FSPremix-00077-
    fragment.py --filein dbs:/SMS-T1tttt_mGluino-1050_mLSP-50
    to775_TuneCUETP8M1_13TeV-madgraphMLM-pythia8/RunIIWinter15pLHE-MCRUN2_71_V1-v2/
    LHE --fileout file:SUS-RunIISpring15FSPremix-00077_step1.root --pileup_input
    dbs:/Neutrino_E-10_gun/RunIISpring15PrePremix-MCRUN2_74_V9-v1/GEN-SIM-DIGI-RAW
    --mc --eventcontent AODSIM --fast --customise SLHCUpgradeSimulations/
    Configuration/postLS1CustomsPreMixing.customisePostLS1,Configuration/
    DataProcessing/Utils.addMonitoring --datatier AODSIM --conditions MCRUN2_74_V9
    --beamspot NominalCollision2015 --step GEN,SIM,RECOBEFMIX,DIGIPREMIX_S2:
    pdigi_valid,DATAMIX,L1,L1Reco,RECO,HLT:@frozen25ns --magField 38T_PostLS1 --
    datamix PreMix --python_filename AODSIM_cfg.py --no_exec -n -1
```

Listing A.3: Configuration fragments added to the configuration template for the GGM signal generation.

```
from Configuration.AlCa.GlobalTag_condDBv2 import GlobalTag
process.GlobalTag = GlobalTag(process.GlobalTag, 'MCRUN2_74_V9', '')

from Configuration.Generator.Pythia8CommonSettings_cfi import *
from Configuration.Generator.Pythia8CUEP8M1Settings_cfi import *
with open("M2_640_M1_630_chi01decays.slha") as f:
    SLHA_TABLE=f.read()

process.generator = cms.EDFilter("Pythia8GeneratorFilter",
    pythiaPylistVerbosity = cms.untracked.int32(0),
    filterEfficiency = cms.untracked.double(1.0),
    pythiaHepMCVerbosity = cms.untracked.bool(False),
    comEnergy = cms.double(13000),
    SLHATableForPythia8 = cms.string(SLHA_TABLE),
    maxEventsToPrint = cms.untracked.int32(0),
    PythiaParameters = cms.PSet(
        pythia8CommonSettingsBlock,
        pythia8CUEP8M1SettingsBlock,
        processParameters = cms.vstring(
            'SUSY:all = on',
        ),
        parameterSets = cms.vstring(
            'pythia8CommonSettings',
            'pythia8CUEP8M1Settings',
            'processParameters'
        )
    )
)
process.ProductionFilterSequence = cms.Sequence(process.generator)
# ...
for path in process.paths:
    getattr(process,path)._seq = process.ProductionFilterSequence * getattr(process
        ,path)._seq
```

Appendix B

Alternative trigger choices

The trigger used in the analysis has not been the first choice. Triggers requiring a photon and missing transverse energy are more suited for the search, owing to the expected signal signature, and generally allow lower energy thresholds. Two photon+$E_{\mathrm{T}}^{\mathrm{miss}}$ triggers were considered initially, but found not to be usable for this analysis, as described below.

HLT_Photon36_R9Id90_HE10_Iso40_EBOnly_PFMET40

The photon+$E_{\mathrm{T}}^{\mathrm{miss}}$ HLT path

`HLT_Photon36_R9Id90_HE10_Iso40_EBOnly_PFMET40`

for the 13 TeV data taking in 2015 comes closest to the parked trigger used in Run I and would be a good choice due to the low $E_{\mathrm{T}}^{\mathrm{miss}}$ and photon p_{T} thresholds. Unfortunately, an inefficiency is observed for large photon p_{T}. The measurement of the trigger efficiency in data does not provide enough statistical precision to clearly observe this issue, but the simulation of the trigger can be used to investigate the problem with more precision. The efficiency of the simulated trigger is shown in Fig. B.1 as a function of $E_{\mathrm{T}}^{\mathrm{miss}}$ and photon p_{T}. The efficiency is measured as described in Section 3.4, but separately for both, the photon and the $E_{\mathrm{T}}^{\mathrm{miss}}$ part. For the measurement of the $E_{\mathrm{T}}^{\mathrm{miss}}$ part,

`HLT_Photon36_R9Id90_HE10_IsoM`

is used as the base trigger and

`HLT_PFMET170`

is used for the photon part. Since `HLT_PFMET170` is not simulated, a simple $E_{\mathrm{T}}^{\mathrm{miss}}$ cut is applied as a base selection to measure the photon p_{T} part. A clear drop of the efficiency is observed for large values of p_{T}. The efficiency drop cannot be seen this clearly in data, because the number of events with high energetic photons is too low.

The photon isolation part `Iso40` included in the trigger consists of the three components `EcalPFClusterIso`, `HcalPFClusterIso`, and `hollowTrackIso`. For each one, a p_{T} dependent threshold is required,

- EcalIsoFilter: EcalPFClusterIso $< 4.0\,\mathrm{GeV} + 0.012 \cdot p_{\mathrm{T}}$
- HcalIsoFilter: HcalPFClusterIso $< 4.0\,\mathrm{GeV} + 0.005 \cdot p_{\mathrm{T}}$
- TrackIsoFilter: hollowTrackIso $< 4.0\,\mathrm{GeV} + 0.002 \cdot p_{\mathrm{T}}$.

The distributions of these components are shown for photons fulfilling the offline loose identification as a function of p_{T} in Fig. B.2 and the lines indicate the thresholds. The offline identification employs PF isolation variables that are not available to the trigger and one can see that photons passing the loose identification do not necessarily fulfill the trigger requirements. Especially for the HCAL part, a substantial fraction of events at large p_{T} is not accepted by the trigger.

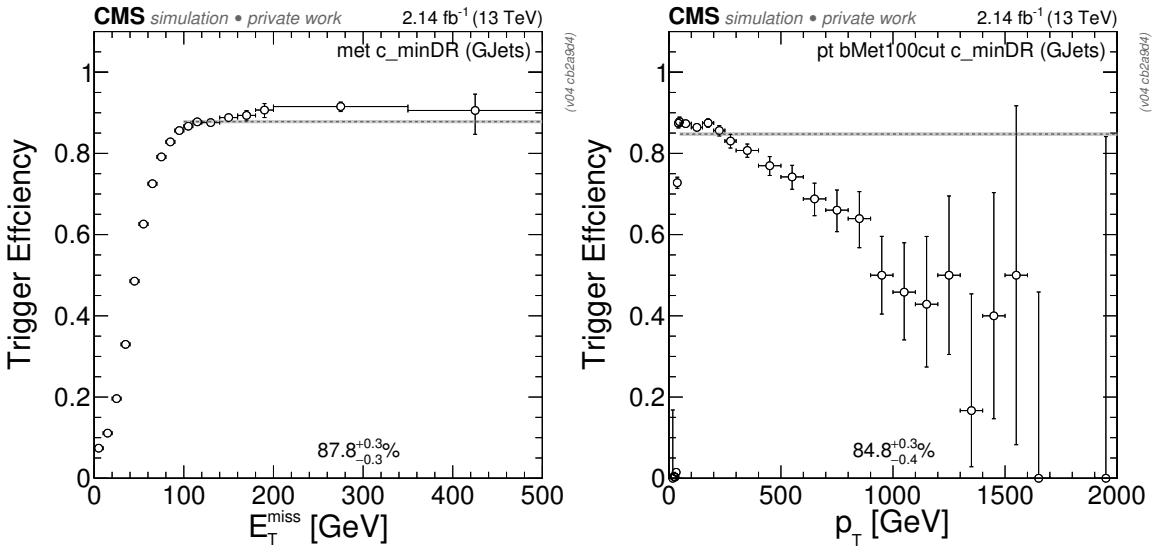

Figure B.1: Efficiency of `HLT_Photon36_R9Id90_HE10_Iso40_EBOnly_PFMET40` (simulated) as a function of $E_{\mathrm{T}}^{\mathrm{miss}}$ and photon p_{T}, measured in γ+jets simulation.

This is also shown in Fig. B.3, where the efficiency of all three components is displayed separately. One can see that the HCAL part of the trigger requirement is causing the overall inefficiency of the trigger.

This inefficiency does not allow the usage of the trigger. Also the usage of a tighter offline photon identification does not solve this issue.

The problem was presented to the CMS Trigger Studies Group[1] and a data quality monitoring (DQM) module was implemented[2]. During the development of the DQM module it was discovered that efficiency plots for many SUSY/BSM HLT paths were not created correctly. Accordingly, the efficiency calculation for the other HLT paths was also fixed[3]. The changes were included in the `CMSSW_8_0_X` development branch.

[1] `https://indico.cern.ch/event/475239/` [CMS interal]
[2] `https://github.com/cms-sw/cmssw/pull/13148`
[3] `https://github.com/cms-sw/cmssw/pull/13150`

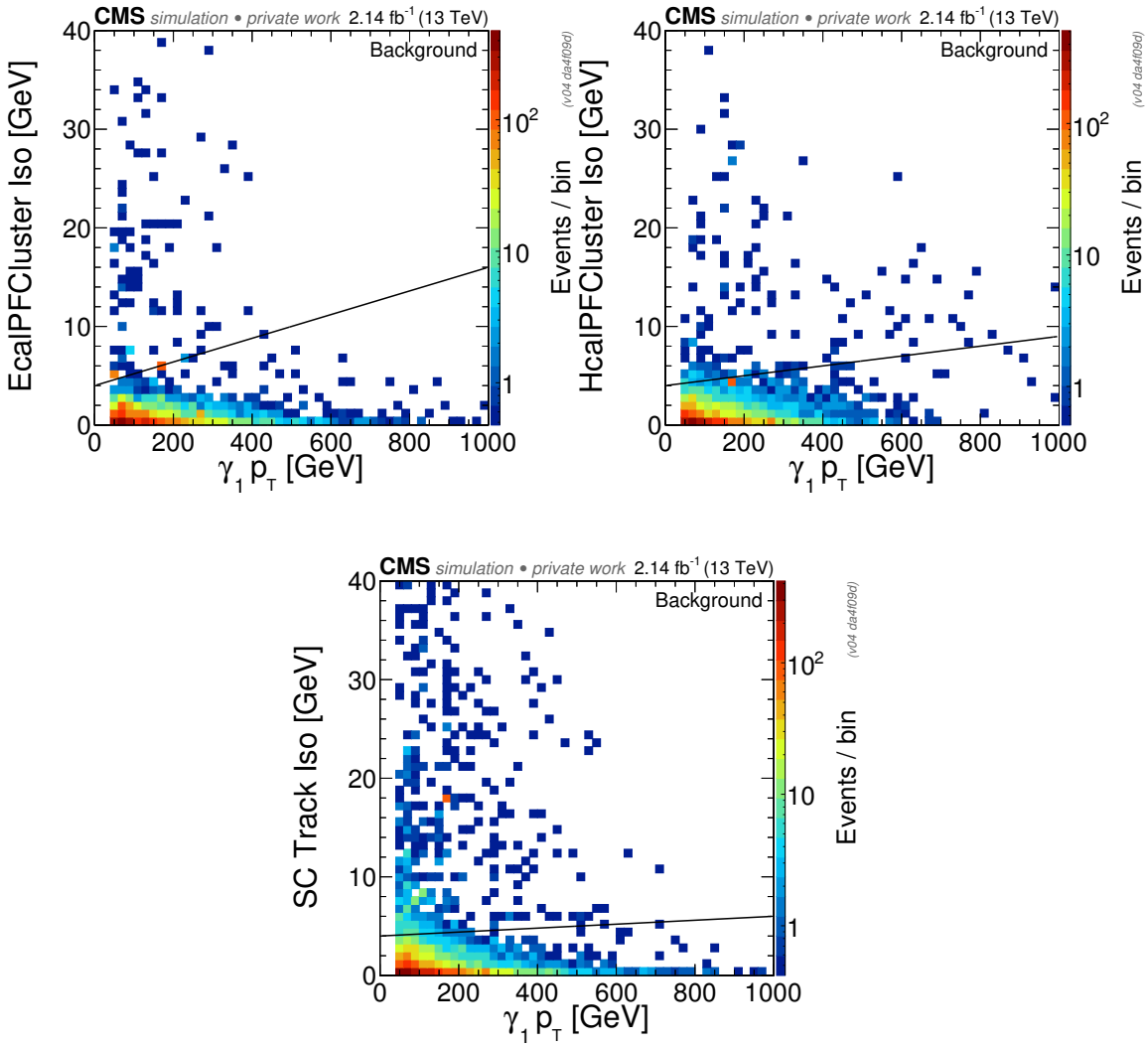

Figure B.2: The distribution of the three trigger isolation components as a function of p_{T}. All photons have passed the offline loose identification. The lines indicate the thresholds required by the trigger.

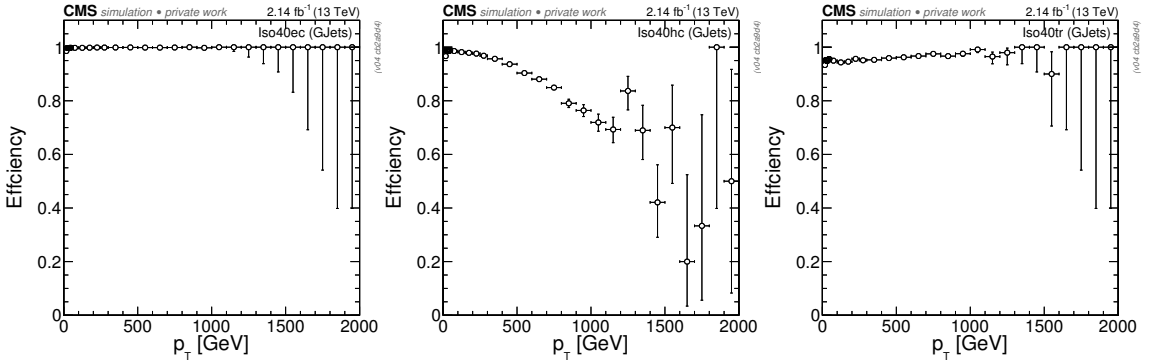

Figure B.3: The efficiencies of the single trigger isolation requirements as a function of p_{T}. Left: EcalPFClusterIso. Middle: HcalPFClusterIso. Right: hollowTrackIso.

HLT_Photon135_PFMET100

The problem described above can be solved by loosening the isolation requirements of the trigger. To counter the resulting rate increase, the photon p_T and/or E_T^{miss} thresholds have to be increased, though. Due to the difference of the isolations used on trigger level and in the offline identification, one cannot reach an efficiency close to 100% in all p_T ranges. Thus, a trigger not using isolations is a preferrable choice, on the other hand implying high thresholds.

The photon+E_T^{miss} trigger without isolation requirements and with the lowest thresholds is HLT_Photon135_PFMET100. The photon p_T, E_T^{miss}, and $\mathcal{S}$ distributions in the efficiency plateau ($p_T > 140\,\text{GeV}$, $E_T^{miss} > 260\,\text{GeV}$) are shown in Fig. B.4. The number of events passing these requirements is too low to allow for a satisfying control region definition to perform the main background estimation described in Section 4.1.

Consequently, the single photon trigger HLT_Photon165_HE10 is used for the analysis of the 2015 data. The photon+E_T^{miss} trigger is considered a good option for the full 2016 dataset, though.

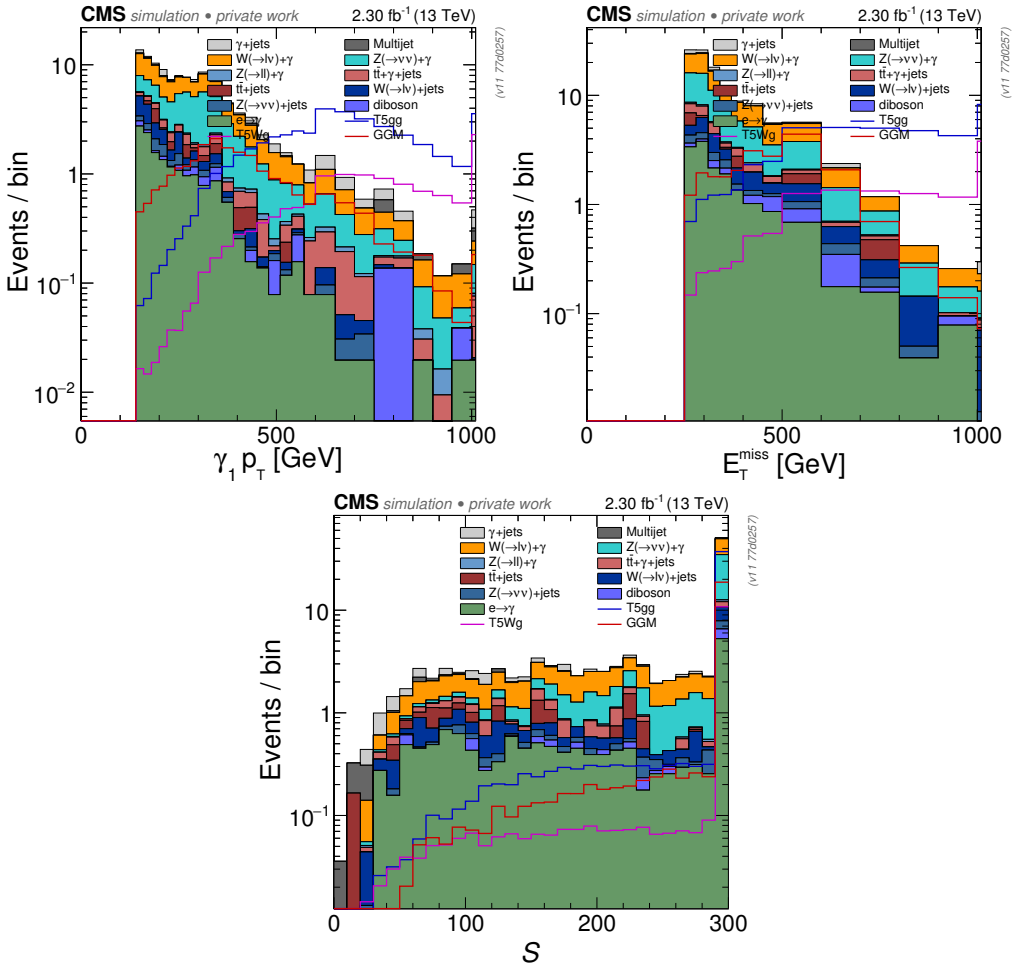

Figure B.4: Photon p_T (top left), E_T^{miss} (top right), and $\mathcal{S}$ (bottom) distributions after the preselection for HLT_Photon135_PFMET100 ($p_T > 140\,\text{GeV}$, $E_T^{miss} > 260\,\text{GeV}$). Steps in the distributions are due to varying bin widths. The overflow is contained in the last bin.

Appendix C

Decomposition of correlated uncertainties

Consider two random variables following normal distributions with different means and standard deviations,

$$X \sim \mathcal{N}(\bar{X}; \sigma_X)$$
$$Y \sim \mathcal{N}(\bar{Y}; \sigma_Y)$$

with a correlation coefficient $\varrho = \mathrm{Cov}(X,Y)/(\sigma_X \sigma_Y) \in [0,1]$. The aim is to decompose the uncertainties such that the remaining components are either 0% or ±100% correlated.

Since the means do not influence the uncertainties, one can assume $\bar{X} = \bar{Y} = 0$. In addition the variables $\hat{X}, \hat{Y}$ are normalized to the standard deviations ($\hat{X} = X/\sigma_X$, $\hat{Y} = Y/\sigma_Y$), such that

$$\hat{X} \sim \mathcal{N}(0; \sigma_{\hat{X}} = 1)$$
$$\hat{Y} \sim \mathcal{N}(0; \sigma_{\hat{Y}} = 1).$$

Assume that the variance of $\hat{Y}$ can be decomposed into two independent parts, one originating from the variation of $\hat{X}$ and one part that is uncorrelated and thus independent of $\hat{X}$,

$$\sigma^2_{\hat{Y}} = \sigma^2_{\hat{X}\to\hat{Y}} + \sigma^{\mathrm{unc}2}_{\hat{Y}}. \tag{C.1}$$

The part that is originating from the correlation with $\hat{X}$ is determined by considering the variance of $\hat{X}$,

$$\mathrm{Var}\left[\hat{X}\right] = \frac{1}{N}\sum_{i=1}^{N}(\hat{x}_i - \bar{X})^2 = \frac{1}{N}\sum_{i=1}^{N}\Delta\hat{x}_i^2,$$

where $\Delta\hat{x}_i = \hat{x}_i - \bar{X}$. A measurement $\hat{x} = \bar{X} + \Delta\hat{x}$ drawn from $\hat{X}$ leads to a shift of $\hat{y}$ of $\Delta_{\hat{x}}\hat{y} = \varrho\Delta\hat{x}$. Now, the variance of $\hat{Y}$ resulting from the variance of $\hat{X}$ can be calculated

$$\begin{aligned}\sigma^2_{\hat{X}\to\hat{Y}} &= \mathrm{Var}_{\hat{X}}\left[\hat{Y}\right] = \frac{1}{N}\sum_{i=1}^{N}(\Delta_{\hat{x}}\hat{y}_i)^2 = \varrho^2\frac{1}{N}\sum_{i=1}^{N}(\Delta\hat{x}_i)^2 = \varrho^2\,\mathrm{Var}\left[\hat{X}\right] \\ &= \varrho^2\sigma^2_{\hat{X}} = \varrho^2.\end{aligned}$$

This part is fully correlated with $\hat{X}$. The remaining uncorrelated component of the variance can be evaluated using Eq. (C.1) and the known total value $\sigma^2_{\hat{Y}} = 1$,

$$\sigma^{\mathrm{unc}2}_{\hat{Y}} = \sigma^2_{\hat{Y}} - \sigma^2_{\hat{X}\to\hat{Y}} = 1 - \varrho^2.$$

These results are translated to the uncertainties of the original random variables X and Y,

$$\sigma_{X\to Y} = \sigma_{\hat{X}\to\hat{Y}} \cdot \sigma_Y = \varrho \cdot \sigma_Y$$
$$\sigma_Y^{\text{unc}} = \sigma_{\hat{Y}}^{\text{unc}} \cdot \sigma_Y = \sqrt{1-\varrho^2} \cdot \sigma_Y \,.$$

For the limit calculation σ_X and $\sigma_{X\to Y}$ are considered with 100% correlation, while σ_Y^{unc} is treated as uncorrelated. For each component, all bins are fully correlated.

References

[1] CMS Collaboration, "Search for supersymmetry in final states with at least one photon and $E_{\mathrm{T}}^{\mathrm{miss}}$ in pp collisions at $\sqrt{s} = 13\,\mathrm{TeV}$", CMS Physics Analysis Summary CMS-PAS-SUS-16-023, CERN, Geneva, 2016.

[2] J. Lange, J. Schulz, C. Autermann, and L. Feld, "Search for supersymmetry in final states with at least one photon and $E_{\mathrm{T}}^{\mathrm{miss}}$ in pp collisions at $\sqrt{s} = 13$ TeV", CMS Analysis Note CMS AN-2016/155 v6 [CMS internal], CERN, Geneva, 2016.

[3] CMS Collaboration, "Observation of a new boson at a mass of 125 GeV with the CMS experiment at the LHC", *Phys. Lett. B* **716** (2012) 30, doi:10.1016/j.physletb.2012.08.021, arXiv:1207.7235.

[4] ATLAS Collaboration, "Observation of a new particle in the search for the Standard Model Higgs boson with the ATLAS detector at the LHC", *Phys. Lett. B* **716** (2012) 1, doi:10.1016/j.physletb.2012.08.020, arXiv:1207.7214.

[5] ATLAS Collaboration, CMS Collaboration, "Combined Measurement of the Higgs Boson Mass in pp Collisions at $\sqrt{s} = 7$ and 8 TeV with the ATLAS and CMS Experiments", *Phys. Rev. Lett.* **114** (2015) 191803, doi:10.1103/PhysRevLett.114.191803, arXiv:1503.07589.

[6] CMS Collaboration, "Precise determination of the mass of the Higgs boson and tests of compatibility of its couplings with the standard model predictions using proton collisions at 7 and 8 TeV", *Eur. Phys. J. C* **75** (2015), no. 5, 212, doi:10.1140/epjc/s10052-015-3351-7, arXiv:1412.8662.

[7] Particle Data Group Collaboration, "Review of Particle Physics", *Chin. Phys. C* **38** (2014) 090001, doi:10.1088/1674-1137/38/9/090001.

[8] CMS Collaboration, "Evidence for the direct decay of the 125 GeV Higgs boson to fermions", *Nature Phys.* **10** (2014) 557, doi:10.1038/nphys3005, arXiv:1401.6527.

[9] ATLAS Collaboration, "Evidence for the Higgs-boson Yukawa coupling to tau leptons with the ATLAS detector", *JHEP* **04** (2015) 117, doi:10.1007/JHEP04(2015)117, arXiv:1501.04943.

[10] CMS Collaboration, "Evidence for the 125 GeV Higgs boson decaying to a pair of τ leptons", *JHEP* **05** (2014) 104, doi:10.1007/JHEP05(2014)104, arXiv:1401.5041.

[11] CMS Collaboration, "Measurements of properties of the Higgs boson and search for an additional resonance in the four-lepton final state at $\sqrt{s} = 13$ TeV", CMS Physics Analysis Summary CMS-PAS-HIG-16-033, CERN, Geneva, 2016.

[12] CMS Collaboration, "Updated measurements of Higgs boson production in the diphoton decay channel at $\sqrt{s} = 13$ TeV in pp collisions at CMS.", CMS Physics Analysis Summary CMS-PAS-HIG-16-020, CERN, Geneva, 2016.

[13] Virgo Collaboration, LIGO Scientific Collaboration, "Observation of Gravitational Waves from a Binary Black Hole Merger", *Phys. Rev. Lett.* **116** (2016), no. 6, 061102, doi:10.1103/PhysRevLett.116.061102, arXiv:1602.03837.

[14] Virgo Collaboration, LIGO Scientific Collaboration, "GW151226: Observation of Gravitational Waves from a 22-Solar-Mass Binary Black Hole Coalescence", *Phys. Rev. Lett.* **116** (2016), no. 24, 241103, doi:10.1103/PhysRevLett.116.241103, arXiv:1606.04855.

[15] D. I. Kazakov, "Beyond the standard model: In search of supersymmetry", in *Proceedings, 2000 European School of high-energy physics*, p. 125. Caramulo, Portugal, August, 2000. arXiv:hep-ph/0012288.

[16] S. P. Martin, "A Supersymmetry primer", *Adv. Ser. Direct. High Energy Phys.* **18** (1998) 1, doi:10.1142/9789812839657_0001, arXiv:hep-ph/9709356.

[17] M. J. Dugan, H. Georgi, and D. B. Kaplan, "Anatomy of a Composite Higgs Model", *Nucl. Phys. B* **254** (1985) 299, doi:10.1016/0550-3213(85)90221-4.

[18] N. Arkani-Hamed, S. Dimopoulos, and G. R. Dvali, "The Hierarchy problem and new dimensions at a millimeter", *Phys. Lett. B* **429** (1998) 263, doi:10.1016/S0370-2693(98)00466-3, arXiv:hep-ph/9803315.

[19] M. Persic, P. Salucci, and F. Stel, "The Universal rotation curve of spiral galaxies: 1. The Dark matter connection", *Mon. Not. Roy. Astron. Soc.* **281** (1996) 27, doi:10.1093/mnras/281.1.27,10.1093/mnras/278.1.27, arXiv:astro-ph/9506004.

[20] D. Clowe et al., "A direct empirical proof of the existence of dark matter", *Astrophys. J.* **648** (2006) L109, doi:10.1086/508162, arXiv:astro-ph/0608407.

[21] P. Ramond, "Dual theory for free fermions", *Phys. Rev. D* **3** (1971) 2415, doi:10.1103/PhysRevD.3.2415.

[22] J. Wess and B. Zumino, "Supergauge transformations in four-dimensions", *Nucl. Phys. B* **70** (1974) 39, doi:10.1016/0550-3213(74)90355-1.

[23] D. Z. Freedman, P. van Nieuwenhuizen, and S. Ferrara, "Progress toward a theory of supergravity", *Phys. Rev. D* **13** (1976) 3214, doi:10.1103/PhysRevD.13.3214.

[24] P. Fayet, "Supergauge invariant extension of the Higgs mechanism and a model for the electron and its neutrino", *Nucl. Phys. B* **90** (1975) 104, doi:10.1016/0550-3213(75)90636-7.

[25] A. H. Chamseddine, R. L. Arnowitt, and P. Nath, "Locally supersymmetric grand unification", *Phys. Rev. Lett.* **49** (1982) 970, doi:10.1103/PhysRevLett.49.970.

[26] L. J. Hall, J. D. Lykken, and S. Weinberg, "Supergravity as the messenger of supersymmetry breaking", *Phys. Rev. D* **27** (1983) 2359, doi:10.1103/PhysRevD.27.2359.

[27] G. L. Kane, C. F. Kolda, L. Roszkowski, and J. D. Wells, "Study of constrained minimal supersymmetry", *Phys. Rev. D* **49** (1994) 6173, doi:10.1103/PhysRevD.49.6173, arXiv:hep-ph/9312272.

[28] I. J. R. Aitchison, "Supersymmetry and the MSSM: An Elementary introduction", arXiv:hep-ph/0505105.

[29] R. Barbieri and G. F. Giudice, "Upper bounds on supersymmetric particle masses", *Nucl. Phys. B* **306** (1988) 63, doi:10.1016/0550-3213(88)90171-X.

[30] P. Fayet, "Mixing between gravitational and weak interactions through the massive gravitino", *Phys. Lett. B* **70** (1977) 461, doi:10.1016/0370-2693(77)90414-2.

[31] H. Baer, M. Brhlik, C. H. Chen, and X. Tata, "Signals for the minimal gauge-mediated supersymmetry breaking model at the Fermilab Tevatron collider", *Phys. Rev. D* **55** (1997) 4463, doi:10.1103/PhysRevD.55.4463, arXiv:hep-ph/9610358.

[32] H. Baer, P. G. Mercadante, X. Tata, and Y. L. Wang, "Reach of Tevatron upgrades in gauge-mediated supersymmetry breaking models", *Phys. Rev. D* **60** (1999) 055001, doi:10.1103/PhysRevD.60.055001, arXiv:hep-ph/9903333.

[33] S. Dimopoulos, S. Thomas, and J. D. Wells, "Sparticle spectroscopy and electroweak symmetry breaking with gauge-mediated supersymmetry breaking", *Nucl. Phys. B* **488** (1997) 39, doi:10.1016/S0550-3213(97)00030-8, arXiv:hep-ph/9609434.

[34] J. R. Ellis, J. L. Lopez, and D. V. Nanopoulos, "Analysis of LEP constraints on supersymmetric models with a light gravitino", *Phys. Lett. B* **394** (1997) 354, doi:10.1016/S0370-2693(97)00019-1, arXiv:hep-ph/9610470.

[35] M. Dine, A. E. Nelson, Y. Nir, and Y. Shirman, "New tools for low energy dynamical supersymmetry breaking", *Phys. Rev. D* **53** (1996) 2658, doi:10.1103/PhysRevD.53.2658, arXiv:hep-ph/9507378.

[36] G. F. Giudice and R. Rattazzi, "Gauge-mediated supersymmetry breaking", in *Perspectives on supersymmetry*, p. 355. World Scientific, Singapore, 1998.

[37] P. Meade, N. Seiberg, and D. Shih, "General gauge mediation", *Prog. Theor. Phys. Suppl.* **177** (2009) 143, doi:10.1143/PTPS.177.143, arXiv:0801.3278.

[38] M. Buican, P. Meade, N. Seiberg, and D. Shih, "Exploring general gauge mediation", *JHEP* **03** (2009) 016, doi:10.1088/1126-6708/2009/03/016, arXiv:0812.3668.

[39] J. T. Ruderman and D. Shih, "General neutralino NLSPs at the early LHC", *JHEP* **08** (2012) 159, doi:10.1007/JHEP08(2012)159, arXiv:1103.6083.

[40] Y. Kats, P. Meade, M. Reece, and D. Shih, "The status of GMSB after 1/fb at the LHC", *JHEP* **02** (2012) 115, doi:10.1007/JHEP02(2012)115, arXiv:1110.6444.

[41] Y. Kats and M. J. Strassler, "Probing colored particles with photons, leptons, and jets", *JHEP* **11** (2012) 097, doi:10.1007/JHEP11(2012)097, arXiv:1204.1119.

[42] P. Grajek, A. Mariotti, and D. Redigolo, "Phenomenology of general gauge mediation in light of a 125 GeV Higgs", *JHEP* **07** (2013) 109, doi:10.1007/JHEP07(2013)109, arXiv:1303.0870.

[43] Y. Kats, P. Meade, M. Reece, and D. Shih, "Simple SUSY spectra for photons + $E_{\mathrm{T}}^{\mathrm{miss}}$ searches", 2012. http://www.physics.rutgers.edu/~kats/binoNLSP [accessed 2016-05-23].

[44] P. Meade, M. Reece, and D. Shih, "Prompt Decays of General Neutralino NLSPs at the Tevatron", *JHEP* **05** (2010) 105, doi:10.1007/JHEP05(2010)105, arXiv:0911.4130.

[45] S. Myers, "The LEP Collider, from design to approval and commissioning". John Adams' Lecture, CERN-91-08, CERN-YELLOW-91-08. CERN, Geneva, 1991. Delivered at CERN, 26 Nov 1990.

[46] R. R. Wilson, "The Tevatron", *Phys. Today* **30N10** (1977) 23, doi:10.1063/1.3037746.

[47] C. Autermann for the CMS Collaboration, "Search for Supersymmetry at CMS", *J. Phys. Conf. Ser.* **623** (2015), no. 1, 012004, doi:10.1088/1742-6596/623/1/012004.

[48] C. Autermann, "Experimental status of supersymmetry after the LHC Run-I", *Prog. Part. Nucl. Phys.* **90** (2016) 125, doi:10.1016/j.ppnp.2016.06.001, arXiv:1609.01686.

[49] CMS Collaboration, "Search for new physics in events with photons, jets, and missing transverse energy in pp collisions at $\sqrt{s} = 7$ TeV", *JHEP* **1303** (2013) 111, doi:10.1007/JHEP03(2013)111, arXiv:1211.4784.

[50] CMS Collaboration, "Search for supersymmetry with photons in pp collisions at $\sqrt{s}$=8 TeV", *Phys. Rev. D* **92** (2015), no. 7, 072006, doi:10.1103/PhysRevD.92.072006, arXiv:1507.02898.

[51] CMS Collaboration, "Search for supersymmetry in events with a photon, a lepton, and missing transverse momentum in pp collisions at $\sqrt{s} = 8$ TeV", *Phys. Lett. B* **757** (2016) 6, doi:10.1016/j.physletb.2016.03.039, arXiv:1508.01218.

[52] CMS Collaboration, "Search for top squark and higgsino production using diphoton Higgs boson decays", *Phys. Rev. Lett.* **112** (2014) 161802, doi:10.1103/PhysRevLett.112.161802, arXiv:1312.3310.

[53] CMS Collaboration, "Search for SUSY with Higgs in the diphoton final state using the razor variables", CMS Physics Analysis Summary CMS-PAS-SUS-14-017, CERN, Geneva, 2015.

[54] CMS Collaboration, "Searches for electroweak neutralino and chargino production in channels with Higgs, Z, and W bosons in pp collisions at 8 TeV", *Phys. Rev. D* **90** (2014), no. 9, 092007, doi:10.1103/PhysRevD.90.092007, arXiv:1409.3168.

[55] ATLAS Collaboration, "Search for photonic signatures of gauge-mediated supersymmetry in 8 TeV pp collisions with the ATLAS detector", *Phys. Rev. D* **92** (2015), no. 7, 072001, doi:10.1103/PhysRevD.92.072001, arXiv:1507.05493.

[56] ATLAS Collaboration, "Search for new phenomena in events with a photon and missing transverse momentum in pp collisions at $\sqrt{s} = 8$ TeV with the ATLAS detector", *Phys. Rev. D* **91** (2015), no. 1, 012008, doi:10.1103/PhysRevD.92.059903,10.1103/PhysRevD.91.012008, arXiv:1411.1559. [Erratum: *Phys. Rev. D* **92** (2015), no. 5, 059903].

[57] CMS Collaboration, "Search for supersymmetry in electroweak production with photons and large missing transverse energy in pp collisions at $\sqrt{s} = 8$ TeV", *Phys. Lett. B* **759** (2016) 479, doi:10.1016/j.physletb.2016.05.088, arXiv:1602.08772.

[58] J. Schulz, "Search for electroweak production of supersymmetric gauginos with photons at CMS", Master thesis, CMS-TS-2014-031, CERN-THESIS-2014-141, RWTH Aachen University, Aachen, 2014.

[59] CMS Collaboration, "Data parking and data scouting at the CMS experiment", CMS Performance note CMS-DP-2012-022, CERN, (2012).

[60] CMS Collaboration, "Search for supersymmetry in events with photons and missing transverse energy", CMS Physics Analysis Summary CMS-PAS-SUS-15-012, CERN, Geneva, 2016.

[61] CMS Collaboration, "Search for SUSY in Events with a Higgs Decaying to Two Photons Using the Razor Variables", CMS Physics Analysis Summary CMS-PAS-SUS-16-012, CERN, Geneva, 2016.

[62] ATLAS Collaboration, "Search for supersymmetry in a final state containing two photons and missing transverse momentum in $\sqrt{s} = 13$ TeV pp collisions at the LHC using the ATLAS detector", *submitted to Eur. Phys. J. C* (2016) arXiv:1606.09150.

[63] ATLAS Collaboration, "Search for Supersymmetry in events with photons, jets and missing transverse energy with the ATLAS detector in 13 TeV pp collisions", ATLAS Note ATLAS-CONF-2016-066, CERN, Geneva, Aug, 2016.

[64] L. Evans and P. Bryant, "LHC Machine", *JINST* **3** (2008) S08001, doi:10.1088/1748-0221/3/08/S08001.

[65] CMS Collaboration, "Particle Kickers". https://cds.cern.ch/record/1706606/ [accessed 2016-08-09].

[66] ATLAS Collaboration, "The ATLAS Experiment at the CERN Large Hadron Collider", *JINST* **3** (2008) S08003, doi:10.1088/1748-0221/3/08/S08003.

[67] LHCb Collaboration, "The LHCb Detector at the LHC", *JINST* **3** (2008) S08005, doi:10.1088/1748-0221/3/08/S08005.

[68] ALICE Collaboration, "The ALICE experiment at the CERN LHC", *JINST* **3** (2008) S08002, doi:10.1088/1748-0221/3/08/S08002.

[69] CMS Collaboration, "The CMS experiment at the CERN LHC", *JINST* **3** (2008) S08004, doi:10.1088/1748-0221/3/08/S08004.

[70] T. Sakuma and T. McCauley, "Detector and Event Visualization with SketchUp at the CMS Experiment", *J. Phys. Conf. Ser.* **513** (2014) 022032, doi:10.1088/1742-6596/513/2/022032, arXiv:1311.4942.

[71] Tai Sakuma, "CMS SketchUp file". https://cms-docdb.cern.ch/cgi-bin/DocDB/ShowDocument?docid=5958 [accessed 2016-08-09].

[72] P. Adzic et al., "Energy resolution of the barrel of the CMS electromagnetic calorimeter", *JINST* **2** (2007) P04004, doi:10.1088/1748-0221/2/04/P04004.

[73] G. Bauer et al., "The CMS High Level Trigger System: Experience and future development", *J. Phys. Conf. Ser.* **396** (2012) 012008, doi:10.1088/1742-6596/396/1/012008.

[74] CMS Collaboration, "Public CMS Luminosity Information". https://twiki.cern.ch/twiki/bin/view/CMSPublic/LumiPublicResults?rev=116 [accessed 2016-09-10].

[75] G. Petrucciani, A. Rizzi, and C. Vuosalo, "Mini-AOD: A New Analysis Data Format for CMS", *J. Phys. Conf. Ser.* **664** (2015), no. 7, 072052, doi:10.1088/1742-6596/664/7/072052.

[76] I. Bird, "Computing for the Large Hadron Collider", *Ann. Rev. Nucl. Part. Sci.* **61** (2011) 99, doi:10.1146/annurev-nucl-102010-130059.

[77] D. Spiga et al., "The CMS Remote Analysis Builder (CRAB)", *Lect. Notes Comput. Sci.* **4873** (2007) 580, doi:10.1007/978-3-540-77220-0_52.

[78] R. Brun and F. Rademakers, "ROOT: An object oriented data analysis framework", *Nucl. Instrum. Meth. A* **389** (1997) 81, doi:10.1016/S0168-9002(97)00048-X.

[79] I. Antcheva et al., "ROOT: A C++ framework for petabyte data storage, statistical analysis and visualization", *Comput. Phys. Commun.* **180** (2009) 2499, doi:10.1016/j.cpc.2009.08.005, arXiv:1508.07749.

[80] CMS Collaboration, "Particle-Flow Event Reconstruction in CMS and Performance for Jets, Taus, and MET", CMS Physics Analysis Summary CMS-PAS-PFT-09-001, CERN, Geneva, 2009.

[81] CMS Collaboration, "Commissioning of the Particle-flow Event Reconstruction with the first LHC collisions recorded in the CMS detector", CMS Physics Analysis Summary CMS-PAS-PFT-10-001, CERN, Geneva, 2010.

[82] L. Gray for the CMS EGM POG, "GED Electron and Photon Reconstruction for Run 2", Second EGM Global Event Description Workshop https://indico.cern.ch/event/306030/contributions/704002/ [CMS internal], CERN, Geneva, 2014-03-24.

[83] CMS Collaboration, "Performance of Photon Reconstruction and Identification with the CMS Detector in Proton-Proton Collisions at $\sqrt{s} = 8$ TeV", *JINST* **10** (2015), no. 08, P08010, doi:10.1088/1748-0221/10/08/P08010, arXiv:1502.02702.

[84] CMS Collaboration, "Performance of Electron Reconstruction and Selection with the CMS Detector in Proton-Proton Collisions at $\sqrt{s} = 8$ TeV", *JINST* **10** (2015), no. 06, P06005, doi:10.1088/1748-0221/10/06/P06005, arXiv:1502.02701.

[85] CMS Collaboration, "Description and performance of track and primary-vertex reconstruction with the CMS tracker", *JINST* **9** (2014), no. 10, P10009, doi:10.1088/1748-0221/9/10/P10009, arXiv:1405.6569.

[86] W. Adam, R. Frühwirth, A. Strandlie, and T. Todor, "Reconstruction of Electrons with the Gaussian-Sum Filter in the CMS Tracker at the LHC", CMS Note CMS-NOTE-2005-001, CERN, Geneva, Jan, 2005.

[87] CMS Collaboration, "Cut Based Photon ID for Run 2". https://twiki.cern.ch/twiki/bin/view/CMS/CutBasedPhotonIdentificationRun2?rev=28#SPRING15_selections_25_ns [accessed 2016-08-31].

[88] CMS Collaboration, "Cut Based Electron ID for Run 2". https://twiki.cern.ch/twiki/bin/view/CMS/CutBasedElectronIdentificationRun2?rev=36#Spring15_selection_25ns [accessed 2016-09-02].

[89] CMS Collaboration, "Particle-flow commissioning with muons and electrons from J/Psi and W events at 7 TeV", CMS Physics Analysis Summary CMS-PAS-PFT-10-003, CERN, Geneva, 2010.

[90] CMS Collaboration, "Baseline muon selections for Run-II". https://twiki.cern.ch/twiki/bin/view/CMS/SWGuideMuonIdRun2?rev=26#Tight_Muon [accessed 2016-09-05].

[91] M. Cacciari, G. P. Salam, and G. Soyez, "The Anti-k(t) jet clustering algorithm", *JHEP* **04** (2008) 063, doi:10.1088/1126-6708/2008/04/063, arXiv:0802.1189.

[92] M. Cacciari, G. P. Salam, and G. Soyez, "FastJet User Manual", *Eur. Phys. J. C* **72** (2012) 1896, doi:10.1140/epjc/s10052-012-1896-2, arXiv:1111.6097.

[93] M. Cacciari and G. P. Salam, "Dispelling the N^3 myth for the k_t jet-finder", *Phys. Lett. B* **641** (2006) 57, doi:10.1016/j.physletb.2006.08.037, arXiv:hep-ph/0512210.

[94] CMS Collaboration, "Pileup Removal Algorithms", CMS Physics Analysis Summary CMS-PAS-JME-14-001, CERN, Geneva, 2014.

[95] CMS Collaboration, "Determination of Jet Energy Calibration and Transverse Momentum Resolution in CMS", *JINST* **6** (2011) P11002, doi:10.1088/1748-0221/6/11/P11002, arXiv:1107.4277.

[96] CMS Collaboration, "Recommended Jet Energy Corrections and Uncertainties For Data and MC". https://twiki.cern.ch/twiki/bin/view/CMS/JECDataMC?rev=119#Jet_Energy_Corrections_in_Run2 [accessed 2016-08-31].

[97] CMS Collaboration, "Jet Identification". https://twiki.cern.ch/twiki/bin/view/CMS/JetID?rev=94#Recommendations_for_13_TeV_data [accessed 2016-08-31].

[98] CMS Collaboration, "Jet energy scale and resolution in the CMS experiment in pp collisions at 8 TeV", *submitted to JINST* (2016) arXiv:1607.03663.

[99] CMS Collaboration, "Identification of b-quark jets with the CMS experiment", *JINST* **8** (2013) P04013, doi:10.1088/1748-0221/8/04/P04013, arXiv:1211.4462.

[100] CMS Collaboration, "Identification of b quark jets at the CMS Experiment in the LHC Run 2", CMS Physics Analysis Summary CMS-PAS-BTV-15-001, CERN, Geneva, 2016.

[101] CMS Collaboration, "Missing transverse energy performance of the CMS detector", *JINST* **6** (2011) P09001, doi:10.1088/1748-0221/6/09/P09001, arXiv:1106.5048.

[102] CMS Collaboration, "Performance of the CMS missing transverse momentum reconstruction in pp data at $\sqrt{s} = 8$ TeV", *JINST* **10** (2015), no. 02, P02006, doi:10.1088/1748-0221/10/02/P02006, arXiv:1411.0511.

[103] CMS Collaboration, "Performance of missing energy reconstruction in 13 TeV pp collision data using the CMS detector", CMS Physics Analysis Summary CMS-PAS-JME-16-004, CERN, Geneva, 2016.

[104] CMS Collaboration, "The CMS dataset bookkeeping service", *J. Phys. Conf. Ser.* **119** (2008) 072001, doi:10.1088/1742-6596/119/7/072001.

[105] J. Alwall et al., "The automated computation of tree-level and next-to-leading order differential cross sections, and their matching to parton shower simulations", *JHEP* **07** (2014) 079, doi:10.1007/JHEP07(2014)079, arXiv:1405.0301.

[106] P. Nason, "A New method for combining NLO QCD with shower Monte Carlo algorithms", *JHEP* **11** (2004) 040, doi:10.1088/1126-6708/2004/11/040, arXiv:hep-ph/0409146.

[107] S. Frixione, P. Nason, and C. Oleari, "Matching NLO QCD computations with Parton Shower simulations: the POWHEG method", *JHEP* **11** (2007) 070, doi:10.1088/1126-6708/2007/11/070, arXiv:0709.2092.

[108] S. Alioli, P. Nason, C. Oleari, and E. Re, "A general framework for implementing NLO calculations in shower Monte Carlo programs: the POWHEG BOX", *JHEP* **06** (2010) 043, doi:10.1007/JHEP06(2010)043, arXiv:1002.2581.

[109] T. Melia, P. Nason, R. Rontsch, and G. Zanderighi, "W+W-, WZ and ZZ production in the POWHEG BOX", *JHEP* **11** (2011) 078, doi:10.1007/JHEP11(2011)078, arXiv:1107.5051.

[110] P. Nason and G. Zanderighi, "W^+W^-, WZ and ZZ production in the POWHEG-BOX-V2", *Eur. Phys. J. C* **74** (2014), no. 1, 2702, doi:10.1140/epjc/s10052-013-2702-5, arXiv:1311.1365.

[111] T. Sjöstrand, S. Mrenna, and P. Skands, "PYTHIA 6.4 physics and manual", *JHEP* **05** (2006) 026, doi:10.1088/1126-6708/2006/05/026, arXiv:hep-ph/0603175.

[112] T. Sjostrand, S. Mrenna, and P. Z. Skands, "A Brief Introduction to PYTHIA 8.1", *Comput. Phys. Commun.* **178** (2008) 852, doi:10.1016/j.cpc.2008.01.036, arXiv:0710.3820.

[113] GEANT4 Collaboration, "GEANT4: A Simulation toolkit", *Nucl. Instrum. Meth. A* **506** (2003) 250, doi:10.1016/S0168-9002(03)01368-8.

[114] G. Bozzi et al., "Production of Drell-Yan lepton pairs in hadron collisions: Transverse-momentum resummation at next-to-next-to-leading logarithmic accuracy", *Phys. Lett. B* **696** (2011) 207, doi:10.1016/j.physletb.2010.12.024, arXiv:1007.2351.

[115] T. Gehrmann et al., "W^+W^- Production at Hadron Colliders in Next to Next to Leading Order QCD", *Phys. Rev. Lett.* **113** (2014), no. 21, 212001, doi:10.1103/PhysRevLett.113.212001, arXiv:1408.5243.

[116] CMS Collaboration, "The fast simulation of the CMS detector at LHC", *J. Phys. Conf. Ser.* **331** (2011) 032049, doi:10.1088/1742-6596/331/3/032049.

[117] C. Borschensky et al., "Squark and gluino production cross sections in pp collisions at $\sqrt{s} = 13$, 14, 33 and 100 TeV", *Eur. Phys. J. C* **74** (2014), no. 12, 3174, doi:10.1140/epjc/s10052-014-3174-y, arXiv:1407.5066.

[118] B. Fuks, M. Klasen, D. R. Lamprea, and M. Rothering, "Gaugino production in proton-proton collisions at a center-of-mass energy of 8 TeV", *JHEP* **10** (2012) 081, doi:10.1007/JHEP10(2012)081, arXiv:1207.2159.

[119] B. Fuks, M. Klasen, D. R. Lamprea, and M. Rothering, "Precision predictions for electroweak superpartner production at hadron colliders with RESUMMINO", *Eur. Phys. J. C* **73** (2013) 2480, doi:10.1140/epjc/s10052-013-2480-0, arXiv:1304.0790.

[120] W. Beenakker et al., "The Production of charginos / neutralinos and sleptons at hadron colliders", *Phys. Rev. Lett.* **83** (1999) 3780, doi:10.1103/PhysRevLett.100.029901,10.1103/PhysRevLett.83.3780, arXiv:hep-ph/9906298. [Erratum: *Phys. Rev. Lett.* **100** (2008), 029901].

[121] J. Lange, "Signal production for GMSB", CMS SUSY Trigger/MC/XPAG Meeting https://indico.cern.ch/event/533756/ [CMS internal], CERN, Geneva, 2016-05-23.

[122] CMS Collaboration, "MET Filter Recommendations for Run II". https://twiki.cern.ch/twiki/bin/view/CMS/MissingETOptionalFiltersRun2?rev=99#76X_Recommendations_and_Recipes [accessed 2016-09-01].

[123] C. J. Clopper and E. S. Pearson, "The use of confidence or fiducial limits illustrated in the case of the binomial", *Biometrika* **26** (1934), no. 4, 404, doi:10.1093/biomet/26.4.404.

[124] J. Orear, "Notes on statistics for physicists", University of California rep. UCRL-8417, Lawrence Berkeley Nat. Lab., Berkeley, CA, Aug, 1958.

[125] W. Verkerke and D. P. Kirkby, "The RooFit toolkit for data modeling", *eConf* **C0303241** (2003) MOLT007, arXiv:physics/0306116.

[126] R. Meyer, "Studies of the misidentification probability of electrons as photons with the CMS experiment in data recorded in 2015", Master thesis, RWTH Aachen University, Aachen, 2016.

[127] R. Meyer, M. K. Kiesel, C. Autermann, and L. Feld, "Studies of the misidentification probability of electrons as photons at $\sqrt{s} = 13$ TeV", CMS Analysis Note CMS AN-2016/176 [CMS internal], CERN, Geneva, 2016.

[128] CMS Collaboration, "Measurement of the inclusive top-quark pair + photon production cross section in the muon + jets channel in pp collisions at 8 TeV", CMS Physics Analysis Summary CMS-PAS-TOP-13-011, CERN, Geneva, 2014.

[129] CMS Collaboration, "Measurement of the WW cross section in pp collisions at $\sqrt{s}$=13 TeV", CMS Physics Analysis Summary CMS-PAS-SMP-16-006, CERN, Geneva, 2016.

[130] CMS Collaboration, "Measurement of the WZ production cross section in pp collisions at $\sqrt{s} = 13$ TeV", CMS Physics Analysis Summary CMS-PAS-SMP-16-002, CERN, Geneva, 2016.

[131] CMS Collaboration, "Measurement of the ZZ production cross section and $Z \to \ell\ell\ell'\ell'$ branching fraction in pp collisions at $\sqrt{s} = 13$ TeV", CMS Physics Analysis Summary CMS-PAS-SMP-16-001, CERN, Geneva, 2016.

[132] T. Junk, "Confidence level computation for combining searches with small statistics", *Nucl. Instrum. Meth. A* **434** (1999) 435, arXiv:hep-ex/9902006.

[133] A. L. Read, "Presentation of search results: the CLs technique", *J. Phys. G* **28** (2002) 2693, doi:10.1088/0954-3899/28/10/313.

[134] ATLAS Collaboration, CMS Collaboration, LHC Higgs Combination Group, "Procedure for the LHC Higgs boson search combination in Summer 2011", CMS-NOTE-2011-005. ATL-PHYS-PUB-2011-11, CERN, Geneva, Aug, 2011.

[135] E. Gross and O. Vitells, "Trial factors or the look elsewhere effect in high energy physics", *Eur. Phys. J. C* **70** (2010) 525, doi:10.1140/epjc/s10052-010-1470-8, arXiv:1005.1891.

Eidesstattliche Versicherung

Lange, Johannes

Name, Vorname

Matrikelnummer (freiwillige Angabe)

Ich versichere hiermit an Eides Statt, dass ich die vorliegende ~~Arbeit/Bachelorarbeit/~~ Masterarbeit* mit dem Titel

Search for electroweak production of supersymmetric particles with photonic final states using the first LHC Run II data recorded with the CMS detector

selbständig und ohne unzulässige fremde Hilfe erbracht habe. Ich habe keine anderen als die angegebenen Quellen und Hilfsmittel benutzt. Für den Fall, dass die Arbeit zusätzlich auf einem Datenträger eingereicht wird, erkläre ich, dass die schriftliche und die elektronische Form vollständig übereinstimmen. Die Arbeit hat in gleicher oder ähnlicher Form noch keiner Prüfungsbehörde vorgelegen.

Aachen, 19.09.2016

Ort, Datum

Unterschrift

*Nichtzutreffendes bitte streichen

Belehrung:

§ 156 StGB: Falsche Versicherung an Eides Statt

Wer vor einer zur Abnahme einer Versicherung an Eides Statt zuständigen Behörde eine solche Versicherung falsch abgibt oder unter Berufung auf eine solche Versicherung falsch aussagt, wird mit Freiheitsstrafe bis zu drei Jahren oder mit Geldstrafe bestraft.

§ 161 StGB: Fahrlässiger Falscheid; fahrlässige falsche Versicherung an Eides Statt

(1) Wenn eine der in den §§ 154 bis 156 bezeichneten Handlungen aus Fahrlässigkeit begangen worden ist, so tritt Freiheitsstrafe bis zu einem Jahr oder Geldstrafe ein.

(2) Straflosigkeit tritt ein, wenn der Täter die falsche Angabe rechtzeitig berichtigt. Die Vorschriften des § 158 Abs. 2 und 3 gelten entsprechend.

Die vorstehende Belehrung habe ich zur Kenntnis genommen:

Aachen, 19.09.2016

Ort, Datum

Unterschrift